JAGIELLONIAN UNIVERSITY
IN KRAKÓW

Faculty of Physics, Astronomy and Applied Computer Science

# DEVELOPMENT OF MANGETIC FIELD CONTROL SYSTEMS IN THE NEDM EXPERIMENT

*Author:*

GRZEGORZ WYSZYŃSKI

Thesis supervisor:
prof. dr hab. Kazimierz Bodek

# Abstract

The measurements of the neutron electric dipole moment are a chance to find the evidence for the CP symmetry violation outside the Standard Model. The most promising attempt to improve the present limit on this value is the nEDM experiment at the Paul Scherrer Institute in Villigen, Switzerland. This measurement is done using the Ramsey method of separated oscillatory fields with polarized ultra-cold neutrons, which precess in the uniform magnetic field. The majority of systematic effects are related to inhomogeneities of the magnetic field in the precession volume and its changes in time. The control over these changes is crucial in this experiment. The volume of precession is isolated from outside to stabilize the magnetic field. The strategy for the successful control of the magnetic field constancy employs the passive magnetic shields – multilayer enclosures made of high permeability material, and the active magnetic shields – a system of coils, generating in the real time the magnetic field compensating the external perturbations. The perturbations are measured using the system of sensitive magnetometers.

In this thesis two problems directly related to high quality of the magnetic field in precession volume are addressed. Firstly, an attempt is made to find the optimal active magnetic field compensation system. In the part II four proposed systems are compared: (i) 6-coil Helmholtz-like system, (ii) 12-coil Merritt-based system, (iii) cellular coil system and (iv) spherical coil system. The last option is based on the description of the magnetic field with the vector spherical harmonic basis. It is thought to be a model solution to which other systems would be compared. Other solutions exhibit easier practical realization but at a price of a significantly worse performance. The comprehensive simulations and results of the first tests on the prototypes were used for comparison between the considered systems.

Part III of this dissertation is devoted to the analysis of the maps of the magnetic field, measured using the dedicated robot equipped with a vector magnetometer. The analysis considers mechanical imperfections of the measurement system. The most significant effects are parametrized and determined in a global fit of the model to the measured map. The corrected maps are later on used for calculation of the optimal current values for 33 correction coils, which are designed to homogenize the magnetic field in the precession chamber.

# Streszczenie

Pomiary elektrycznego momentu dipolowego neutronu są szansą na znalezienie dowodów na łamanie symetrii CP w sposób nie uwzględniony w Modelu Standardowym. Obecnie najbardziej obiecującą próbą zmierzenia tej wartości jest eksperyment nEDM w Instytucie Paula Scherrera w Villigen, w Szwajcarii. Pomiar jest wykonywany metodą rezonansową Ramsey'a z wykorzystaniem spolaryzowanych, ultra-zimnych neutronów, które precesują w jednorodnym polu magnetycznym. Większość efektów systematycznych wynika z zaburzeń pola precesji w przestrzeni i czasie. Kontrola pola magnetycznego jest kluczowa w tym eksperymencie. Zapewnienie stałości w czasie zhomogenizowanego pola precesji polega na izolacji krytycznego obszaru od zewnętrznych zaburzeń. Strategia skutecznej kontroli stałości pola wykorzystuje równocześnie osłony pasywne — wielowarstwowe komory z materiału o wysokiej podatności magnetycznej, jak i osłony aktywne -– system otwartych cewek, generujących w czasie rzeczywistym pole kompensujące zewnętrzne zaburzenia. Same zaburzenia wykrywane są przez układy czułych magnetometrów.

W niniejszej pracy podjęto dwa zagadnienia ściśle związane z zapewnieniem wysokiej jakości pola magnetycznego precesji. Pierwsze, to próba znalezienia optymalnego systemu aktywnej kompensacji zaburzeń zewnętrznych. Poświęcona jest jej pierwsza część pracy. Porównano cztery systemy: (i) system oparty na układzie Helmholtza z 6 cewkami, (ii) system oparty na układzie Merritt z 12 cewkami, (iii) system małych cewek „komórkowych", (iv) układ cewek sferycznych. Ostatnia propozycja jest oparta na opisie pola magnetycznego przy pomocy wektorowych harmonik sferycznych i jest pomyślana jako rozwiązanie modelowe, służące do porównania wydajności rozwiązań bardziej praktycznych, ale o mniejszej wydajności od układu sferycznego. Do porównań wykorzystano zarówno wszechstronne obliczenia symulacyjne, jak i wstępne wyniki testów przeprowadzonych na modelu cewek w geometrii sześciennej.

Druga część pracy poświęcona jest analizie map pola magnetycznego wykonanych przy pomocy specjalnego robota wyposażonego w wektorowy sensor pola magnetycznego. Analiza uwzględnia niedoskonałości geometryczne systemu pomiarowego poprzez modelową parametryzację najważniejszych efektów i ustalenie ich wartości w globalnym dopasowaniu modelu do zmierzonej mapy. Oczyszczone w ten sposób mapy są następnie wykorzystane do obliczenia wartości prądów w systemie 33 cewek korekcyjnych, które stanowią pierwsze przybliżenie w procedurze homogenizacji pola magnetycznego w komorze precesji.

# Contents

# List of Figures

# List of Tables

# Part I

# nEDM experiment at PSI

# Chapter 1

# Neutron electric dipole moment and ultra-cold neutrons

## 1.1 Baryon-antibaryon asymmetry and CP symmetry violation

Since the discovery of the positron by Carl Anderson [1], scientists have asked why the universe appears to be built mostly from matter, instead of consisting of equal parts of matter and antimatter. One small piece of this puzzle was solved in 1964 at the Brookheaven National Laboratory where Cronin and Fitch [2] discovered a CP symmetry violation in the decay of the system of neutral K mesons. CP violation is one of necessary conditions to create an asymmetry between baryons and antibaryons, postulated in 1967 by Sakharov [3]. He claimed that to explain the observed level of supremacy of matter in the universe, three conditions must be fulfilled:

- C and CP symmetry violation,

- thermal non-equilibrium,

- baryon number violation.

Up until now, CP symmetry violation was observed only in the mesonic systems - K mesons: indirectly in 1964, directly in 1999 by the KTeV and the NA48 experiments [4,

5], B mesons (Refs. [6, 7]) and D mesons (Ref. [8]) . Another source of CP violation could be responsible for the non-zero neutron electric dipole moment.

## 1.2   Electric dipole moment

The neutron electric dipole moment $d_n$ reflects the difference between the distributions of positive and negative charges inside a neutron. Classical definition is derived from the multipole expansion of the electric potential $\phi_e$ [9], here expressed in the Cartesian coordinate system $x_i,\ i = 1, 2, 3$):

$$\phi_e = \frac{1}{4\pi\varepsilon_0} \int \frac{\rho(\vec{x'})}{\|\vec{x} - \vec{x'}\|} \, \mathrm{d}^3 x' \cong \frac{1}{4\pi\varepsilon_0} \left[ \frac{q}{r} + \frac{\vec{d_n} \cdot r}{r^3} + \frac{1}{2} \sum_{i,j} Q_{ij} \frac{x_i x_j}{r^5} + \cdots \right], \quad (1.1)$$

where $\rho(\vec{x'})$ is the charge density. The lowest order expansion coefficients are:

a) Total charge $q$:

$$q = \int \rho(\vec{x'}) \, \mathrm{d}^3 x', \tag{1.2}$$

b) Electric dipole moment $\vec{d}$:

$$\vec{d} = \int \vec{x'} \rho(\vec{x'}) \, \mathrm{d}^3 x', \tag{1.3}$$

c) Electric quadrupole moment $Q_{ij}$:

$$Q_{ij} = \int \left( 3x_i' x_j' - (r')^2 \delta_{i,j} \right) \rho(\vec{x'}) \, \mathrm{d}^3 x'. \tag{1.4}$$

As Nagashima states in Ref. [10]: "When an object is a particle like the neutron, regardless of finite or point size, its only attribute that has directionality is spin $\vec{\sigma}$. If the particle has finite $\vec{d}$, it has to be proportional to $\vec{\sigma}$. While the transformation property of $\vec{\sigma}$ under P [parity transformation, reversing of signs on all space coordinates $x \to -x$] and T [time reversal transformation] is even, odd, respectively, that of $\vec{d}$ is odd, even as seen from Eq. (1.3). Therefore the existence of the EDM of particle violates both P and T. As the neutron is a neutral composite of quarks, its EDM can be a sensitive test of T-reversal invariance in the strong interaction sector as well as in the weak interaction."

## 1.3   Measurements of the neutron electric dipole moment
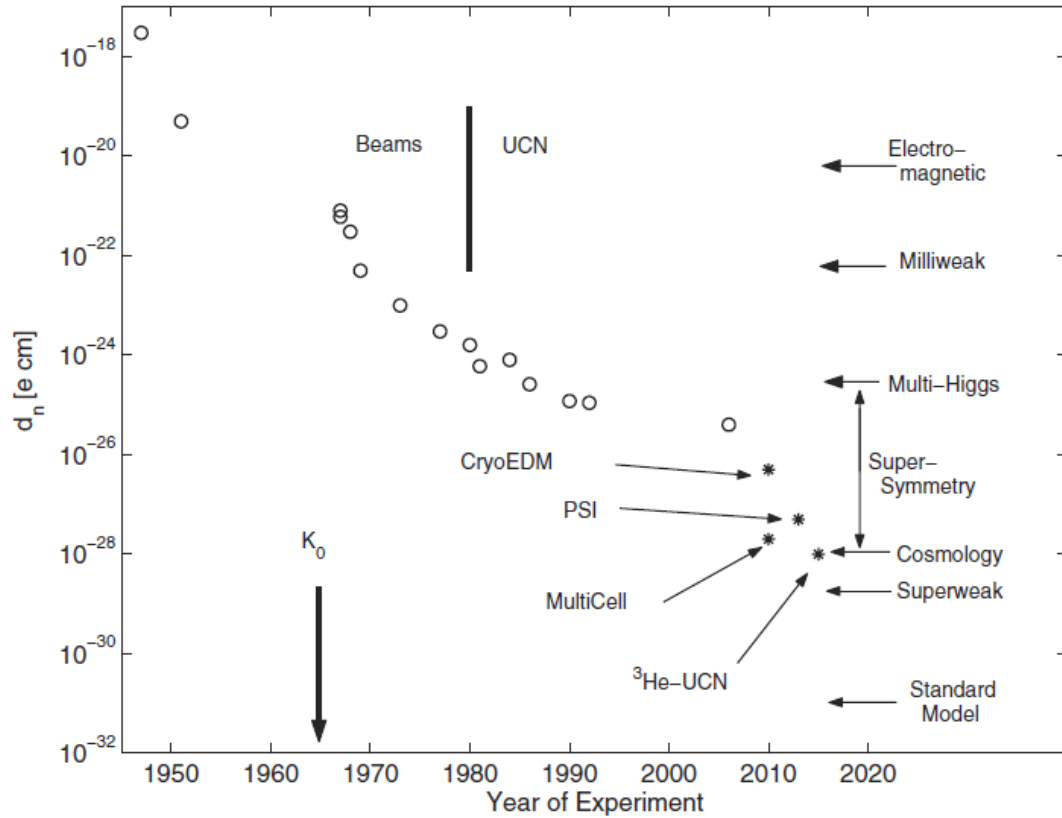


Figure 1.1: The history of measurements of the neutron electric dipole moment. Predictions of various models and theories are marked on the right. Stars mark predicted sensitivity of measurements. First discovery of CP violation in the neutral kaon system is marked with an arrow. Taken from Ref. [11]

The first direct measurement of the neutron electric dipole moment was performed by Smith, Purcell and Ramsey in 1957 [12]. They used a beam of polarized neutrons and applied the magnetic resonance technique and obtained an upper limit for the neutron EDM $d_n < 5 \cdot 10^{-20}$ e · cm.

Instead of neutron beam experiments, using ultra-cold neutrons (UCNs) stored in material vessels, so called bottles, is more common nowadays. The latest and the most accurate result is from 2007. The RAL-Sussex-ILL collaboration obtained the limit of $d_n < 2.9 \times 10^{-26}$ e · cm using stored ultra-cold neutrons produced at the Institut

Laue-Langevin in Grenoble [13].

The history of measurements of the neutron electric dipole moment is illustrated in Fig. 1.1. The most important new measurements are also marked. They are described in detail in Ref. [11].

Nevertheless, there are attempts to go back to beam measurements of the nEDM. The last experiment using this method was performed by Dress et al. in 1977 [14]. Recently, a new proposal was published by Piegsa [15]. He suggests using pulsed cold neutron beams in a scenario suppressing the main systematic effects of measurement.

## 1.4 Ultra-cold neutrons

All modern measurements of the neutron electric dipole moment are performed using ultra-cold neutrons (UCNs) - the neutrons with such sufficiently low kinetic energy that they cannot surpass the repulsive potential barrier of certain solid or liquid materials or magnetic field configurations forming so called bottles.

As J. Byrne states in [16], Fermi was the first to recognize that cold neutrons propagate in condensed matter in a way similar to the propagation of light waves. The refractive index for most materials is less than unity – which means that neutrons are totally reflected when incident at glancing angles $\theta$, which satisfy the inequality (Ref. [16]):

$$\theta \leq \sin^{-1}\left[(V_F/E_n)^{1/2}\right], E_n \geq V_F, \tag{1.5}$$

where:

$$V_F = \frac{2\hbar^2}{m_n}Nb, \tag{1.6}$$

is the Fermi pseudo-potential, $b$ is the bound coherent scattering length, $E_n$ is the neutron kinetic energy, $N$ is the density of nuclei in the material.

Total reflection at all incident angles appears when $E_n \leq V_F$ which allows for storage of neutrons in material containers. Owing to the fact that the largest positive $V_F$ is equal 346 neV for $^{58}$Ni, corresponding to $v \approx 8$ m/s, the neutrons with kinetic energy between $0 - 346$ neV ($0 - 8$ m/s) are called ultra-cold neutrons. For reference a few most notable examples of Fermi pseudopotential values are collected in Tab. 1.1.

What can also be seen in Tab. 1.1, is the fact that iron can be used as a material

Table 1.1: Example materials with their Fermi pseudopotential, taken from Ref. [17]. Arrows indicate parallel and anti-parallel orientation of the magnetic moment of the neutrons and of the sample.

| material | $V_F$ [neV] |
|---|---|
| Al | $54 \pm 10$ |
| Si | $50 \pm 10$ |
| Diamond on Si | $286 \pm 32$ |
| Diamond Like Carbon on Si | $271 \pm 13$ |
| Diamond Like Carbon on Al | $249 \pm 14$ |
| One layer Be on Si | $249 \pm 7$ |
| Fe $\uparrow\uparrow$ | $351 \pm 14$ |
| Fe $\uparrow\downarrow$ | $72 \pm 8$ |
| $^{58}$Ni | 346 [18] |

for polarizing neutrons. If neutrons have kinetic energy between $72$ neV $> E_{kin} > 351$ neV and if the iron foil is magnetized, only neutrons with magnetic moment anti-parallel to the foil magnetization would go through it. This property is also used by the nEDM experiment at PSI for selecting neutrons with only one spin direction.

### 1.4.1 Principle of the neutron EDM measurement

Measurement of the neutron electric dipole moment is based on the neutron's interaction with the electrical and magnetic fields.

**Interaction with electrical and magnetic fields**

Neutrons, although being electrically neutral, have a non-zero magnetic moment $\mu_n$. The magnitude of the neutron magnetic moment $\mu_n$ was measured already in 1940 by Alvarez and Bloch [19]. Present value is $\mu_n = -1.91304272\mu_N$, where $\mu_N = \frac{e\hbar}{2m_p}$ is called nuclear magneton, $m_p$ being the proton mass. Electric dipole moment $\vec{d}_n$ and magnetic moment $\vec{\mu}_n$ cause the interaction term of the neutron Hamiltonian in the presence of the electromagnetic field:

$$\mathcal{H} = -\vec{\mu}_n \cdot \vec{B} - \vec{d}_n \cdot \vec{E}, \tag{1.7}$$

where: $\vec{B}$ and $\vec{E}$ represent magnetic induction and electric field, respectively. Comparing the interaction energy of a parallel and anti-parallel electric and magnetic field, one observes the shift:

$$h\nu_{\substack{\uparrow\uparrow \\ \uparrow\downarrow}} = 2\mu_n B \pm 2d_n E, \tag{1.8}$$

where $h$ is Planck constant, $\nu_{\substack{\uparrow\uparrow \\ \uparrow\downarrow}}$ is the precession frequency of the neutron in parallel/anti-parallel magnetic and electric fields, and the $\pm$ sign corresponds to parallel/anti-parallel $\vec{E}$ and $\vec{B}$ respectively. From Eq. (1.8), assuming separate measurements for parallel ($\uparrow\uparrow$) and anti-parallel ($\uparrow\downarrow$) field configurations, we can calculate the neutron electric dipole moment:

$$d_n = \frac{h\left(\nu_{\uparrow\uparrow} - \nu_{\uparrow\downarrow}\right)}{4E}. \tag{1.9}$$

**The Rabi single coil resonance method**
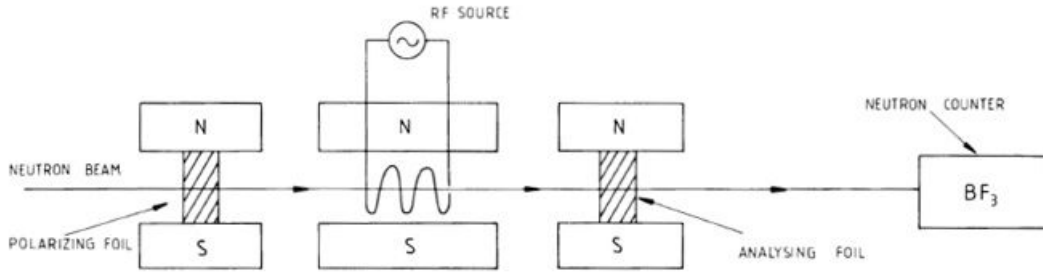


Figure 1.2: Apparatus used by Alvarez and Bloch to measure the neutron magnetic moment. Taken from Ref. [16]

The Rabi single coil resonance method was used in the first measurement of the neutron magnetic moment. Alvarez and Bloch used an apparatus presented in Fig. 1.2 to measure the neutron's precession frequency in a given magnetic field. As Byrne states in Ref. [16], "The state of a neutron beam with an arbitrary degree of partial polarization may be characterized by its four Stokes parameters $(P_0, \vec{P})$, when $P_0$ is the total intensity and $\vec{P}/P_0$ is an axial vector in position space, which may be identified with the expectation value of the spin. In a uniform magnetic field $\vec{B}_0$, the component of $\vec{P}$ normal to $\vec{B}_0$ precesses about $\vec{B}_0$ with Larmor angular frequency given by:

$$\hbar\omega_0 = \hbar\gamma_n B_0, \tag{1.10}$$

where $\gamma_n$ (<0) is the gyromagnetic ratio. When a weak magnetic field $\vec{B}_1$ is superimposed in a plane normal to $\vec{B}_0$ rotating with angular frequency $\omega$ in the same sense as the free precession, the Stokes vector carries out a forced precession. Thus, when $\omega = \omega_0$, the neutron spin senses a constant weak field when viewed from a frame of reference rotating with angular velocity $\omega$, and a resonance occurs which is similar to any classical resonance phenomenon."

In the Alvarez and Bloch experiment, neutrons in a beam are polarized passing through a polarizing foil – an iron foil brought in the saturation by magnets. Then, polarized neutrons pass through uniform magnetic field $\vec{B}_0$ and a superimposed oscillating $\vec{B}_1$ field. If frequency of the $\vec{B}_1$ field satisfies the resonance condition, neutron polarization is changed to opposite one, if the interaction time is chosen properly. This kind of magnetic field pulse is called $\pi$ pulse.



Figure 1.3: Probability of change of spin state (Eq. (1.11)) as a function of applied frequency of oscillating magnetic field for three different interaction times. Taken from Ref. [16].

Neutrons' polarization is measured by counting how many neutrons pass through the analysing foil in the Rabi method [16]. The change of this number with changing frequency of the $\vec{B}_1$ field can be described by the transition probability of the spin state:

$$W_{12}(\omega, t) = \frac{(b)^2 \sin^2\left(\frac{t}{2}\sqrt{(\omega_0 - \omega)^2 + (b)^2}\right)}{(\omega - \omega_0)^2 + (b)^2},$$

$$(1.11)$$

where $b = \gamma_n B_1$. This relation as a function of applied frequency for three different values of time of application of the oscillating field is shown in Fig. 1.3.

**The Ramsey method of separated oscillatory fields**

The Rabi method can be compared to a single slit optical experiment. Equivalent of a double slit experiment would then be the Ramsey method of separated oscillatory fields. A single application of an oscillating field $\vec{B}_1$ is replaced by the shorter $\vec{B}_1$ pulses separated by a free precession time $T$ in a constant field $\vec{B}_0$. This method gives a much narrower central resonance fringe than that of the Rabi method. The resonance curve allows for a more accurate estimation of the transition frequency, thus the energy shift between parallel and anti-parallel field configurations. The details of the Ramsey method of separated oscillatory fields are illustrated in Fig. 1.4.

**a)** Polarized neutrons (all of the neutrons in the population are in the "up" state) are in volume, where magnetic and electric fields are either parallel or anti-parallel. This field configuration causes neutrons' spins to precess around the direction of both field vectors, resulting in net polarization of neutrons to be along the direction of both fields.

**b)** Oscillating magnetic field $\vec{B}_1$ perpendicular to the main field direction is applied. Duration of this pulse is tuned, so that the average polarization of neutrons after its application is 0. This pulse is called a "$\pi/2$" pulse because in the rotating (with the $\omega = \omega_L$) frame of reference, the neutron's spin direction is rotated by $\pi/2$.

**c)** The spins of neutrons are precessing in the plane perpendicular to the main field direction with $\omega = \omega_L$.

**d)** Second $\pi/2$ magnetic field pulse is applied to neutrons. Their spins are rotated again by $\pi/2$, leading again to non-zero net polarization.
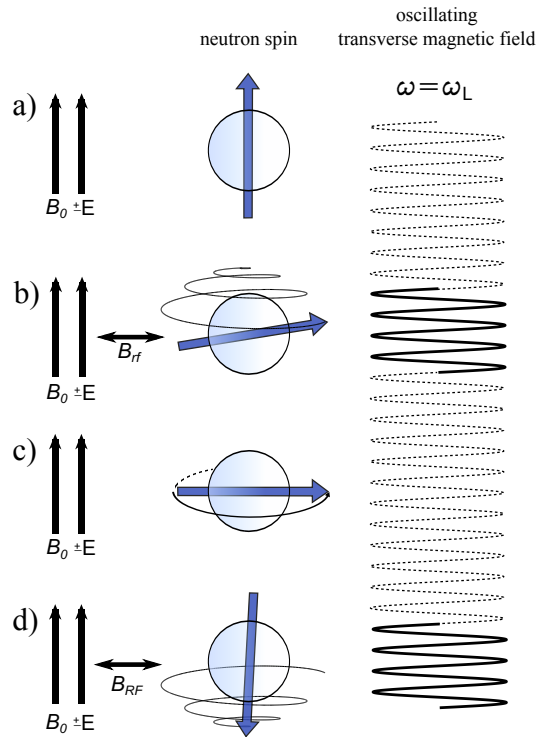


Figure 1.4: Scheme of the Ramsey method of separated oscillatory fields
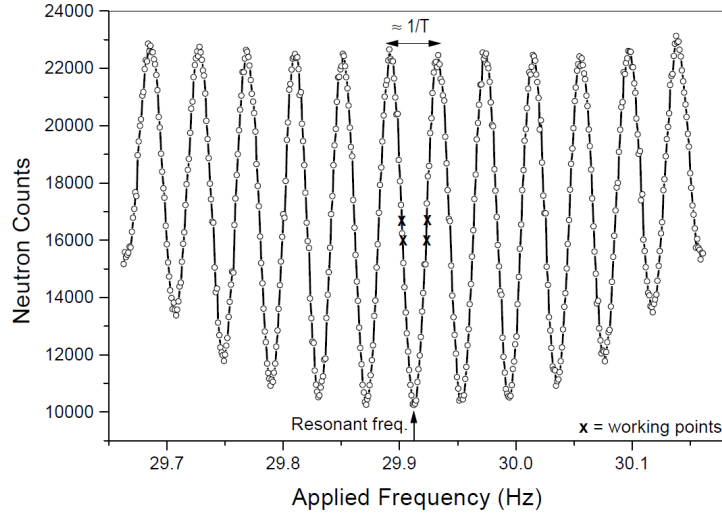
Figure 1.5: A magnetic resonance curve, showing the number of neutrons in the "up" state reaching detector after application of $\pi/2$ pulse, free precession and second $\pi/2$ pulse as a function of frequency of $\pi/2$ pulses. Measurement done by RAL-Sussex-ILL collaboration (see Ref. [20]).

The central fringe in the Ramsey resonance curve (Fig. 1.5), corresponding to neutrons in the "up" state after application of the Ramsey method of separated oscillatory fields, can be described by:

$$N_{up}(\Delta\nu) = N_{up}\left(1 - \alpha\cos\left(\Delta\nu T\right)\right), \tag{1.12}$$

where $N_{up} = (N_{max} + N_{min})/2$ and $\alpha = (N_{max} - N_{min})/(N_{max} + N_{min})$ is the, so called, visibility factor and $T$ is the free precession time. From this equation, it is clearly visible that the width of the central fringe of the Ramsey pattern is proportional to $1/T$, making it important to allow neutrons to precess as long as possible.

From equations (1.12) and (1.9) it is possible to calculate [21] the expected statistical uncertainty of the electric dipole moment obtained by the Ramsey's method of separated oscillatory fields:

$$\sigma\left(d_n\right) = \frac{\hbar}{2E\alpha T\sqrt{NM}}, \tag{1.13}$$

with $E$ - electric field, $N = N_{up} + N_{down}$ total number of neutrons and $M$ – the number of repetitions of the measurement.

**Influence of magnetic field changes on the Ramsey method of oscillatory fields**

Equation (1.9) was obtained under the assumption that the magnetic field has not changed between measurements with parallel and anti-parallel fields. Without this simplification, the neutron electric dipole moment can be expressed as:

$$d_n = \frac{(\nu_{\uparrow\uparrow} - \nu_{\uparrow\downarrow}) - \mu_n \left(B_{\uparrow\uparrow} - B_{\uparrow\downarrow}\right)}{2 \left(E_{\uparrow\uparrow} + E_{\uparrow\downarrow}\right)}, \tag{1.14}$$

where $B_{\uparrow\downarrow}$, $E_{\uparrow\downarrow}$ are norms of magnetic induction and electric field vectors during the measurement with anti-parallel fields and $B_{\uparrow\uparrow}$, $E_{\uparrow\uparrow}$ correspond to parallel fields. This equation shows that it is crucial to control changes of magnetic field contributing to the fake term $\mu_n \left(B_{\uparrow\uparrow} - B_{\uparrow\downarrow}\right)$.

In the proceeding parts of this thesis, the topic of suppressing the changes in magnetic field is addressed. Several active magnetic shielding setups are considered. The field changes, still remaining after compensation, are to be measured using magnetometers.

# Chapter 2

# The nEDM experiment at the Paul Scherrer Institute

The nEDM experiment at the Paul Scherrer Institute is a joint project of a group consisting of over 60 scientists from various countries. This collaboration is working on improving the measurement sensitivity of the neutron electric dipole moment. To achieve that, the first pulsed spallation UCN source in the world was built in Paul Scherrer Institute. With the use of neutrons from this source, there are ongoing measurements of neutron EDM, using parts of the old setup developed by the RAL-Sussex-ILL collaboration (see Ref. [13]).

## 2.1   UCN Source at Paul Scherrer Institute

For measurement of the neutron electric dipole moment at the Paul Scherrer Institute, the spallation based UCN source is used. Its scheme is shown in Fig. 2.1. Protons arrive from the $590$ MeV PSI proton ring accelerator and hit the spallation target made of Zircalloy tubes filled with lead [23].

Spallation neutrons have the energy spectrum with the mean value around $2$ MeV. They are slowed down in a room temperature $D_2O$ moderator. To the ultra-cold regime, they are decelerated in deuterium crystal by inelastic scattering. Most of their kinetic energy is transformed to excitations of the scattering medium.

Resulting energies of the neutrons are below $500$ neV. Earth's gravitational field
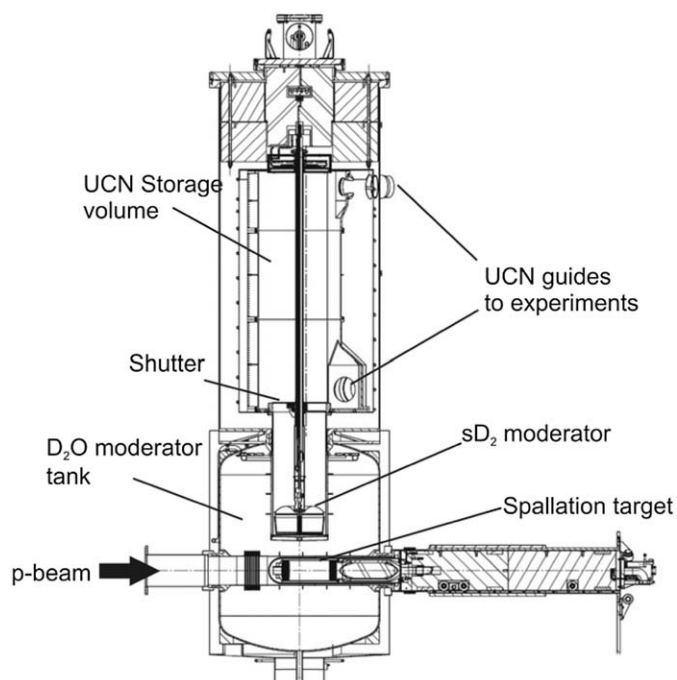
Figure 2.1: Scheme of the ultra-cold neutron source at the Paul Scherrer Institute. The marked components of the system are described in the text. Image taken from [22].

causes the neutrons' energy to lower even more while going up to the UCN Storage volume. Only ultra-cold neutrons can be stored there, since all neutrons with higher energies are absorbed by walls coated with diamond-like carbon.

From storage volume, neutrons are transported through UCN guides to the nEDM experiment and other experiments.

## 2.2 EDM Spectrometer

Neutrons from the UCN source (see Fig. 2.2) get polarized in the axial field of the super-conducting magnet and reach the switch section. A mechanical switch directs neutrons up to the precession chamber located inside a 4-layer shield built from Mumetal, metallic alloy with high magnetic permeability.

Inside the precession chamber, a $1\mu$T vertical magnetic field is applied together with an electric field of magnitude over $10$ kV/cm.

After the storage cell is filled with neutrons, the mercury entrance shutter is opened
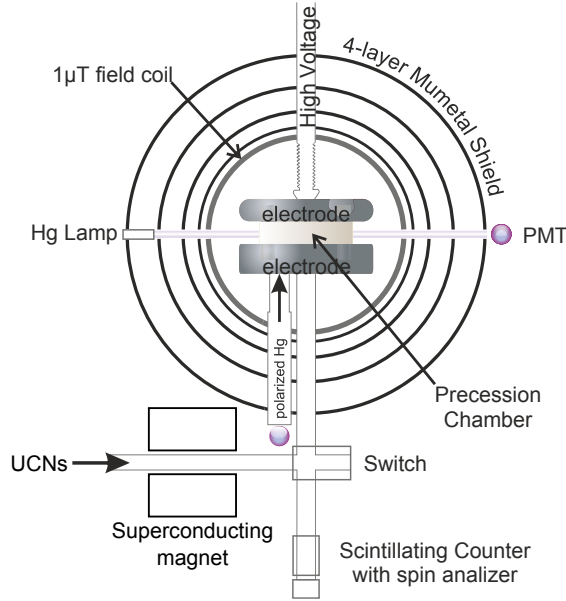
Figure 2.2: Scheme of nEDM apparatus

and polarized $^{199}$Hg atoms diffuse to the precession chamber. During the experiment, there are about $3 \cdot 10^{10}$ Hg atoms/cm$^3$ in the precession chamber. Then, two radio frequency $\pi/2$ pulses are applied. The first pulse is applied at the Larmor frequency of $^{199}$Hg $f_{Hg} \approx 7.7$ Hz to force mercury magnetic moments to precess in plane perpendicular to the main field direction. Immediately after that, a second pulse is applied with frequency $f_n \approx 30$ Hz. This is the beginning of the Ramsey sequence for neutrons: neutron spins start precessing in the plane perpendicular to the main field direction. The free precession takes about $200$ s. After this time, the second $\pi/2$ pulse with the $f_n$ frequency is applied (see Sec. 1.4.1).

After that, neutrons exit through the entrance window and reach the switch, which directs them to the scintillating neutron detector.

## 2.3 Neutron detection

To increase the number of counted neutrons, simultaneous spin analysis is used, contrary to the sequential one utilized by the RAL-Sussex-ILL experiment [13]. Here, two spin components of the UCN ensemble are counted separately. This results in two identical arms of the polarimeter, as shown in Fig. 2.4. In the left arm, where the adiabatic
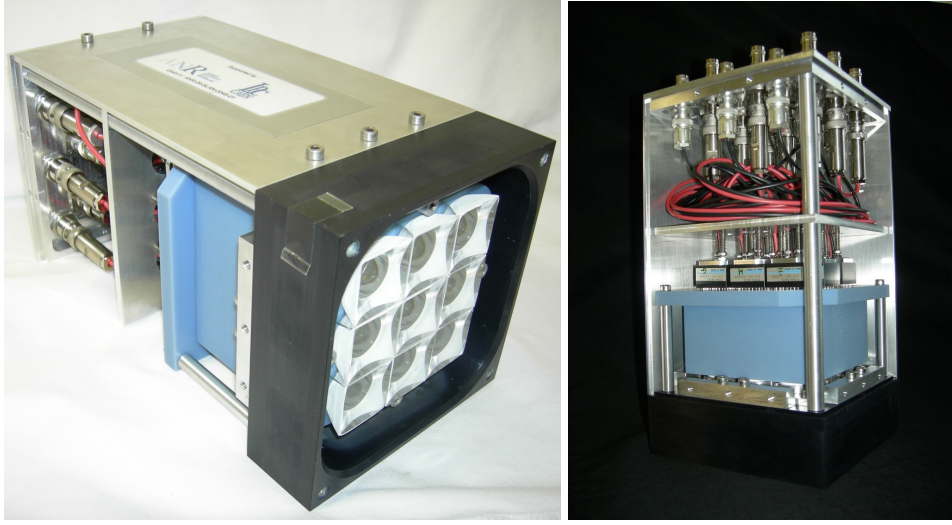
Figure 2.3: NANOSC - NANO SCintillator.

spin flipper (ASF) is on, the spin up component is analysed whereas in the right arm, where the ASF is off, the spin down component is measured. As a result, the waiting time above the analysing foils is reduced and UCN losses, as well as depolarizations, are minimized. During this operation, neutrons with initial spin down (up) will be rejected on the analysis foil of the left (right) arm. An important goal in the design of the simultaneous spin analyser was to optimize the transport of "wrong spin" neutrons from one arm to the other in the transit volume above the two arms. Optimal geometry was determined with Geant4-UCN simulations [24].

For a detecting device, we use a $^6$Li doped glass scintillator with photomultiplier tubes for readout of light. The detectors are shown in Fig. 2.3. This detector utilizes the neutron capture reaction:

$$n + {}^6\text{Li} \rightarrow {}^3\text{H}(2.74 \text{ MeV}) + {}^4\text{He}(2.05 \text{ MeV}).$$

Cross-section for this reaction for thermal neutrons is 940 barns. This cross-section follows the $1/v$ rule and though it leads to order of $10^5$ barns for velocities of ultra cold neutrons.

Detector pulses are digitized and sorted according to respective amplitudes with the help of FASTER (the Fast Acquisition System for nuclEar Research) – data acquisition system, which is specially designed by LPC Caen for nuclear physics experiments.
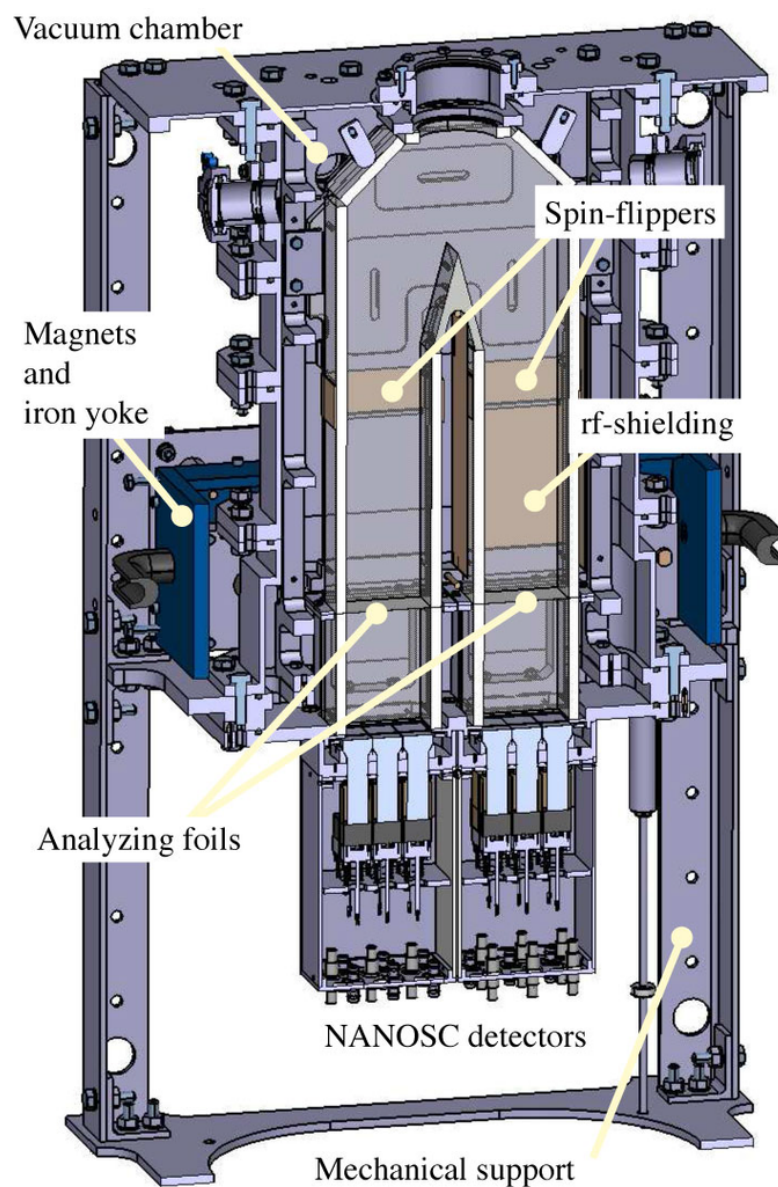
Figure 2.4: Scheme of the U-shaped Simultaneous Spin Analyser detector system

## 2.4 Systematic effects

Careful investigation of systematic effects which affect the result of measurement in this experiment is crucial. Current limits are presented in Tab. 2.1. A detailed description of all of these effects can be found in Ref. [21].

Table 2.1: Known systematic effects of the nEDM experiment (from [21]).

| Effect | Shift to neutron EDM $[10^{-27}\mathrm{e} \cdot \mathrm{cm}]$ |
|---|---|
| Leakage currents | $0.00 \pm 0.05$ |
| $v \times E$: | |
| first order | $0.00 \pm 1.70$ |
| second order | $0.00 \pm 0.00$ |
| Electric forces | $0.00 \pm 0.00$ |
| AC fields | $0.00 \pm 0.00$ |
| Uncompensated B field drifts | $-0.1 \pm 0.4$ [25] |
| $^{199}$Hg atom EDM | $0.02 \pm 0.06$ |
| $^{199}$Hg light shifts | $0.00 \pm 0.27$ |
| Geometric phase effect: | |
| Dipole fields | $0.00 \pm 0.00$ |
| Quadrupole difference | $0.56 \pm 0.90$ |
| Total | $0.48 \pm 1.98$ |

In the following chapters, the systematic effects related to magnetic field which are influenced by either magnetic field shielding or magnetic field mapping are described. They are the main topics of this dissertation.

### 2.4.1 Geometric phase effect

Particles with a magnetic moment exposed to a magnetic field, $\vec{B}_0 = B_0\hat{z}$ precess at the Larmor frequency $f_L = \gamma B_0/2\pi$, where $\gamma$ is the gyromagnetic ratio. Because of experimentally unavoidable magnetic field gradients, the Larmor frequency of a particle moving through this field will be subject to a shift, known as the Ramsey-Bloch-Siegert (RBS) shift [26]. If an electric field $\vec{E}$ (parallel or anti-parallel to $\vec{B}_0$) is applied - as is the case in experiments searching for EDMs - the moving particle will experience an additional motional magnetic field $\vec{B}_v = \vec{E} \times \vec{v}/c^2$. It is the interplay between this field

and the magnetic field gradients that lies at the origin of a frequency shift proportional to the electric field strength, thus inducing a false EDM.

The first detailed calculation of such false EDMs for stored particles was given in Ref. [27, 28] in the context of the RAL-Sussex-ILL neutron EDM experiment [13]. The authors derived expression for the two limiting cases: non adiabatic and adiabatic, corresponding to $2\pi f_l \tau \gg 1$ and $2\pi f_l \tau \ll 1$ respectively, where $\tau$ is the typical time particles take to cross the trap. Both regimes are of interest, since $^{199}$Hg atoms fall into the first category whereas UCNs fall into the second. More general results, valid for a broad range of frequencies, were obtained only for cylindrical symmetry and specular reflections. The expressions of the frequency shifts for the two limiting regimes are:

$$\delta f_L = \frac{\gamma^2 D^2}{32\pi c^2} \frac{\partial B_0}{\partial z} E \quad \text{(non adiabatic)} \tag{2.1}$$

$$\delta f_L = \frac{v_{xy}^2}{4\pi B_0^2 c^2} \frac{\partial B_0}{\partial z} E \quad \text{(adiabatic)}, \tag{2.2}$$

where $\gamma$ is the gyromagnetic ratio, $D$ is the diameter of the trap, $c$ is the velocity of light and $v_{xy}$ is the particle velocity transverse to $\vec{B}_0$. Note the absence of the gyromagnetic ratio in Eq. (2.2). Indeed, in the adiabatic case, the frequency shift can be interpreted as originating from a phase of purely geometric nature, or Berry's phase [29, 30], and is therefore independent of the coupling strength to the magnetic field.

These results were then complemented and extended using the general theory of relaxation (Redfield theory) [31, 32] and then by solving the Schrödinger equation directly [33]. In Ref. [32], an expression valid for arbitrary field distributions or trap shapes was obtained in the non-adiabatic limit:

$$\delta f_L = \frac{\gamma^2}{2\pi c^2} \langle x B_x + y B_y \rangle E \quad \text{(non adiabatic)}, \tag{2.3}$$

where the brackets refer to the average over the storage volume. For a cylindrically uniform gradient and a trap with cylindrical symmetry, Eq. (2.1) reduces to (2.3). Using the relationship between the frequency shift and the false EDM,

$$d^{false} = \frac{h}{2E} \delta f_L(E), \tag{2.4}$$

where $h$ is Planck's constant. Together with Eqs. (2.2) and (2.1), one can now readily calculate the magnitude of the false EDMs for the mercury and for the neutron (both direct and resulting from the false EDM of $^{199}$Hg). Given our experimental conditions and assuming a neutron velocity of 3 m/s, one obtains:

$$d_n^{false} = \frac{\partial B_0}{\partial z} 1.490 \cdot 10^{-29} e\text{cm/(pT/cm)} \tag{2.5}$$

$$d_{Hg}^{false} = \frac{\partial B_0}{\partial z} 1.148 \cdot 10^{-27} e\text{cm/(pT/cm)} \tag{2.6}$$

$$d_n^{false,Hg} = \frac{\partial B_0}{\partial z} 4.418 \cdot 10^{-27} e\text{cm/(pT/cm)}, \tag{2.7}$$

where $d_n^{false}$ is false EDM of neutrons, $d_{Hg}^{false}$ is false EDM of Hg atoms and $d_n^{false,Hg}$ is false EDM of neutrons inducted by false EDM of mercury.

Considering a typical value of 10 pT/cm for the vertical ($z$ direction) gradient in our setup, we can conclude, on the one hand, that the direct false neutron EDM is negligible, at least at the current level of sensitivity. On the other hand, the mercury induced false neutron EDM is a major systematic error that must be properly taken into account.

To take this error into account, control and careful investigation of magnetic field in the place of the experiment must be conducted.

To suppress the magnetic field gradients, generating the effect described above, passive and active shielding are used. The comparison of active compensation systems is the main topic of this dissertation and is presented in Part II.

The analysis of results of the mapping campaign, which was performed to gather information about magnetic field distribution in the volume occupied by the precession chamber, is presented in Part III of this dissertation.

## 2.5 Magnetic field nonuniformity

In the experiment measuring nEDM at the Paul Scherrer Institute, mercury cohabiting magnetometer is used to monitor changes of magnetic field during free precession time. This sensor measures magnetic field averaged over volume occupied by $^{199}$Hg vapour. This vapour is at room temperature, which results in uniform distribution of mercury atoms inside the whole precession chamber.

Ultra-cold neutrons interact gravitationally with matter. Because their thermal kinetic energy is very low, the gravity has a non-negligible impact on their trajectories in the bottle, resulting in larger density near the bottom. The difference of centres of gravity of neutrons and mercury atoms is about $2.5$ mm. This means that, on average, neutrons may interact with slightly different magnetic field than mercury atoms.

Non-uniform magnetic field leads also to spin-spin relaxation of both neutrons and mercury atoms. This is a result of different spin precession frequencies at different places in the precession chamber, which causes a self-depolarization of medium. This phenomenon is described by $T_2$ time, which is the measure of time needed for polarization to decrease by $1/e$. In order to improve the precision of measurement (see Eq. (1.13)), it is preferred to increase the free precession time. The larger $T_2$ time is, the more neutrons will still be polarized after a given free precession time.

The value of the magnetic field vertical gradient can be extracted in two ways. It is done either by analysis of the ratio of gyromagnetic ratios of neutrons and mercury atoms ($R = \gamma_n/\gamma_{Hg}$) as a function of externally applied vertical magnetic field gradients [34] or by direct measurement using a dedicated magnetometer. During this work direct data was analysed, which is presented in Part III.

The higher orders of the vertical magnetic field nonuniformity present in the precession chamber are harder to measure and apply corrections for. The main goal of magnetic field shielding, both passive and active, is to provide a sufficiently uniform and stable magnetic field. R&D works on improving the existing system of magnetic field compensation are presented in Part II.

## 2.6 Magnetic field control systems

Magnetic field is a crucial source of uncertainties in the nEDM measurement. Due to this fact, systems gathered in Fig. 2.5 are being used. They can be divided into two types:

**Magnetic field monitoring** - Measurement systems allowing us to correct for changes in magnetic field. Here we use two magnetometer systems: a mercury cohabiting magnetometer and caesium magnetometers

**Magnetic field generation/shielding**  - Coil systems and shields allowing us to change
the magnetic field to improve sensitivity of nEDM measurement.
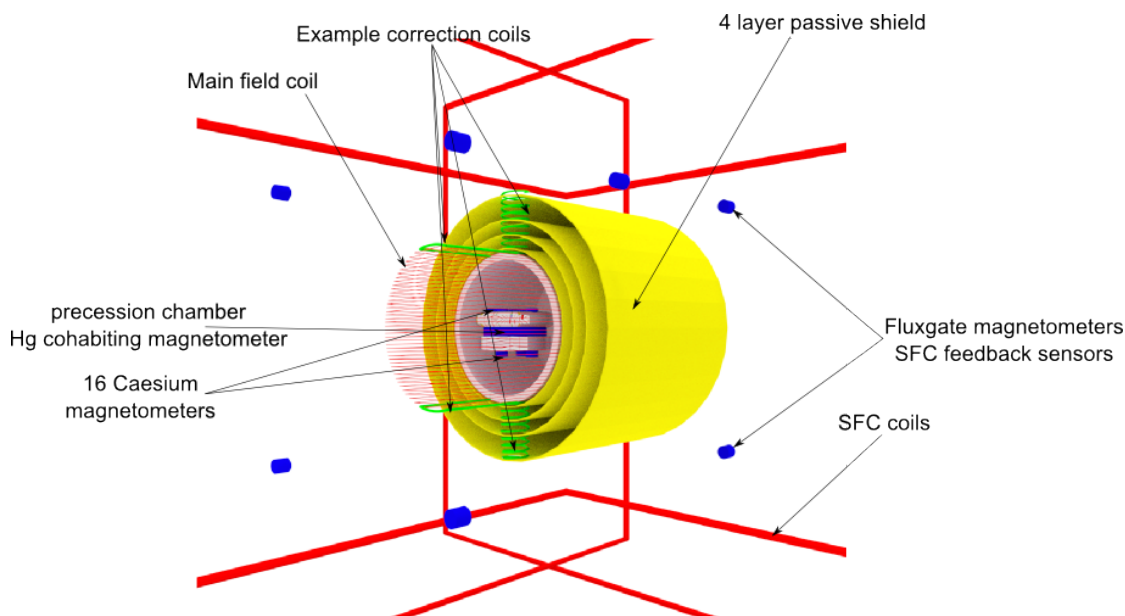


Figure 2.5: Summary of magnetic field control components

## 2.6.1   Magnetic field monitoring

Monitoring of the magnetic field during measurement of the electric dipole moment
is crucial (for discussion, see Sec. 1.4.1). It is necessary to respect variations of the
ambient magnetic field in evaluation of the nEDM measurement. A spectacular effect
of the corrections of the magnetic field variation is shown in Fig. 2.6. Without those
corrections, magnetic field changes dominate other effects, including nEDM itself.

In the nEDM experiment at the Paul Scherrer Institute, the magnetic field in the
precession chamber is monitored by the following systems:

**Mercury cohabiting magnetometer.** Measurement with this instrument is based on
determination of the precession frequency of polarization of $^{199}$Hg atoms in the
magnetic field inside precession chamber. This frequency is proportional to the
average magnetic field inside the chamber since the $^{199}$Hg atoms move randomly
and uniformly inside the precession chamber. Circularly polarized light passes
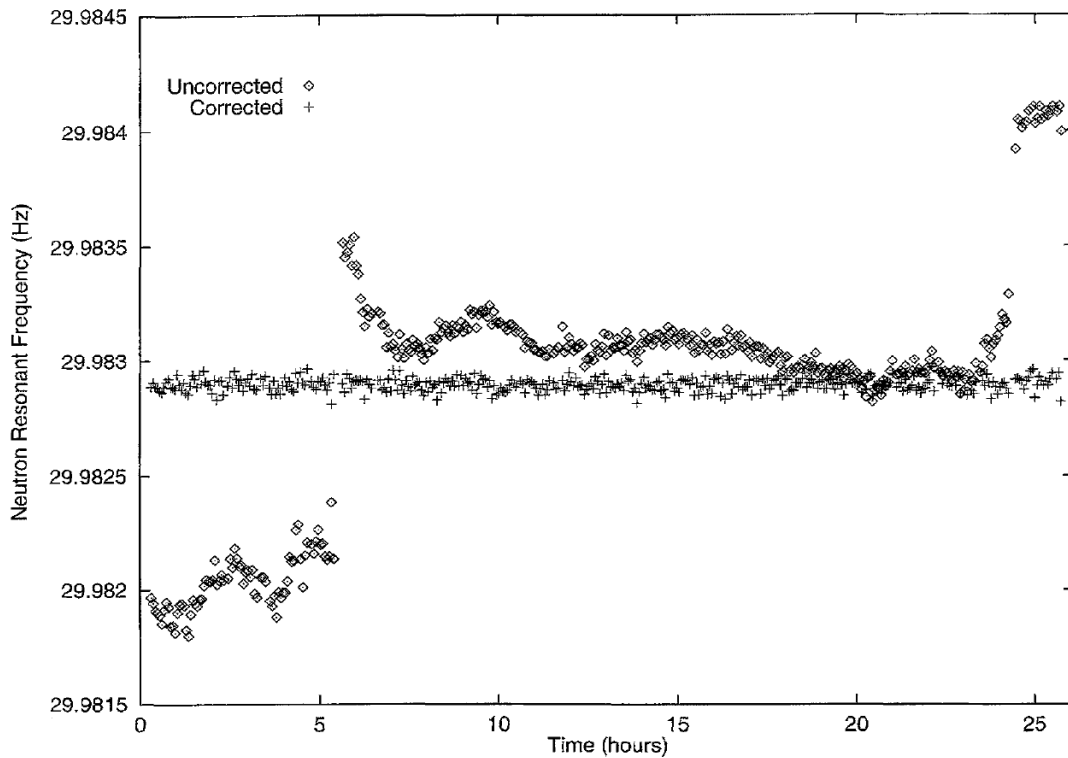
Figure 2.6: Larmor frequency of neutrons during RAL-Sussex-ILL experiment with and without corrections for changing magnetic field. Figure taken from [35]

through the precession chamber, being partially absorbed, depending on the relative orientation of the $^{199}$Hg polarization and the Poynting vector of the light wave. In effect, the detected intensity at the end of its path is proportional to the average polarization of the $^{199}$Hg atoms. The transmitted light is sampled during the whole free precession time of the Ramsey cycle.

**Caesium magnetometer.** Measurement with this sensor is based on measurement of precession frequency of $^{133}$Cs atoms enclosed in a glass bulb with a diameter of 2 cm. The caesium atoms are optically pumped by a circularly polarized light, oriented at $45°$ with respect to the magnetic field direction. A diode laser provides the resonant light, which is then transmitted through the cell and carried back to the detection unit. The pumping process produces a polarization in the sample which precesses with Larmor frequency $\omega_L$. The weak radio-frequency field is driving this precession. The absorption of the pumping light depends on

the direction of the magnetization with respect to the light direction, like in the Mercury magnetometer. The measurement of the modulation frequency allows to calculate the magnitude of the magnetic field vector.

**Fluxgate sensors.** These sensors are working on another principle. The excitation coil with current produces an oscillating magnetic field, which periodically saturates the sensor core made up of soft magnetic material. Core permeability is lowered in saturation, causing flux associated with magnetic field to be decreased. In the second (pick-up) coil, the voltage is induced. This voltage is usually the sensor output and it is proportional to the measured field. In the nEDM experiment at the Paul Scherrer Institute, fluxgate sensors are used for feedback in the active field compensation system.

## 2.6.2 Main field coil and correction coils
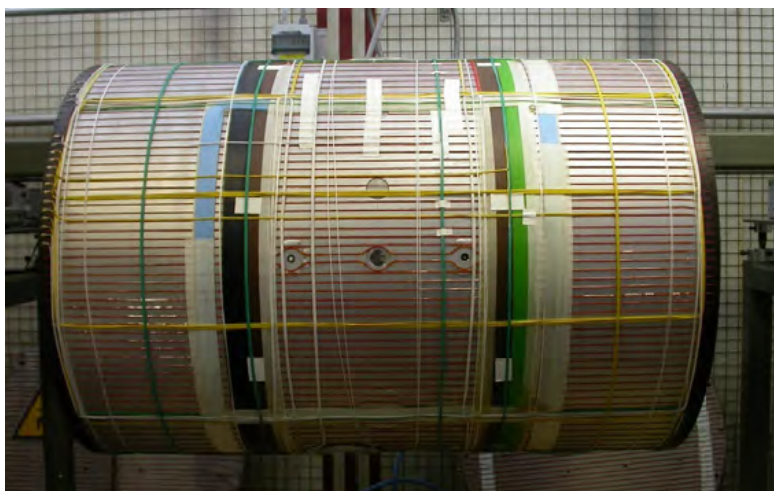


Figure 2.7: Main field coil and correction coils wound around the surface of the vacuum tank

The main field coil (called $B_0$ coil) is designed to provide an uniform vertical magnetic field in the precession chamber. This is the so-called $\cos\theta$ coil, wound around the surface of a cylindrical vacuum tank (see Fig. 2.7). It generates $1\ \mu$T field using $17$mA current flowing through it. Since the $B_0$ coil is contained inside the innermost passive shielding layer, the generated field interacts with ferromagnetic material such that the

precession chamber volume is exposed to the effective field from the $B_0$ coil and from the shielding.

The $B_0$ coil is assisted by a set of 33 correction coils (shown in Fig. 2.8) helping to reduce the field imperfections produced by the $B_0$ coil and the shield. It is a big challenge to find the optimal trim coil currents that should be driven such that the field inside the precession chamber is perfectly uniform.



(a) Left and Right Correction Coils    (b) Top, Bottom and Helmholtz correction coils
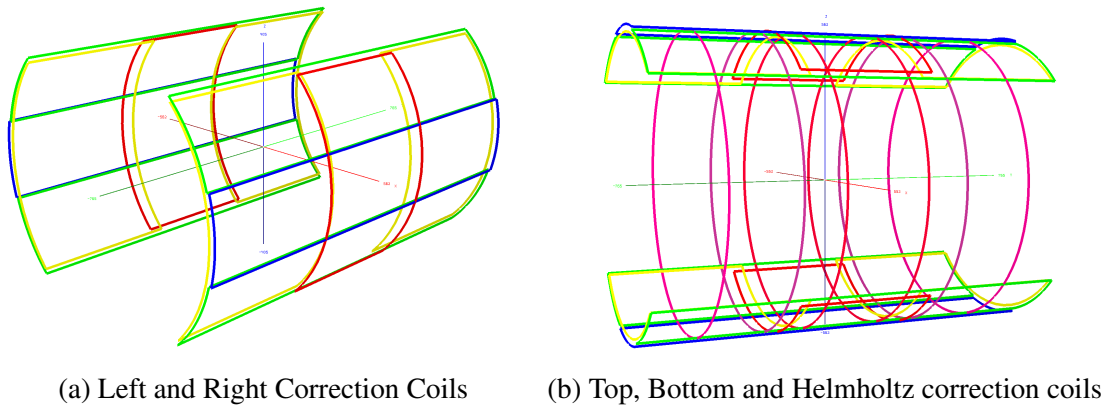
Figure 2.8: Correction coils

The naming scheme for the correction coils is related to their location. The first letters (B - bottom, T - top, L - left, R - right) represent the coil positions, while H stands for the three paired Helmholtz coils.

There are also additional coils wound around mercury and neuron guides to ensure that transported neutrons will not lose their polarization.

A large number of coils and complexity of the apparatus make it difficult to calculate the optimal current settings. To solve this problem, three different approaches were tried:

**Manual tuning** – The theoretical model of the magnetic field environment and coils was calculated and used for determination of optimal currents. Its results are used as an initial estimate for manual tuning of currents in the coils separately. This method is most commonly used during normal day operation, but it is not the most efficient.

**Cs magnetometer feedback** – The magnitude of the magnetic field vector $|\vec{B}|$, generated by each coil ($i$), is measured by caesium magnetometers ($j$), resulting in a set

of $B_{i,j}$. In general, the relation between the coil currents ($I_i$) and the magnitude of the magnetic field at the $j$ sensor position $B_{total,j}$ is described by:

$$B_{total,j} = \left| \vec{B}_{0,j} + \sum_{i=1}^{33} I_i \vec{G}_{x,i,j} \right|, j = 1, \ldots \tag{2.8}$$

where $\vec{B}_{0,j}$ denotes the magnetic field vector originating from outside the system (not correction coils) and from the $B_0$ coil measured by the magnetometer $j$ and $\vec{G}_{i,j} = \frac{1}{I_{test}} \vec{B}_{i,j}$ are the proportionality factors relating coil currents with generated fields. Even the uncorrected field has a large vertical component, while horizontal components are relatively small ($\vec{B}_{0,j,z} \gg \vec{B}_{0,j,x}$ and $\vec{B}_{0,j,z} \gg \vec{B}_{0,j,y}$) and it is possible to simplify Eq. (2.8):

$$B_{total,j} \approx \left| \vec{B}_{0,j,z} + \sum_{i=1}^{33} I_i \vec{G}_{z,i,j} \right|. \tag{2.9}$$

In Eq. (2.9) $\vec{B}_{0,j,z}$ and $\vec{G}_{i,j,z}$ are measured driving the test current $I_{test}$ to individual coils. A perfectly uniform field corresponds to equal values of $B_{total,j}; j = 1, \ldots$. Thus, the optimization procedure has to find such currents $I_i(i = 1, \ldots, 33)$ that equalize $B_{total,j}$ in the best way. This can be achieved using singular value decomposition and regularization methods described in greater detail in Sec. 4.1.

With this method, it is possible to make all the magnetometer readings equal. This does not necessarily mean that the corresponding magnetic field is uniform, since we do not have any information about the direction of the field. However, this method has lead to the magnetic field configuration allowing us to obtain the longest possible free precession time.

**Mapping based** – This approach utilizes the magnetic field maps obtained during a dedicated measurement campaign. This will be described in detail in Chapter 6.10.

### 2.6.3 Shields

The experiment is located at the Paul Scherrer Institute in proximity of other experiments and test sites. All these facilities are sources of a variable magnetic field which can interfere with measurements. Changes in both modulus and gradients increase uncertainty of the measured neutron EDM. To suppress these unwanted influences, two types of magnetic field shielding are used:

**Passive** – built using metal alloys with high magnetic permeability $\mu$. In this experiment we use a 4-layer shield made of Mumetal.

**Active** – this shield consists of coils connected to power supplies and controlled with feedback based on magnetic field measurements by dedicated sensors. Active shields are the main topic of this dissertation. Part II is devoted to the detailed discussion of this topic.

These two shield types have a different range of operation in the frequency domain. Active magnetic field shielding can operate at low frequencies (usually below $100$ Hz, like [36] at $60$ Hz), whereas passive shields behave better at the greater frequency of perturbation [37].

To quantify the performance the so-called Shielding Factor ($SF$) is used. It is defined as:

$$SF = \frac{\|\vec{B}_{\text{without shield}}\|}{\|\vec{B}_{\text{with shield}}\|} \tag{2.10}$$

**Passive shield**

Passive shields are usually built using material with high permeability. This causes static magnetic field lines to concentrate inside the shielding material (see Fig. 2.9). The changing magnetic field generates eddy currents in the conductive shield which compensates the disturbing field.

In nEDM experiment at PSI, 4-layer passive shield made of Mumetal is used. Its dimensions are collected in Tab. 2.2. Measured [39] and simulated [40] performance is shown in Tab. 2.3. The discrepancy between the theoretical and experimental values are related to the fact that there are holes in the Mumetal shield, which were not included in theoretical calculations.
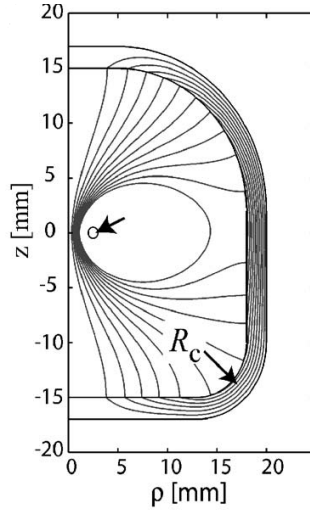
Figure 2.9: Magnetic field lines inside a high permeability ($\mu_r = 1000$) shield. This figure shows the right half of the shield. The field is generated by a current loop of the radius 2.5 centred on the $z$ axis. The circle marked with an arrow is the cross section of the wire. Taken from [38]

Table 2.2: Dimensions of passive magnetic shielding. Each of the layers is made of a cylinder with a radius of $R$, length $l_1$ and two end caps. Length $l_2$ is the total length of shield layer with end caps after assembly. Overlap states how many end caps overlap with the cylinder. $t$ is the thickness of the Mumetal used for both the end caps and cylinder.

| Shield | $R$ [m] | $l_1$ [m] | $l_2$ [m] | Overlap [m] | $t$ [mm] |
|--------|---------|-----------|-----------|-------------|----------|
| 1 | 0.97 | 2.74 | 2.74 | 0.20 | 1.5 |
| 2 | 0.79 | 2.30 | 2.30 | 0.20 | 1.5 |
| 3 | 0.68 | 0.75 | 1.89 | 0.12 | 2.0 |
| 4 | 0.58 | 0.75 | 1.63 | 0.12 | 2.0 |

Table 2.3: The shielding factors for the passive magnetic shield for the nEDM experiment at PSI

| Direction | Measurement at PSI [39] | calculation [40] |
|-----------|-------------------------|------------------|
| Radial horizontal (X) | 13300 | 24023 |
| Longitudinal (Y) | 1600 | 3550 |
| Radial vertical (Z) | 8600 | 24023 |

## 2.7   n2EDM - next generation setup

First measurements of neutron EDM at the Paul Scherrer Institute are done using passive magnetic shielding from the RAL/Sussex/ILL collaboration. Experience gained with this apparatus allows us to design a completely new measurement system suppressing the systematic uncertainties in a much better way. The biggest changes are the sandwiched precession chambers (see Fig. 2.10) instead of the one in the currently used apparatus.

Configuration with two ground electrodes on top and bottom of the sandwich arrangement of two precession chambers and high voltage electrode in the centre makes it possible to run both configurations, parallel and anti-parallel magnetic and electric fields at the same time. Such an arrangement is advantageous since several systematic effects cancel in the first order. In this configuration, the magnetic field in the spectrometer would be measured by three types of atomic magnetometers:

- cohabiting $^{199}$Hg magnetometer

- a pair of $^3$He magnetometers for a direct control of the vertical magnetic field gradients,

- Cs magnetometers,

The Cs magnetometers would be primarily used to monitor the rotating $^3$He magnetization.

The new concept of the spectrometer requires a new design of both a vacuum chamber and a passive magnetic shielding. A sketch of the n2EDM setup is presented in Fig. 2.12. The multilayer cubic Mumetal shield surrounds a cylindrical vacuum vessel, where the spectrometer with two precession chambers and two large-scale $^3$He magnetometers is located. In order to improve the active magnetic field shielding, extensive research and development is being conducted. Results of these investigations are part of this dissertation and described in Part II.

The $B_0$ coil is being designed to be "self-compensating", meaning that the external flux should be as small as possible. This can be done with an additional layer of windings as shown in Fig. 2.11. The reason for suppressing the external flux of the $B_0$ coil is its interaction with the passive shield worsening the $B_0$ field uniformity.
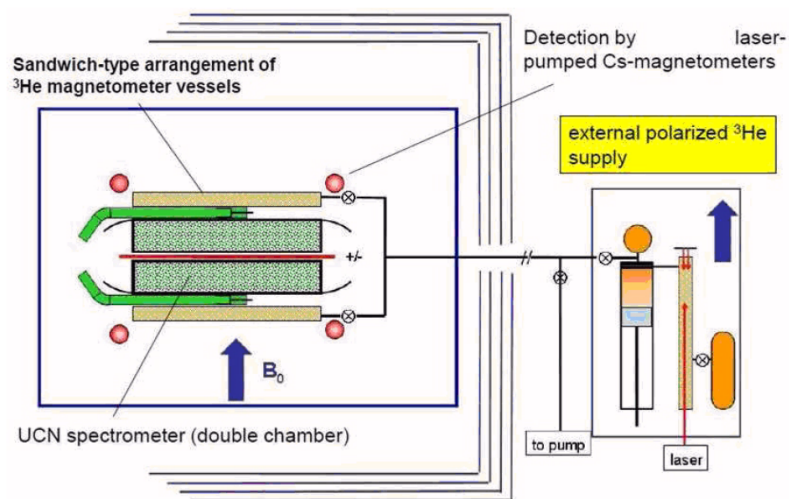
Figure 2.10: Sketch of n2EDM precession chambers with polarized $^3$He supply line
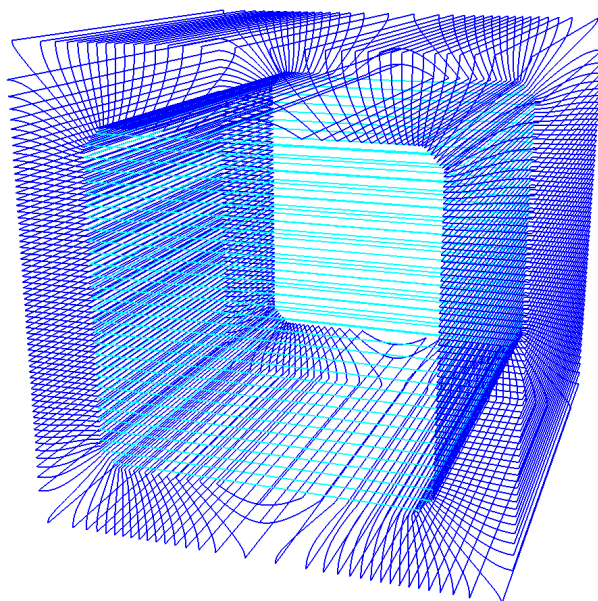


Figure 2.11: 3d image of the DISCO coil - self-compensating coil, which generates uniform magnetic field inside and only small rest magnetic field outside
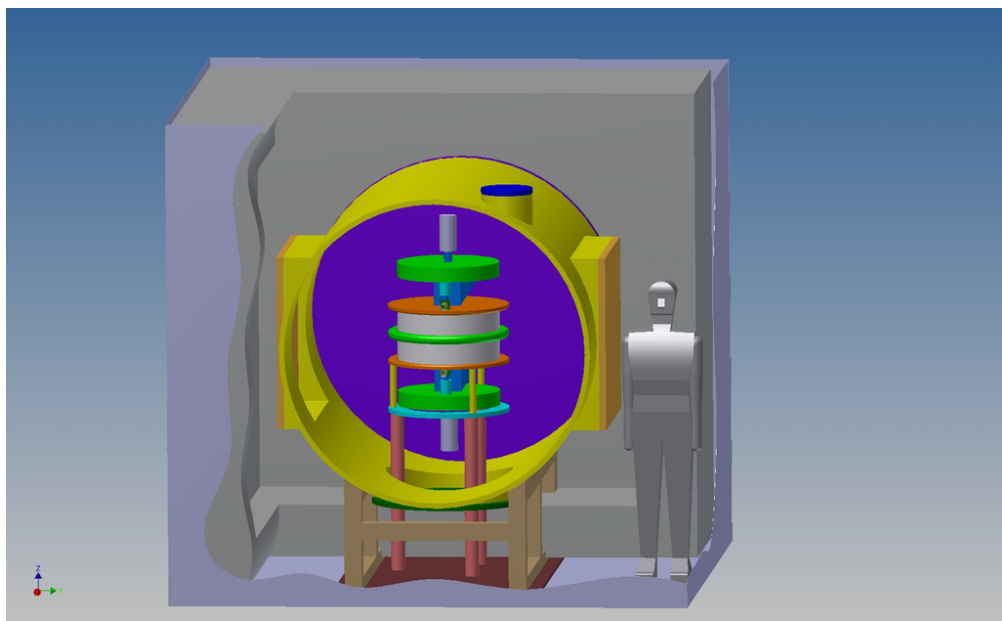
Figure 2.12: Preliminary design of n2EDM experiment apparatus. Visible are two precession chambers – designed to perform the Ramsey method of oscillatory fields with the field parallel and anti-parallel at the same time. They are positioned inside a cylindrical vacuum vessel inside a multi-layer magnetically shielded room.

# Part II

# Active magnetic shielding systems

# Chapter 3

# Introduction

Interesting information about complex physical, biological and environmental systems is communicated to the external world by weak and low-frequency magnetic signals reflecting evolution of the weak magnetization carried by these systems. Similarly, in certain quantum mechanical ensembles such as spin polarized ultra-cold neutrons or atoms, the interesting physical information is superimposed on top of their weak magnetization, which must be strictly controlled in order to observe the desired signal. There are also well established methods to measure magnetic fields in the range starting from 10 nT and down to a few fT. These include fluxgate transducers (see Refs. [41, 42]), quantum-optical magnetometers and SQUIDs (see Ref. [43]), reaching sensitivities as low as a few $fT/\sqrt{Hz}$. The measurement of such weak signals is, however, extremely difficult because external magnetic field disturbances and noise penetrate easily to the object being studied. One traditional way to deal with this problem is based on sophisticated passive shieldings made of high permeability ferromagnetic alloys or superconducting enclosures. Examples of such systems can be found e.g. in Refs. [44–47].

Theoretically, another approach exists to provide a "magnetic vacuum" in a given volume and frequency range. For a charge- and current-free space, in the quasi-static regime, this is guaranteed by solutions of the Laplace equation arising from Maxwell's laws of classical electromagnetism (see for example Ref. [48]). Knowing field vectors at sufficiently numerous points it is possible to judge the field distribution in a given volume with the required accuracy. This, in turn, allows calculating and applying electric currents in a system of correction coils generating (in the same volume) the field distri-

bution with the same magnitude and sign opposite to the measured field. The correction signal must appear with a delay negligible for the frequency range in question.

In practical solutions, especially for a large controlled volume, one is faced with limitations, the most important being the maximal number of independent correction coils included in the feedback loop. Each coil needs a precise and quickly reacting current source with control electronics and dissipating power (heat) which may cause additional problems in a particular application. The main goal of this study is to estimate the performance of an idealized system with as few degrees of freedom as possible. Such a case will be used in the future as a reference for practical solutions, in particular, for the next stage of the nEDM experiment. In this thesis, this system is compared to two already built systems and one only simulated. A total of four different active compensation systems, that will be presented in this work are:

**SFC - surrounding field compensation system** . This system is based on 6 rectangular coils, which are grouped in 3 Helmholtz-like pairs. This configuration is in operation right now as an element of the nEDM experiment at the Paul Scherrer Institute

**Merritt coil system** . There are 12 rectangular coils in this system, which are based on the 4 coil arrangement proposed by Merritt et al. [49]. An operational prototype of this coil set was built for comparison and is described in Chapter 4.2.

**Cellular coils system** . This considered setup consists of a large number of small coils with magnetic field sensors inside each of them. Such a system is the discrete realization of the ferromagnetic or superconducting shielding idea - eddy currents that compensate the magnetic field component perpendicular to the surface are mimicked by the cell coil currents.

**Spherical coils system** . This system is based on the field description using vector spherical harmonics (VSH). It exhibits optimal properties and can be used as a reference in the performance comparison of various systems.

All the calculations were performed with adopted algorithms from the GNU Scientific Library [50]. The calculations for the spherical system are resource-intensive. For instance, for some of the calculations, it consumes as much as 5 GB of memory and

needs over a month of CPU time. In order to speed up the process, the code was implemented onto a GPU system consisting of 3 nVIDIA TESLA C2050 cards (for more information see Ref. [51]).

In order to compare the performance of all coil systems, we assume that the field measurement sensors are located at randomly chosen positions on a cube with 2 m long edges (centred in the coil system centre). The chosen radius for the spherical coils is $r = 2.93$ m and the number of wire turns in each spherical coil is equal to 100. We assume that the finite thickness of the wires has negligible influence on magnetic fields.

As the figure-of-merit for the performance of a field compensation system we define the relative difference $\Delta$ between the perturbation and the field correction generated by the considered system:

$$\Delta = \frac{\left|\vec{B}_{\text{per}} - \vec{B}_{\text{cor}}\right|}{\left|\vec{B}_{\text{per}}\right|}, \tag{3.1}$$

where $\vec{B}_{\text{per}}$ denotes the field generated by an external source and $\vec{B}_{\text{cor}}$ the correction calculated by the compensation system.

The defined in Eq. (3.1) $\Delta$ is a function of $(x, y, z)$ and describes the shielding factor in a given place achieved by the considered compensation system of ideal coils driven by ideal current sources and measured by ideal magnetometers located at fixed positions distributed on the sensor cube.

Since the mostly expected external field disturbances are of dipolar type, we model them with a current loop at a fixed distance and fixed orientation. The resulting field distribution was calculated by the integration of the Biot-Savart's law. This kind of perturbation always generates the magnetic field inside the volume with non-zero magnitude $\left|\vec{B}_{\text{per}}\right| > 0$. This assures that the denominator in Eq. (3.1) is always different than 0.

To equally consider all possible orientations and positions at a given distance, $\Delta$ is averaged over a set of 100 random positions and 100 orientations.

# Chapter 4

# Considered variants of magnetic field compensation systems

In this chapter a description of four active magnetic field shielding systems is presented. These include:

**SFC** - 6-coil rectangular system

**Merritt** - 12-coil rectangular system, based on the setup proposed by Merritt et al. [49]

**Cellular** - System consisting of a large number of small, rectangular coils

**Spherical** - System consisting of 8 or 15 spherical coils, based on vector spherical harmonics

# 4.1 Surrounding Field Compensation system (SFC)
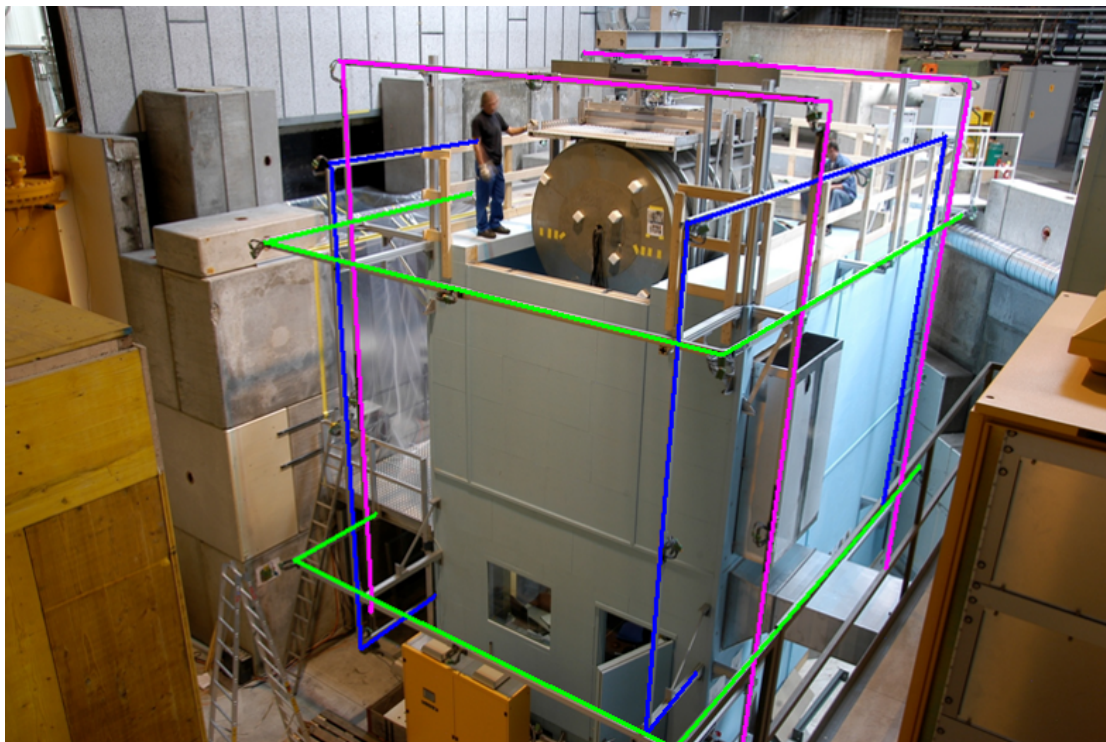


Figure 4.1: Main passive shield and the coils of SFC, marked with colours.

This system is build up of:

- 6 rectangular coils, presented in Figure 4.1. Their dimensions are collected in Tab. 4.1.

- Current sources, power supplies from FuG, type NTN350-35 and NTN700-35. They can provide $350$ W and $700$ W DC power, respectively, and are controlled from PC.

- 10 fluxgate magnetometers, Bartington Mag-03 MCL-70 or MCTP-70, 8 of them mounted in the corners of the aluminium support of the Mumetal shield and two in the centre of the side support structure.

- PC running the compensation algorithm calculating the coil currents stabilized by a PID controller.

Table 4.1: Dimensions of the coils of the rectangular active magnetic field compensation system of the nEDM experiment at PSI

| coil | long side [m] | short side [m] | separation[m] |
|------|---------------|----------------|---------------|
| X- | 7.9 | 6.1 | 4.2 |
| X+ | 7.9 | 6.1 | |
| Y- | 8.2 | 5.9 | 5.1 |
| Y+ | 8.4 | 6.0 | |
| Z- | 8.0 | 5.8 | 4.2 |
| Z+ | 8.0 | 5.8 | |

The coils have independent power supplies providing 6 degrees of freedom of the compensation system. The necessary reaction currents of the external field changes are calculated using the readouts from a number of fluxgate sensors utilizing the fact that the magnetic field strength generated by a coil is proportional to the current driven through it. This leads to a system of linear equations relating the measured field components with the coil currents:

$$
\begin{pmatrix}
B_x^1 \\
B_y^1 \\
B_z^1 \\
\cdots \\
B_z^n
\end{pmatrix}
=
\begin{pmatrix}
G_1^{x1} & G_2^{x1} & G_3^{x1} & \cdots & G_m^{x1} \\
G_1^{y1} & G_2^{y1} & G_3^{y1} & \cdots & G_m^{y1} \\
G_1^{z1} & G_2^{z1} & G_3^{z1} & \cdots & G_m^{z1} \\
\cdots & \cdots & \cdots & \cdots & \cdots \\
G_1^{zn} & G_2^{zn} & G_3^{zn} & \cdots & G_m^{zn}
\end{pmatrix}
\begin{pmatrix}
I_1 \\
I_2 \\
I_3 \\
\cdots \\
I_m
\end{pmatrix}
\tag{4.1}
$$

$$
\vec{B} = \mathbf{G}\vec{I} \tag{4.2}
$$

The $G_k^{ij}$ coefficients are determined by recording the fluxgate magnetometer measurement values while changing the current in one coil at a time. The minimum number of 3-dimensional fluxgate sensors necessary to uniquely establish the coil currents depends on the number of coils in the system. Only two sensors are required for that purpose, in the case of this rectangular coil system. However, such a system would compensate the field changes only in two points (the location of fluxgate sensors) ignoring the field changes in other parts of the controlled volume. Moreover, the uncertainties of the measured fields propagate to the calculated correction currents. In order to reduce these drawbacks the system utilizes more fluxgate sensors leading to an overdetermined set of equations.

In general, such a set of linear equations does not have solutions, but it is possible to solve the least-square problem instead:

$$I_{leastsquare} = \min_{\vec{I}} \left\| \mathbf{G}\vec{I} - \vec{B} \right\| = \tilde{\mathbf{G}}^{-1}\vec{B}, \tag{4.3}$$

where $\|\cdot\|$ denotes the euclidean norm. The pseudoinverse matrix $\tilde{\mathbf{G}}^{-1}$ is calculated using the Singular Value Decomposition method [52].

In this method the $\mathbf{G}$ matrix of size $m \times n$ is decomposed into a product of three matrices:

$$\mathbf{G} = \mathbf{U}\mathbf{\Sigma}\mathbf{V}^{\dagger}, \tag{4.4}$$

where: $\mathbf{U}$ and $\mathbf{V}$ are unitary matrices ($\mathbf{U}^{-1} = \mathbf{U}^{\dagger}$) of sizes $m \times m$ and $n \times n$, respectively, $^{\dagger}$ denotes conjugate transpose and $\Sigma$ is a diagonal $m \times n$ matrix with diagonal values $\Sigma_i$.

Properties of such matrices make the pseudoinverse matrix easy to calculate:

$$\tilde{\mathbf{G}}^{-1} = \mathbf{V}\mathbf{\Sigma}^{-1}\mathbf{U}^{\dagger}, \tag{4.5}$$

with $\mathbf{\Sigma}^{-1} = \mathrm{diag}\,(1/\Sigma_i)$ - diagonal matrix with values $1/\Sigma_i$.

Elements of matrix $\mathbf{G}$ include noise, no matter if it is induced by measurement or calculation. Even a small change, introduced by finite numerical precision of the computer floating point algebra, would result in significant differences of current solutions. To limit this problem, the so called Tikhonov regularization (see Ref. [53]) is introduced in pseudoinverse calculation. This approach solves not the least-square problem of Eq. (4.3), but the more general one:

$$I_{tikhonov} = \min_{\vec{I}} \left( \left\| \mathbf{G}\vec{I} - \vec{B} \right\|^2 + \left\| \mathbf{\Gamma}\vec{I} \right\|^2 \right) = \breve{\mathbf{G}}^{-1}\vec{B}, \tag{4.6}$$

where $\mathbf{\Gamma}$ is an additional matrix, usually chosen as a scaled identity matrix $\mathbf{\Gamma} = \alpha\mathbf{1}_{n \times n}$.

The solution to such a problem is given by:

$$\breve{\mathbf{G}}^{-1} = \mathbf{V}\breve{\mathbf{\Sigma}}^{-1}\mathbf{U}^{\dagger}, \tag{4.7}$$

where $\breve{\Sigma}^{-1}$ is a diagonal matrix with elements given by:

$$\breve{\boldsymbol{\Sigma}}^{-1} = \text{diag}\left(\frac{\Sigma_i}{\left(\Sigma_i\right)^2 + \alpha^2}\right), \tag{4.8}$$

which, in comparison to regular pseudoinverse, results in decreasing value of the inverse of the smallest singular elements $\Sigma_i$. The parameter $\alpha$ needs to be optimized for the specific case. The most common way of finding the optimal $\alpha$, is the use of the so-called L-curve (see Ref. [54]). It is a log-log plot of the residual $\left\|\mathbf{G}\vec{I} - \vec{B}\right\|$ as a function of the norm $\|x\|$ for different values of the regularization parameter $\alpha$. The name originates from the shape of this curve, which is similar to the L letter. The point of the greatest curvature estimates the optimal $\alpha$ value.

### 4.1.1 Residual distributions of compensation
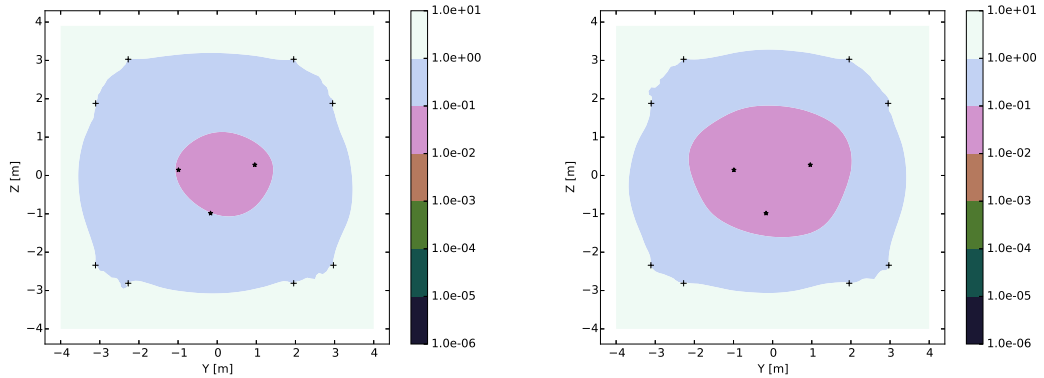


Figure 4.2: Maps of the simulated average $\Delta$ for the rectangular magnetic field compensation system for disturbance sources located randomly 20 m away from the centre of system – left panel and 200 m – right panel. The map plane is at $x = 0.01$ m. The coil positions are marked with black crosses and positions of three (out of 10) feedback sensors are marked with black stars.

The simulations were performed to compare SFC system to other considered systems. For the calculations the magnetic field values at 10 fixed positions were used. These positions are common to all systems. The SFC system of coils is the simplest one of all considered in this thesis. The distribution of $\Delta$ for sources located closely and further away are presented in Fig. 4.2. The smallest values, meaning better compensa-

tion, are in a close neighbourhood of sensors. Even there, $\Delta$ is not smaller than $10^{-2}$. With increasing distance to the source of magnetic field disturbance, the volume with lower $\Delta$ is increasing which will be described, in detail, in Chapter 5.

## 4.1.2 Measurement results

The ability for compensation of the changing field is quantified by Allan standard deviation and dynamic shielding factor. They are defined in the following chapter.

**The Allan standard deviation and Dynamic Shielding Factor**

Consider a series of measurements of the changing magnetic field $\vec{B}_i$, performed in the time sequence. Each $\vec{B}_i(\tau)$ represents a measurement averaged over an $i$-th integration period of length $\tau$. In such a measurement series, one can define the Allan standard deviation $\sigma_y(B, \tau)$:

$$\sigma_y(B, \tau) = \sqrt{\frac{1}{2(N-1)} \sum_{l=1}^{N-1} \left( \bar{B}_{l+1}(\tau) - \bar{B}_l(\tau) \right)^2}, \qquad (4.9)$$

where: $N$ - number of $\tau$ intervals in the whole measurement ($N = T/\tau$, where $T$ - total measurement interval) , $\bar{B}_l(\tau)$ is the average over an $l$-th interval.

Allan standard deviation will be used in the definition of the dynamic shielding factor (see below).

During operation of an active magnetic shielding system, information about the magnetic field vectors at the position of sensors and current is supplied to the coils. With these information, it is possible to reconstruct what the magnetic field would look like, if the compensation system was not working (see section 4.1):

$$B_{(j)\text{not compensated}} = B_{(j)\text{compensated}} - \sum_{i=1}^{12} \mathbf{G}_{j,i} I_i, \qquad (4.10)$$

where $I_i$ is the current driven into $i$-th coil, $B_{(j)\text{compensated}}$ is the magnetic field measured by $j$-th sensor (compensated field). The dynamic shielding factor ($DSF$) is defined as a ratio of the Allan standard deviation of uncompensated and compensated fields and

thus, is a function of the integration time:

$$DSF_j(\tau) = \frac{\sigma_y\left(B_{(j)\text{not compensated}}, \tau\right)}{\sigma_y\left(B_{(j)\text{compensated}}, \tau\right)} \qquad (4.11)$$

**Measurement results**

Operation of this system is described in Ref. [55].

Experimental investigation revealed that regularization is crucial to operation of this system. Without it, the compensation system introduces additional noise instead of preventing it. Results from the most optimal configuration (a regularized pseudo-inverse matrix used for calculation of currents from 24 magnetic field sensors) are presented in Fig. 4.3. The dynamic shielding factor for $\tau = 100$ s is spread out between $2$ and $12$.
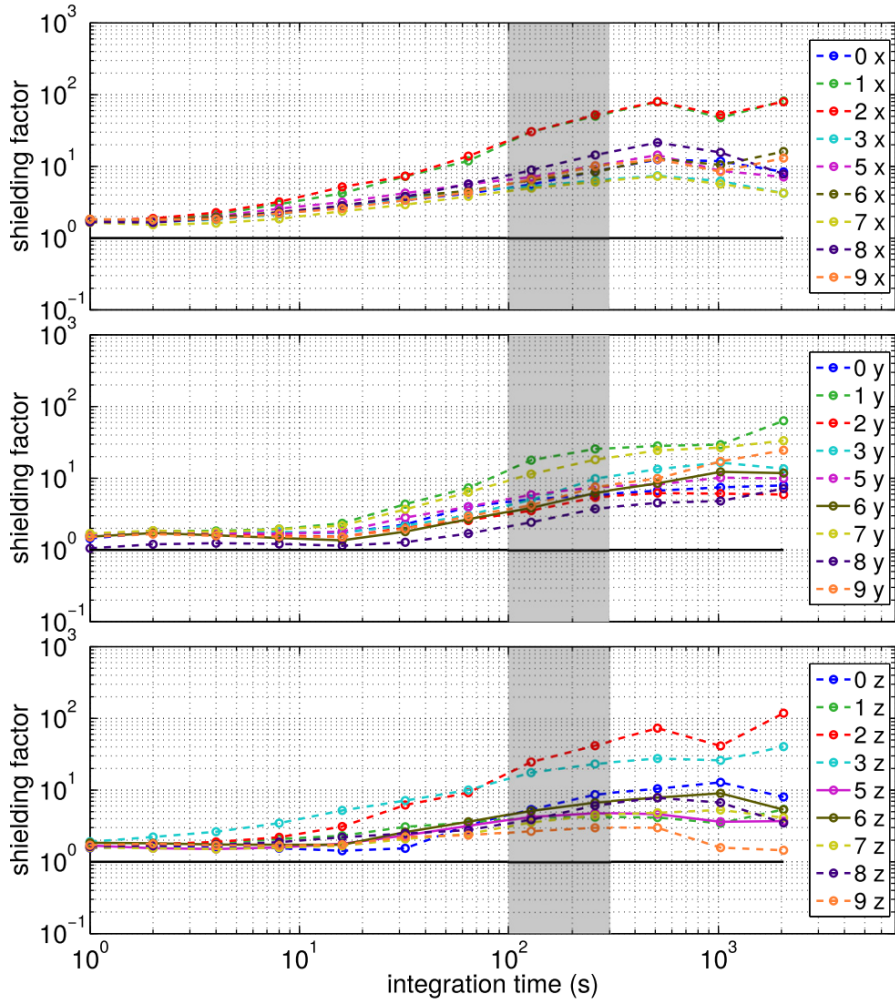
Figure 4.3: Shielding factors from a measurement using the SFC system with 24 sensor feedback, including a regularized matrix. The plot shows $DSF_j$ for all SFC sensors as a function of integration time, sorted by their orientation: x-sensors in the upper, y-sensors in the middle, and z-sensors in the lower graph, respectively. Feedback sensors are plotted with dashed lines and monitoring sensors are plotted with solid lines. The solid black line is an emphasized grid line at $DSF = 1$; shielding factors lower than 1, indicate noise increase by dynamic SFC implementation. The grey area depicts the region of interest for the nEDM experiment.

# 4.2 Merritt system

The simplest extension to the 6-coil system is by adding more degrees of freedom with additional coils. The main goal for this extension was to increase the volume, inside which, it is possible to compensate external perturbation effectively. Based on the analysis from Ref. [56], the four parallel coil system proposed by Merritt, Purcell and Stroink in Ref. [49] would be responsible for the compensation of one Cartesian field component. In order to compensate independently in 3D, we consider installing three such sets along all three spatial directions. This results in 12 square coils in total.

According to Ref. [56], 4 square coils of edge length $d$ aligned parallelly (see Fig. 4.4a at $-0.5005d$, $-0.1281d$, $0.1281d$ and $0.5005d$ with a current flowing through an inner coil pair being $11/26$ of the current of outside coils, generate the most uniform field, seen in Fig.4.4b.



(a) Geometry of the system

(b) Uniformity of the magnetic field shown in the plane sectioning the coils through their geometrical centre
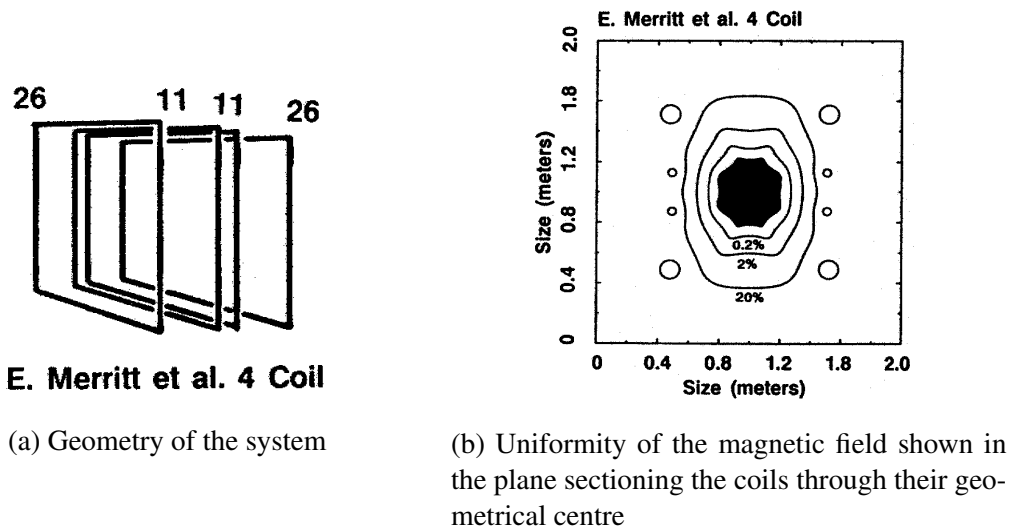
Figure 4.4: Merritt et al. 4-coil system. Figure taken from [56]

.

## 4.2.1 Geometry optimization

Due to mechanical limitations, the geometry of the 3D system has to be adjusted. The outer pair of coils have to be located closer to the centre of the system than in the original

setup. This change makes it necessary to find a new optimal position and number of wires for two internal coils.

Fixing the distance between the outer coils to be $0.96d$, where $d$ is length of the edge of the square coil, there are two parameters, which have to be optimized:

- Position of two inner coils

- Winding ratio $k = I_{inner}/I_{outer}$

The figure of merit, $u$, is defined as the frequency of the relative (to the centre) field remnant below a given threshold.

$$u = \text{number of points with } \frac{|B_{centre} - B_{point}|}{|B_{centre}|} < u_{threshold} \qquad (4.12)$$

The parameter space was scanned with $10,000$ random points uniformly distributed in the volume enclosed by coils. The $u_{threshold}$ was set to $2 \cdot 10^{-2}$.

The results of the parameter scan are presented in Fig. 4.5. The optimal setup is the distance between coils equal to $0.25 \cdot d$ and $I_{inner} = 0.4375 I_{outer}$. Such a setup generates the remnant magnetic field presented in Fig. 4.6.
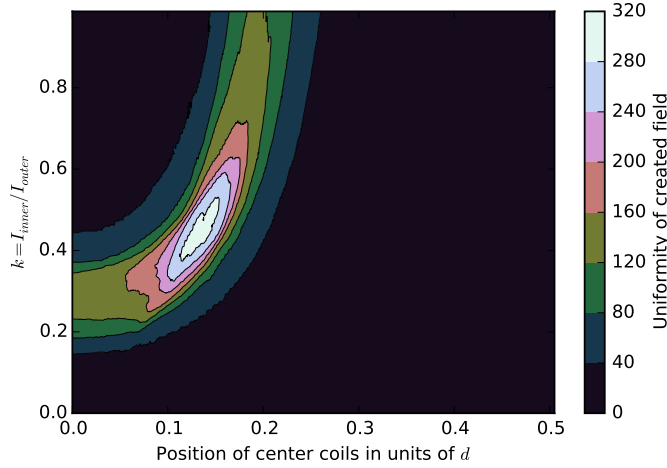


Figure 4.5: Results of optimization of number of windings and position of two centre coils in Merritt-like configuration. Optimal configuration is seen in coils positioned at $\pm 0.125 \cdot d$ with $k = 0.4375$.

(a) for $x = 0$



(b) for $x = 1$



(c) for $x = 1.8$
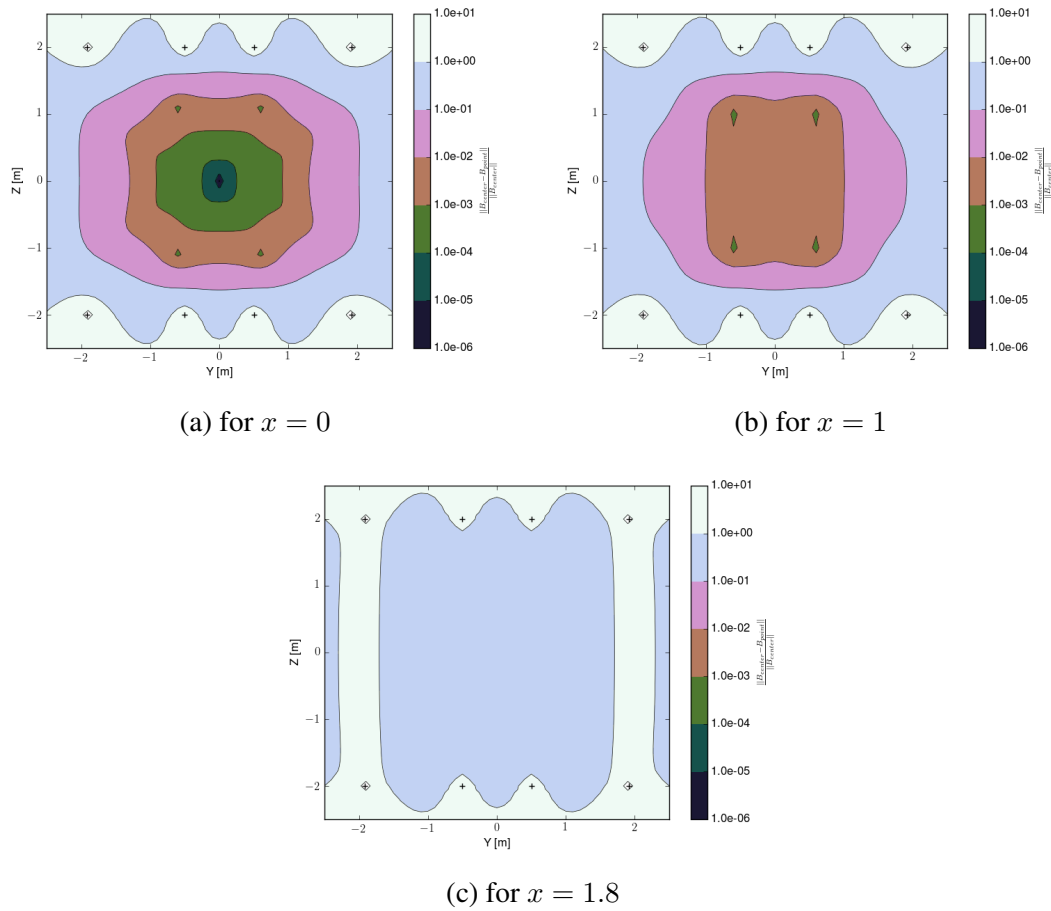
Figure 4.6: Simulated distribution of $\frac{|B_{centre} - B_{point}|}{|B_{centre}|}$ for calculated, optimized 4 square coil configuration with edge length of coil $d = 4$ m.

### 4.2.2 Compensation performance

Considered system maps of the shielding factor $\Delta$ (see Eq. (3.1)) for disturbances located at $20$ m and $200$ m from the system are presented in Figures 4.7a and 4.7b, respectively. Comparing to the similar maps for the SFC system (see Fig. 4.43), one concludes that, at close distances of the perturbation source, the performance of the Merritt system is similar. When the source is further away, the 12 coil system is compensating the outside disturbance better than the simpler one achieving $\Delta \leq 10^{-2}$.



(a) Sources 20 m away           (b) Sources 200 m away
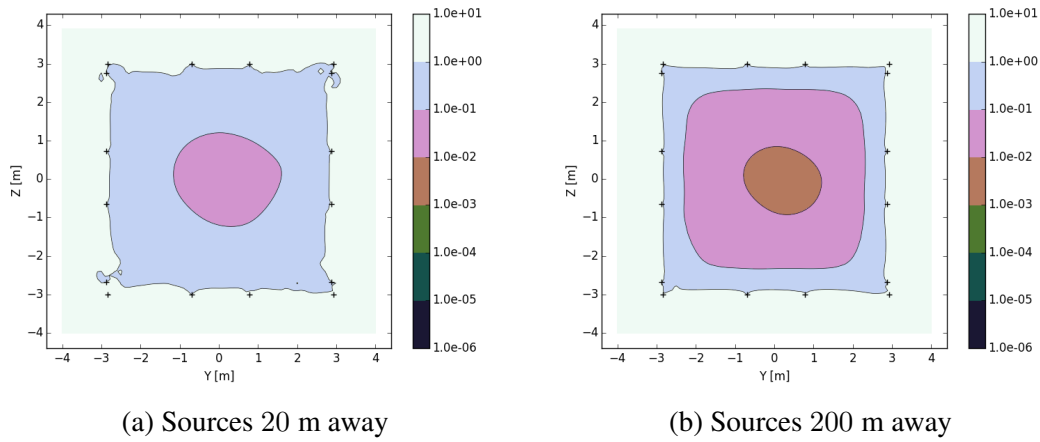
Figure 4.7: Maps of simulated average $\Delta$ for 12 Merritt coil magnetic field compensation system for disturbance sources located randomly 20 m and 200 m away from the centre of system. The map plane is at $x = 0.01$ m. The coil positions are marked with black crosses.

### 4.2.3 Prototype of Merritt system

The mechanical construction of coils is presented in Fig. 4.8 where a 5-wire cable is wound around the aluminium profiles fixed to a frame made from the same material. The inner volume is a cube with $128$-cm-long edges. The positions of the coils are listed in Tab. 4.2. In our system, we use 10 Steffan Mayer FLC3-70 fluxgate magnetometers Their positions and orientations are gathered in Tab. 4.3. Nine of those sensors are positioned near the coils on the aluminium frame and provide input to the feedback loop. The tenth sensor was used for monitoring and is located in the centre of the system.
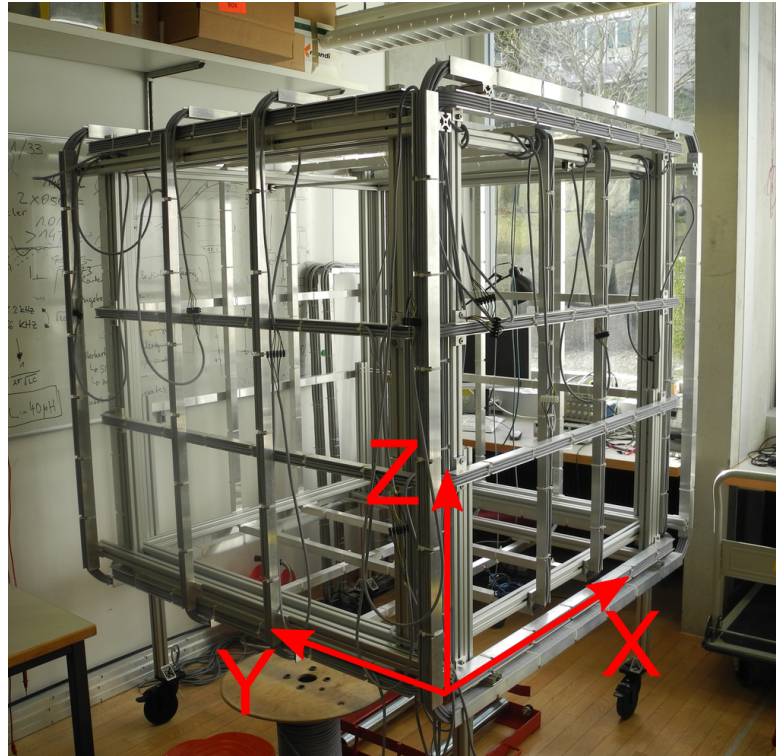
Figure 4.8: 12 coils of active magnetic field compensation system.

Table 4.2: Dimensions of prototype 12-coil Merritt setup

| Coil | Position along axis [mm] | long edge [mm] | short edge [mm] |
|------|--------------------------|----------------|-----------------|
| X1 | 0 | 1299 | 1249 |
| X4 | 1280 | | |
| X2 | 480 | 1289 | 1259 |
| X3 | 800 | | |
| Y1 | 0 | 1450 | 1390 |
| Y4 | 1440 | | |
| Y2 | 540 | 1460 | 1392 |
| Y3 | 910 | | |
| Z1 | 0 | 1445 | 1445 |
| Z4 | 510 | | |
| Z2 | 860 | 1450 | 1435 |
| Z3 | 1360 | | |

Table 4.3: Orientation and positions of fluxgate magnetometers. Sensor 0 (marked with *) is not used for feedback.

| | Field in | | | Position | | |
|---|---|---|---|---|---|---|
| | X | Y | Z | X | Y | Z |
| Number | direction measured by | | | [mm] | | |
| 1 | y | z | x | 1350 | 270 | 191 |
| 2 | -z | y | x | 1140 | 1445 | 875 |
| 3 | -y | x | z | 200 | 470 | 490 |
| 4 | y | -z | -x | 310 | 1220 | 275 |
| 5 | x | -z | y | 1057 | 1300 | 1240 |
| 6 | -y | -x | -z | 120 | 1013 | 1020 |
| 7 | x | z | -y | 630 | 230 | 1230 |
| 8 | -x | -z | -y | 700 | 1015 | 0 |
| 9 | -z | y | x | 1280 | 1300 | 680 |
| 0* | $\sqrt{\frac{1}{2}}z - \sqrt{\frac{1}{2}}y$ | $\sqrt{\frac{1}{2}}z + \sqrt{\frac{1}{2}}y$ | -x | Centre of system | | |

Custom-built RC filters were used to filter high frequency noise from magnetometers. Their scheme is shown in Fig. 4.9. The frequency response of this circuit is plotted in Fig. 4.10.
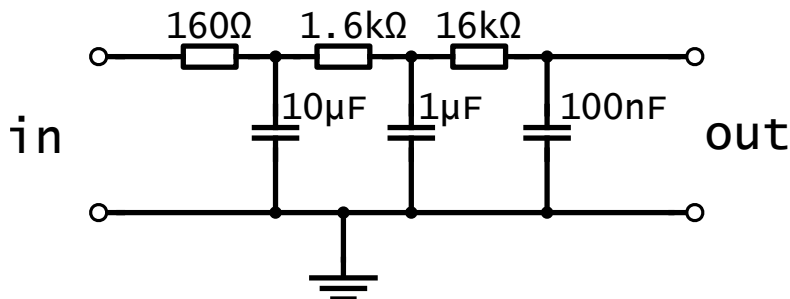


Figure 4.9: Scheme of RC filter

After filtering, analogue signals were read out by two National Instruments PXI-6284 cards. They are multiplexing 18-Bit Analogue Input digitizing cards.

Multiplexing with connected RC filters caused the so called "ghosting" [57] which is experienced when the acquired value in one channel depends on the value from the previous one. This phenomenon is illustrated with Fig. 4.11. Two readout modes are presented for the same sensor (located at the same position). In the first one, marked with +, the presented sensor was the only one read out. In this case, there is no ap-
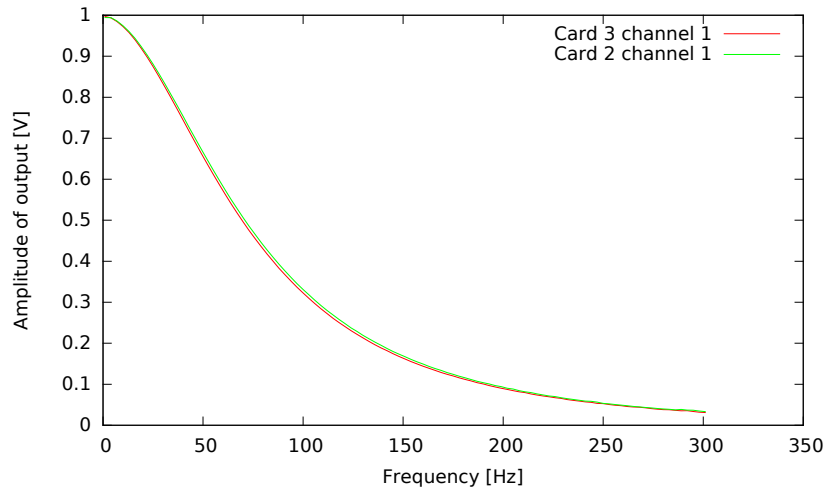
Figure 4.10: Frequency characteristics measured for two input filters for the 12-coil active compensation system

parent dependence between the acquired value and the sampling rate. In the second mode, marked with $\times$ symbols, measurements were done in the multi-channel mode. The channel preceding that read out was disconnected. In this mode, there is a clear dependence between measured values and the sampling rate, which for high sampling rates tends to be linear.

This problem is caused by an internal capacitance of the ADC card. For high impedance input, the charging time may be longer than the time window allocated to one channel at a given sampling frequency. The digitized voltage is not saturated to that of the input. Because of the shortage of resources, we have decided to minimize this problem by lowering the sampling rate.

A dedicated setup shown in Fig. 4.12 was built to measure the ghosting effect. One fluxgate (generator) was positioned between Helmholtz coils. They were supplied by a sinusoidal voltage source. The second fluxgate (monitor) was positioned in another room, about $5$ m away from the rest of the setup. It was enclosed in a multi-layer magnetic shield built from Metglas Magnetic Alloy 2705M (Cobalt-based) [58] to suppress influence from Helmholtz coils. The fluxgates were positioned so that the Z component of the generator fluxgate was oriented along the axis of Helmholtz coils (to generate the biggest field) and the X component of the monitor sensor was oriented perpendicularly to that direction.
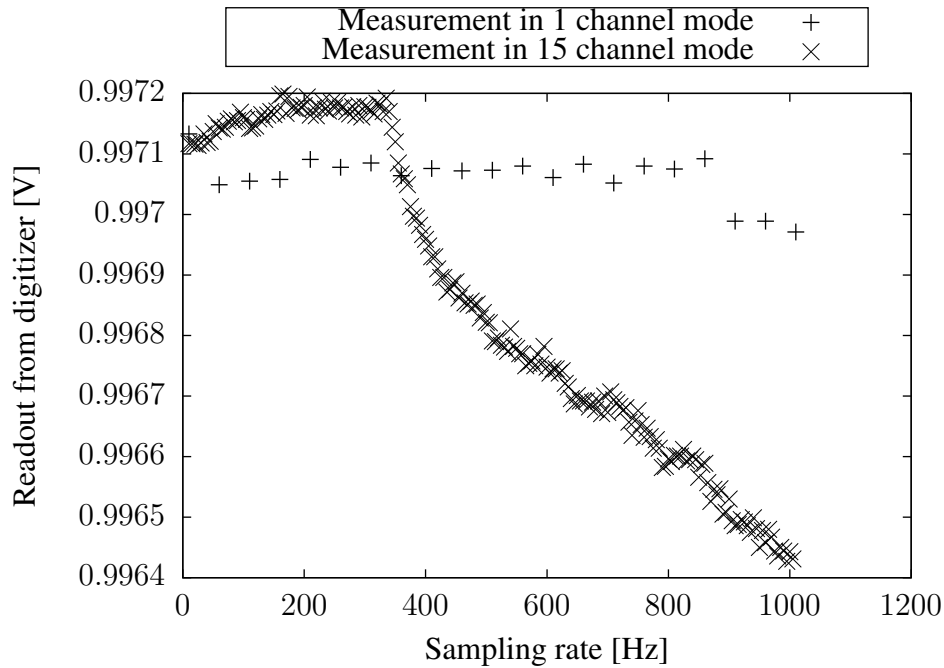
Figure 4.11: Readout of the field from fluxgate in two configurations - as one of 15 read channels in multiplexed mode ($\times$) and as the only read channel ($+$).

The size of the ghosting effect was described by the crosstalk parameter $T$ defined as:

$$T = \frac{B_{1\text{channel}} - B_{15\text{channel}}}{B_{\text{prev.channel}}}, \tag{4.13}$$

where $B_{1\text{channel}}$ is the field read out by the monitor sensor in one channel mode, $B_{15\text{channels}}$ and $B_{\text{prev.channel}}$ are the measurements from the monitor and generator sensor, respectively, obtained in the multiplexed mode of the digitizer card. To correct for linear drifts of the field, $B_{1\text{channel}}$ is the average of two values, measured before and after the multiplexed mode measurement and is plotted in Fig. 4.13 as a function of sampling rate. This plot was used for optimizing the sampling rate – the sampling frequency of 100 Hz was used, where the ghosting effect is still small.
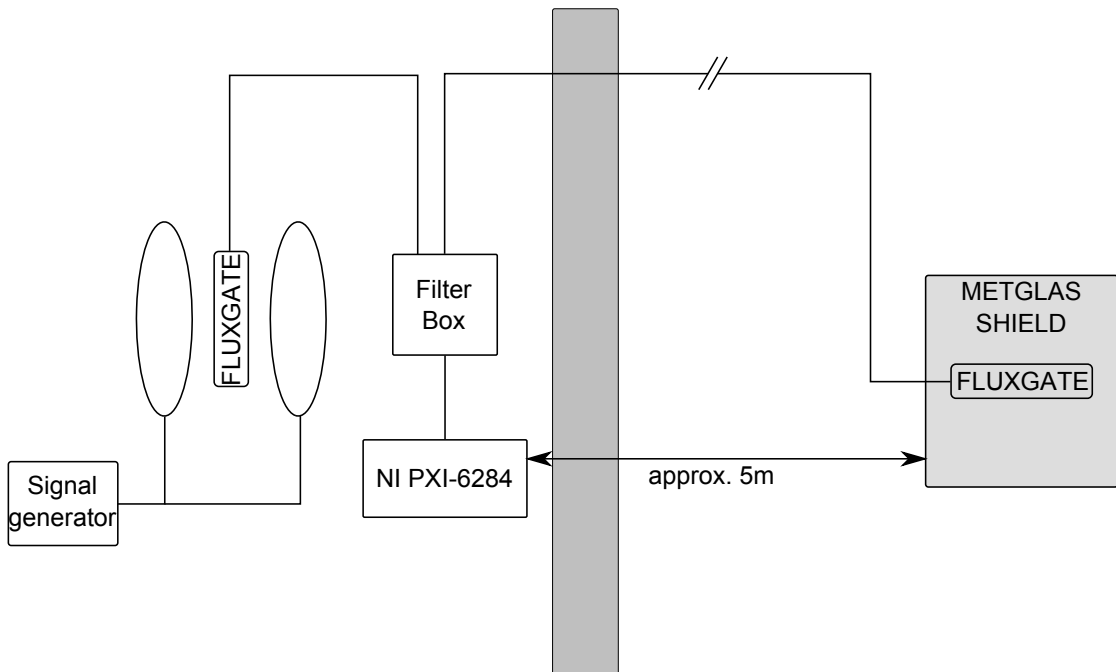
Figure 4.12: Setup for measurement of crosstalk between channels.
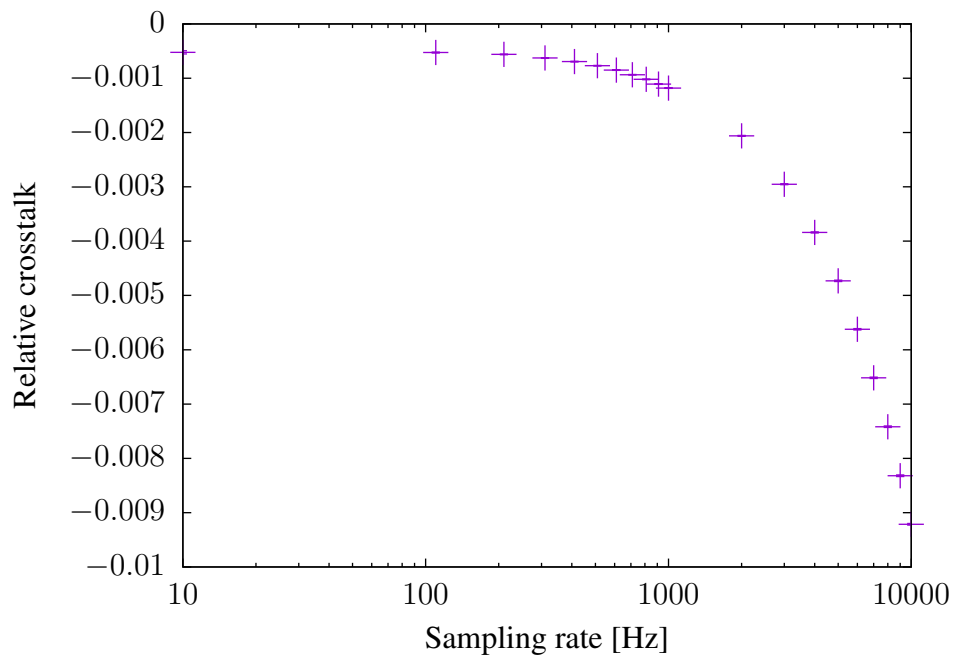


Figure 4.13: Relative crosstalk as a function of sampling rate for readout of magnetic field.
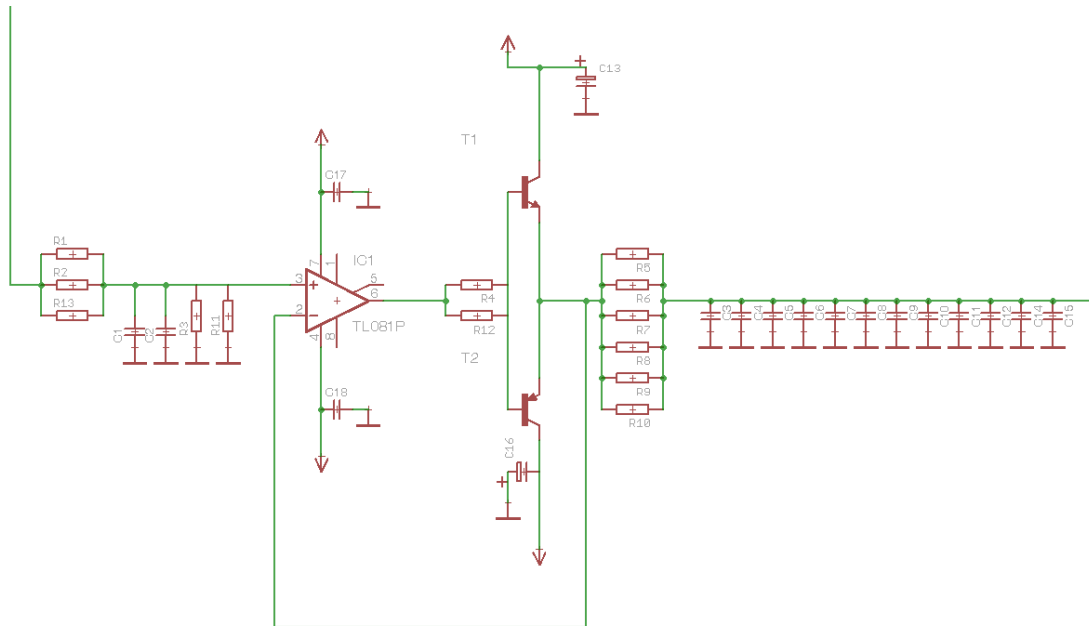
Figure 4.14: Schematic of the current sources used in Modified Merritt setup

**Feedback - calculation of reaction currents**

The coil currents were supplied by the custom built power supply [59] controlled by DC voltage delivered by a DAC card (National Instruments PCI-6733). The electrical schematic of the power supplies is presented in Fig. 4.14.

**Matrix determination**   Before application of control algorithm it is necessary to find the relation between the measured magnetic field and voltage used to control current sources (response matrix $\mathbf{G}$ from Eq. (4.2)). To do that, designated calibration measurement was performed where the control voltage (within range of current sources) was applied to coils. The field was measured with all 10 three-dimensional sensors. For each of the relations between the field and the input voltage, a linear function was fitted which slope defines one element of $\mathbf{G}$ matrix.

**Matrix inversion and finding optimal parameters**   Response matrix $\mathbf{G}$, obtained from the calibration procedure described above, needs to be (pseudo)-inverted (see Sec. 4.1) before using it in the feedback algorithm.

In the first step, the l-curve (see Sec. 4.1) was drawn (Fig. 4.15) to find the optimal regularization constant $\alpha$. In this log-log plot, abscissas are the norms of the residuals of currents (solutions of equation $\vec{B} = \mathbf{G}\vec{I}$). Ordinates are the norms of the solutions. In this plot, the point of the highest curvature is connected with the optimal regularization parameter. Having this theoretically optimal regularization parameter $\alpha = 0.06$, three different values were tested empirically:

1. $\alpha = 0$ - no regularization

2. $\alpha = 0.06$ - theoretically optimal regularization

3. $\alpha = 0.1$ - theoretically over-regularization.

All three $\mathbf{G}^{-1}$ matrices were tested in the system working for 24 hours to include both noisy time during day and quiet conditions in the night. The results are non-conclusive, although slightly better performance is achieved using the theoretically optimal regularization at $\alpha = 0.06$.
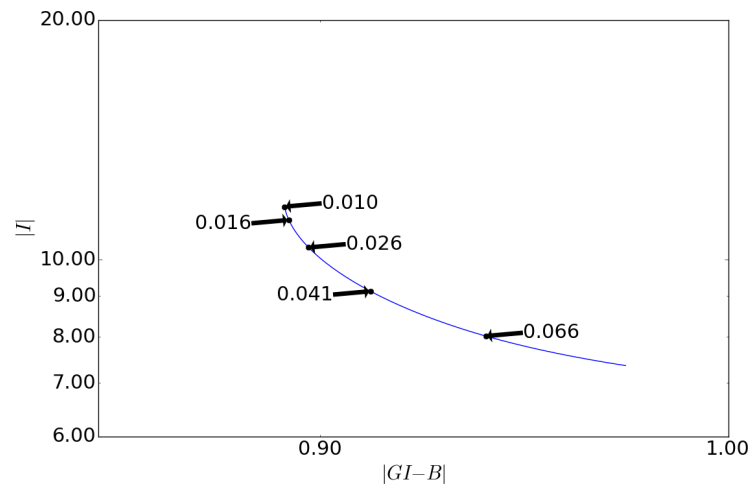


Figure 4.15: L-curve for the regularized pseudo-inverse of the $\mathbf{G}$ response matrix. Labels mark the value of regularization constant $\alpha$ for some of the points.

**Feedback algorithm**  The power supplies were not able to drive enough current to compensate the Earth magnetic field, so it was decided to cancel only changes of the

magnetic field around $\vec{B}_{goal}$. $\vec{B}_{goal}$ was chosen to be the first measured field vector in the run.
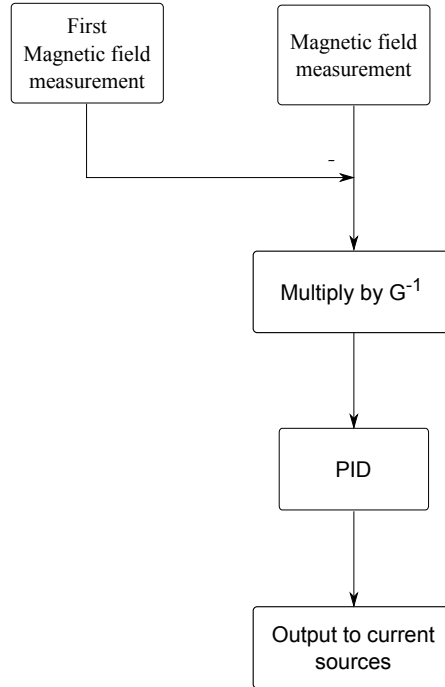


Figure 4.16: Flow diagram of the control algorithm

The feedback algorithm was implemented using the National Instruments LabView 2008 programming platform. After initialization, the system works in a loop. Each loop consists of the following steps (see the flow diagram in Fig. 4.16):

**Measurement of the field** The three consecutive readout values of each of field components are averaged and used for further calculations.

**Multiplication of the measurement field by the inverse matrix** To calculate the change in magnetic field that needs to be compensated, the $\vec{B}_{goal}$ magnetic field is subtracted from all measured and averaged 27 magnetic field components. The resulting field disturbance (from $\vec{B}_{goal}$) vector is multiplied by the inverse of response matrix (see section 4.1), which established a set of currents required to compensate this departure:

$$\tilde{\vec{I}}_n = \mathbf{G}^{-1}(\vec{B}_{meas,n} - \vec{B}_{goal}), \tag{4.14}$$

where $n$ denotes the loop number.

**PID** Calculated current information is used as an input to a PID controller, which calculates the final set of currents to be driven to coils.

$$\vec{I}_{n+1} = 0.8 \underbrace{\tilde{\vec{I}}_n}_{\text{P part}} + 0.9 \underbrace{\sum_{i=0}^{n} \hat{\vec{I}}_i}_{\text{I part}} \tag{4.15}$$

The differentiation part of the PID controller puts the compensating system into an unstable state, so it was decided to use only the proportional and integrating part of this solution.

**Setting of currents** Currents calculated by the PID controller are passed to outputs of the DAC card controlling the current sources.

**Waiting period** Before starting a new loop iteration, we waited for 50 ms, corresponding to the maximal setting time for the current in this system. This time was established experimentally by setting the currents within the allowed range and observing how long it takes to stabilize the current.

The new currents were calculated with the frequency of $\approx 10$ Hz, which is mostly a result of $50$ ms waiting time and delays caused by computer calculations.

### Background magnetic field

The prototype 12-coil compensation system was installed in the basement of the Institute for Particle Physics, ETH Zürich. Tests were performed in the neighbourhood of other experiments and installations, which generate contributions to the ambient magnetic field. Evolution of this field was measured and the results are presented in Fig. 4.17. During the day, the biggest field noise was observed in vertical direction. This component of ambient field decreases significantly during the night. The frequency of $16\frac{2}{3}$ Hz is clearly present, which may be related to the train system in Switzerland supplied by the alternating current with this frequency.

### Measurement results

The most significant results are the values measured by the sensor 0 (see Tab. 4.3), which was positioned in the centre of the system and not used in feedback. This is the

sensor checking what is the real performance in the centre of the system.

An example of magnetic field evolution measured by this sensor is presented in Fig. 4.18. The compensated magnetic field is the one measured directly by the fluxgate sensor while the not compensated field is calculated back using information about currents in coils. Even without calculation of the Allan Deviation, it is visible that noise is significantly suppressed, especially the vertical direction. The suppression of long-term drifts is clearly visible in all directions. It is not possible to compensate sudden magnetic field jumps shorter than 200 ms (twice the feedback loop period), since the system needs this time to react.

The Allan standard deviation plots are presented in Fig. 4.19. Dividing the respective Allan deviation of not compensated and compensated magnetic fields gives the Dynamic Shielding Factor, as shown in Fig. 4.20. Comparing three considered values of the regularization parameter $\alpha$, the differences of operation are not significant - all three possibilities give maximal $DSF$ of 10 for 10 s integration time for the vertical component. Other two components are compensated with $DSF$ of order of $2 \div 3$. The SFC system, which is currently operating in the nEDM experiment at PSI, usually achieves better performance (see Chapter 4.1.2), which is probably due to the less noisy environment on the site of the measurement of the SFC at the Paul Scherrer Institute.
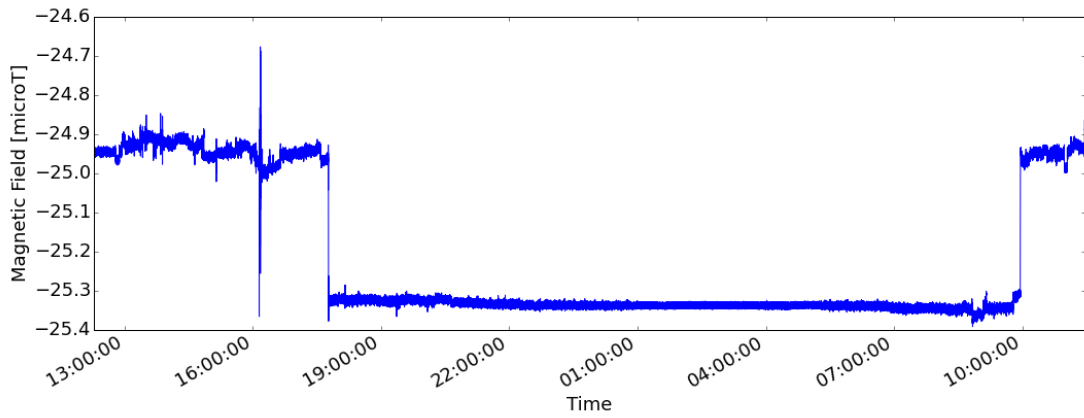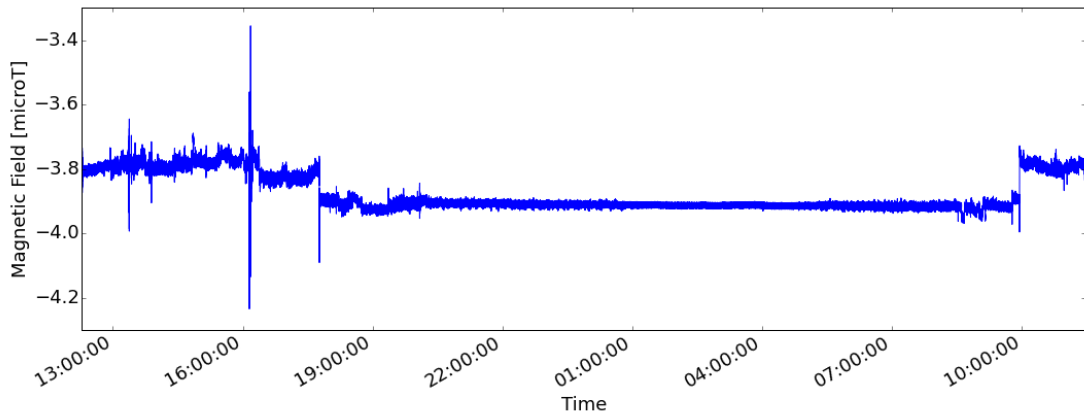
(a) X coordinate



(b) Y coordinate
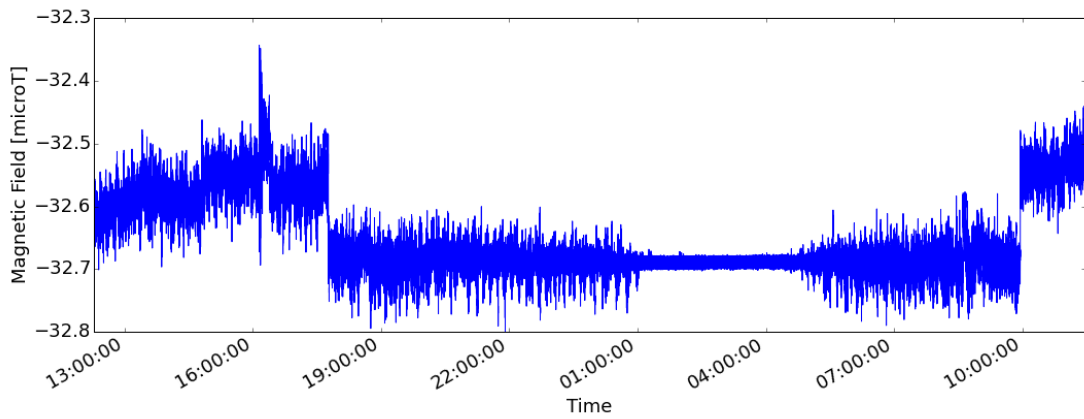


(c) Z coordinate

Figure 4.17: Background magnetic field, registered on site of operation of 12 coil compensation system.
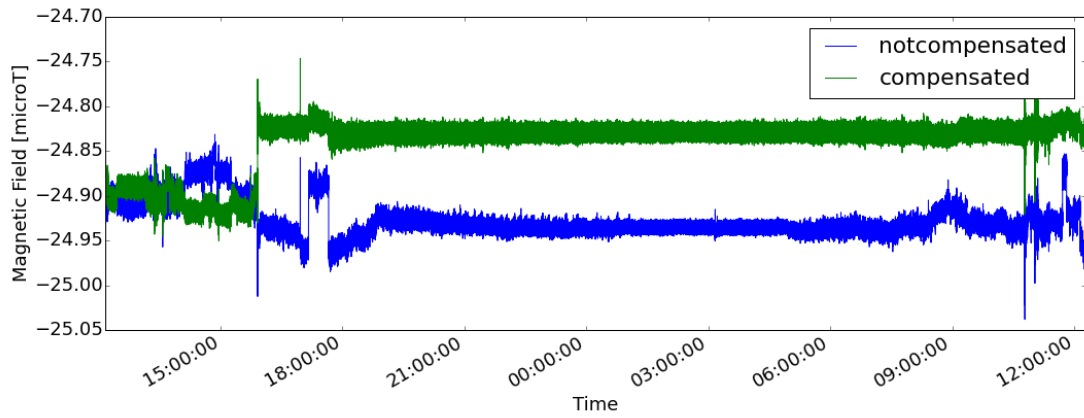
(a) X direction
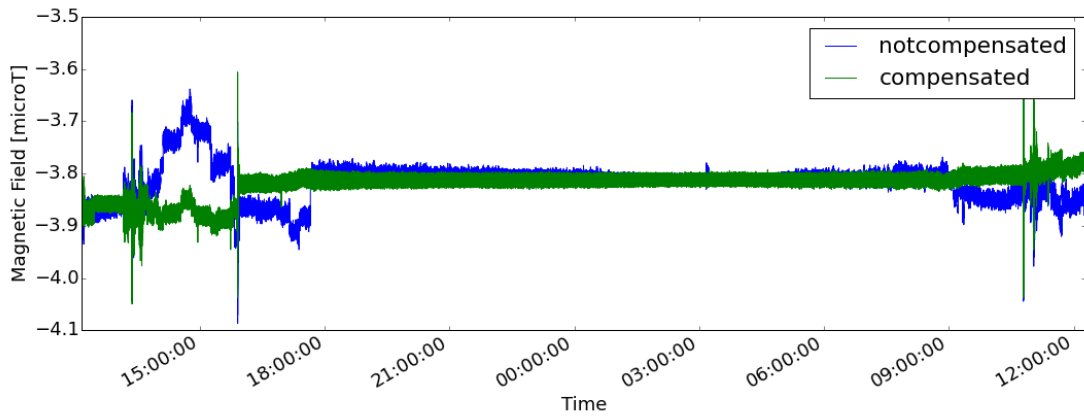


(b) Y direction
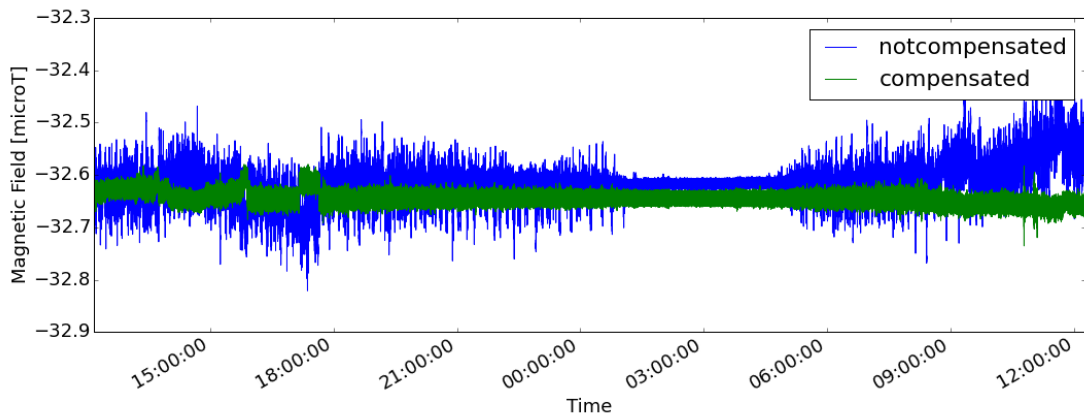


(c) Z direction

Figure 4.18: Magnetic field measured (compensated) and calculated using information about the currents in coils (non-compensated) for the 12-coil system
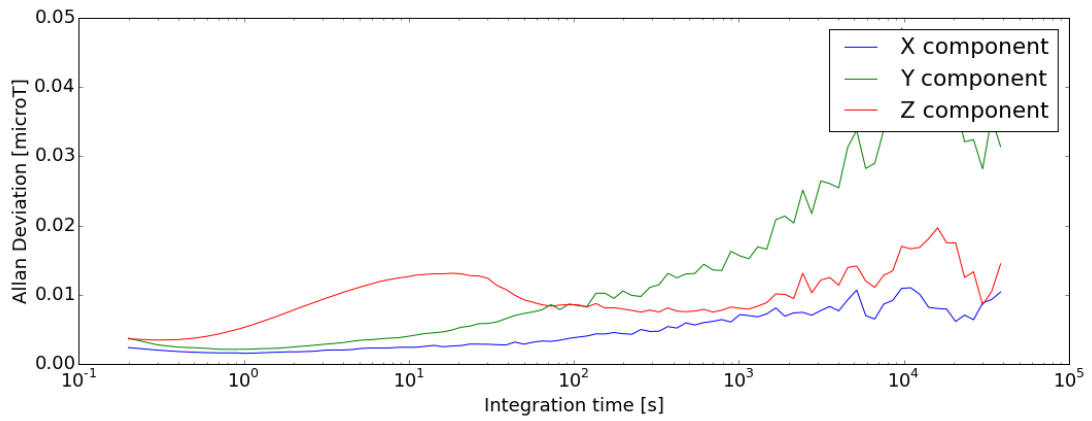
(a) Non-compensated field calculated using information about the currents
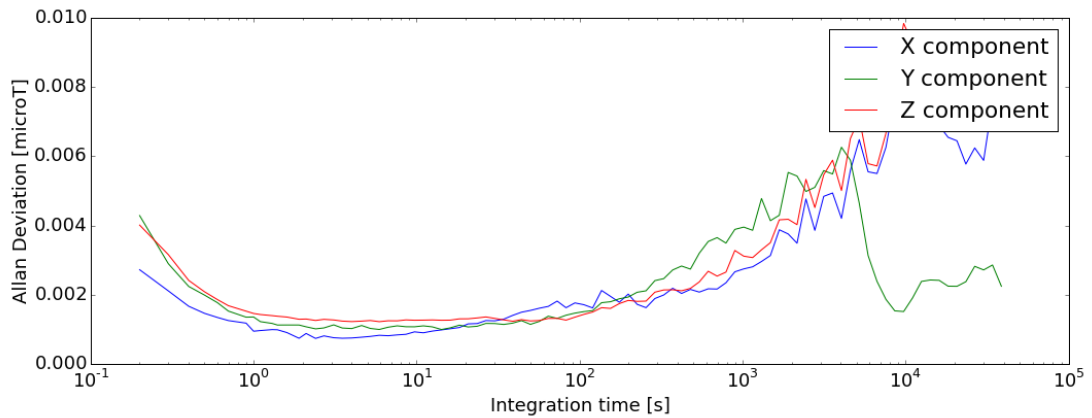


(b) Compensated field

Figure 4.19: Allan deviation of magnetic field measured (compensated) and calculated using the information about the currents in coils (non-compensated) for the 12-coil system
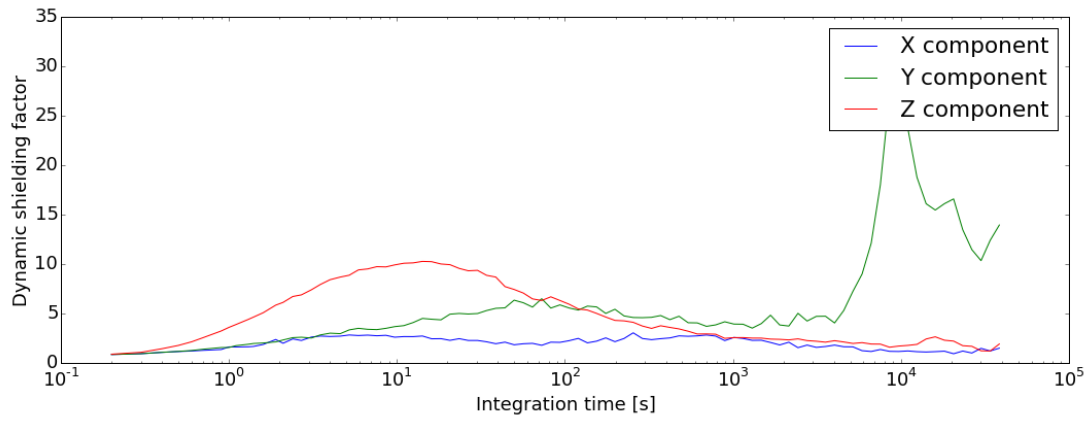
(a) $\alpha = 0$ (no regularization)
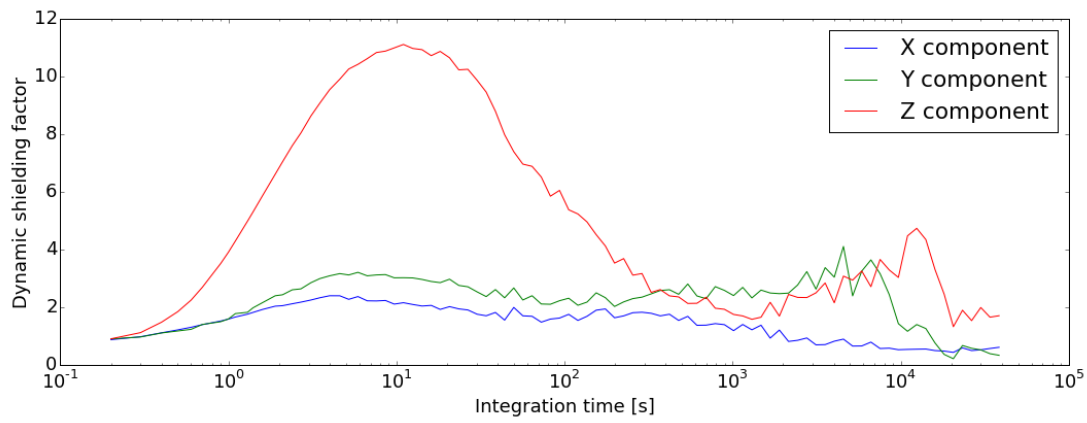
(b) $\alpha = 0.06$ (optimal regularization)
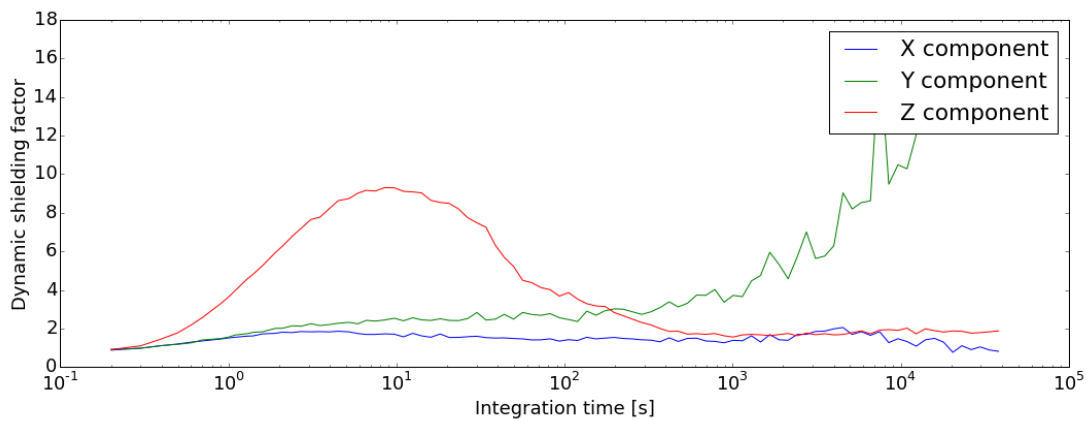
(c) $\alpha = 0.1$ (over-regularization)

Figure 4.20: Dynamic shielding factors for the different regularization constant $\alpha$ used to calculate the pseudoinverse of the response matrix $\mathbf{G}$.

## 4.2.4 Possible improvements
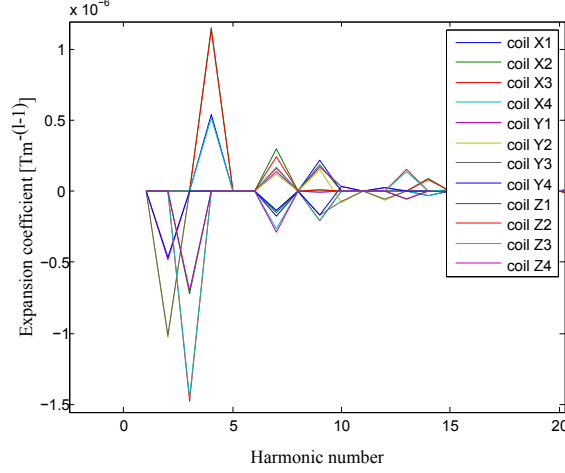


Figure 4.21: Decomposition of 12 Merritt coils into Cartesian harmonic functions.

Merritt coil setup is designed to generate uniform magnetic fields. Looking at calculated decomposition of the field created by those coils into Cartesian harmonics (see Fig. 4.21) one realizes, that the first three coefficients are the biggest. However, more important for compensation are the next 5 components representing the first order gradients. Unfortunately, three of those gradients cannot be compensated by this set of coils, because neither of the coils can generate the field described by any of following functions:

$$\vec{B}_{l=2,m=-2} \propto \text{grad}(xy) \tag{4.16}$$

$$\vec{B}_{l=2,m=-1} \propto \text{grad}(xz) \tag{4.17}$$

$$\vec{B}_{l=2,m=1} \propto \text{grad}(yz). \tag{4.18}$$

These fields can be generated by an additional 12 coils positioned diagonally with respect to Merritt coils. The resulting setup is shown in Fig. 4.22, where the additional coils are marked with yellow colour.

The map of the average $\Delta$ is presented in Fig. 4.23, showing improved performance with respect to the 12-coil system. What is interesting, is the small change in performance when the source of disturbance is moving closer. Further discussion of those two systems is done in Sec. 5.
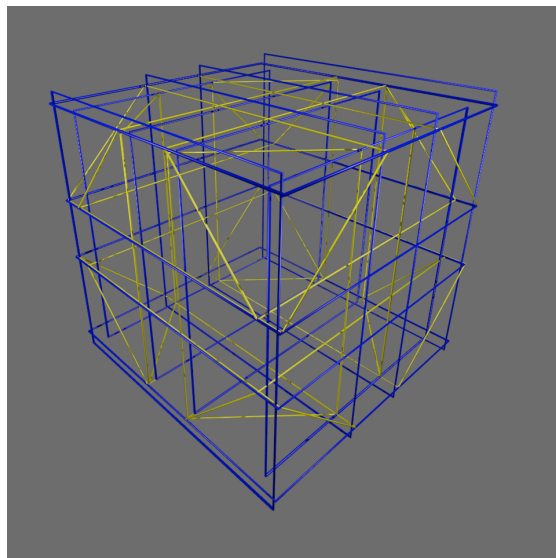
Figure 4.22: Proposition of additional 12 coils to the Merritt-based compensation system. Twelve Merritt setup coils are marked with blue colour, while additional 12 diagonal coils are marked with yellow colour.
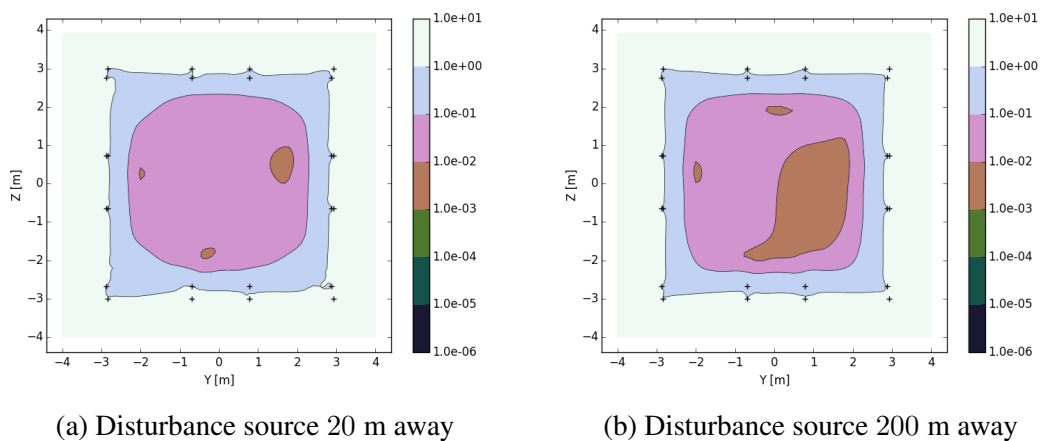


(a) Disturbance source 20 m away

(b) Disturbance source 200 m away

Figure 4.23: Maps of the simulated average $\Delta$ for the magnetic field compensation system consisting of 12 Merritt coils and additional 12 diagonal coils. Disturbance sources are located, randomly, 20 m and 200 m away from the centre of system. The map plane is at $x = 0.01$ m. The coil positions are marked with a black circle.

## 4.3 Cellular system

Another approach, considered in this thesis, is based on the operation principle of passive magnetic shields. The ferromagnetic and superconducting closed shields compensate, with eddy currents, the magnetic field component perpendicular to the surface. The same approach is used in the "cellular coil" system.

The cellular system consists of a large number of square coils, located on the surface of the controlled volume. They cover it completely. The feedback sensors would be positioned in the centre of each coil. Two cubic examples of coils for such a system are shown in Fig. 4.24.



(a) 6x9 coils          (b) 6x64 coils
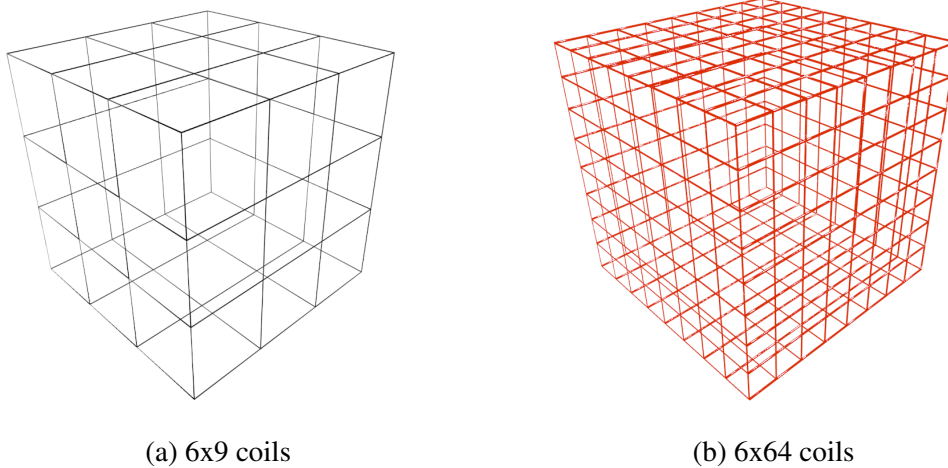
Figure 4.24: Cellular coil systems

### 4.3.1 Considered configurations

There are two parts of this system which can be optimized: (i) the number of coils and (ii) the feedback system. We consider systems being built up from $6 \times 9$ and $6 \times 64$ coils. In both cases, the feedback sensors are positioned in the centres of all coils, giving $54$ and $384$ measurement points, respectively.

Three possibilities of the feedback system were considered:

**Local scalar feedback mode** – Each loop compensates only the field component normal to the loop plane, measured in the loop centre. The maps of $\Delta$ being a result

of this method of calculation of currents are presented in Fig. 4.25.

**Global scalar feedback mode** – One dimensional sensors in the centre of each of the coils send the measured field value to the main controller, which uses the whole information to calculate the necessary reaction currents. The response matrix relating currents and fields generated by individual coils has the square matrix form, hence no regularization is needed. The $\Delta$ maps corresponding to this way of operation are presented in Fig. 4.26.

**Global vector feedback mode** – Three-dimensional sensors located in the centre of each coil send the full information about the measured field to the main controller. In this way, more measurements are generated than needed, meaning that the regularization may be advantageous. This solution is the most advanced and expensive because of price of three-dimensional sensors. The results of simulations for this mode are presented in Fig 4.27. Application of regularization (see Sec. 4.1) improves the performance significantly, as shown in Fig. 4.28.

The maps of $\Delta$ presented in Figs. 4.25 - 4.28 prove that the choice of the calculation method of the reaction currents is crucial for this family of compensation systems. The global vector feedback model is beneficial over the global scalar model only, if the regularization is applied.

What is interesting in the non-regularized feedback modes is that $\Delta$ is uniformly distributed inside the controlled volume. Also, there is no significant change in values of $\Delta$ when changing the distance to the disturbance source. However, the overall performance is poor.
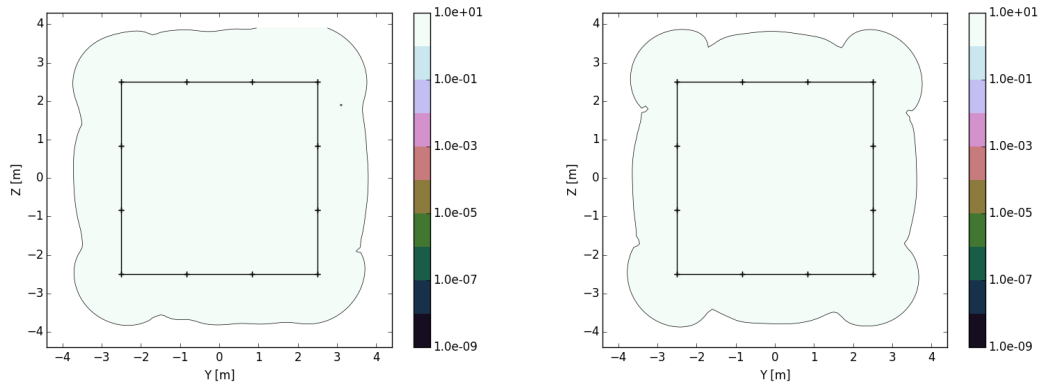
(a) 6x 9 coil system
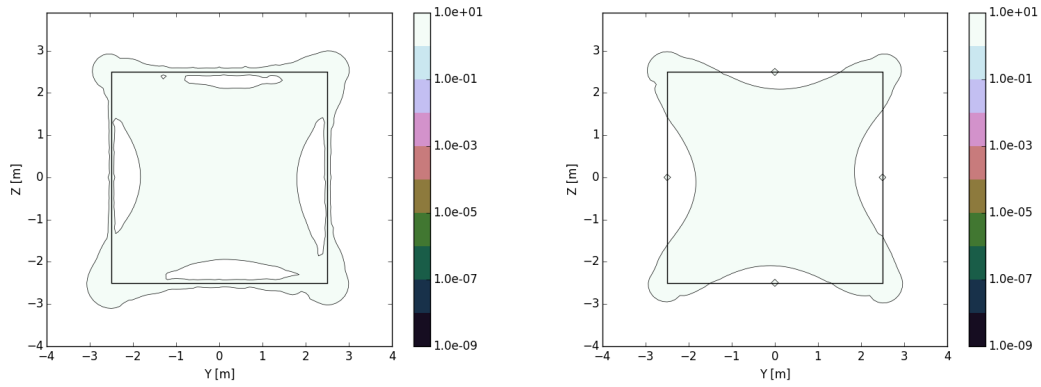


(b) 6x64 coil system

Figure 4.25: Maps of simulated average $\Delta$ (See Eq.(3.1)) for small coil-based magnetic field compensation systems (local scalar feedback mode) for disturbance sources located randomly 20 m away from the centre of system – left panel and 200 m – right panel. Map plane is at $x = 0.01$ m. The coil positions are marked with black crosses.
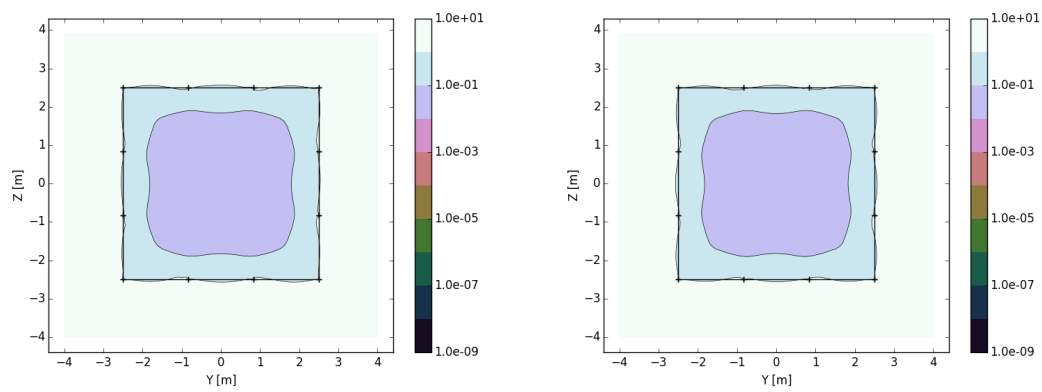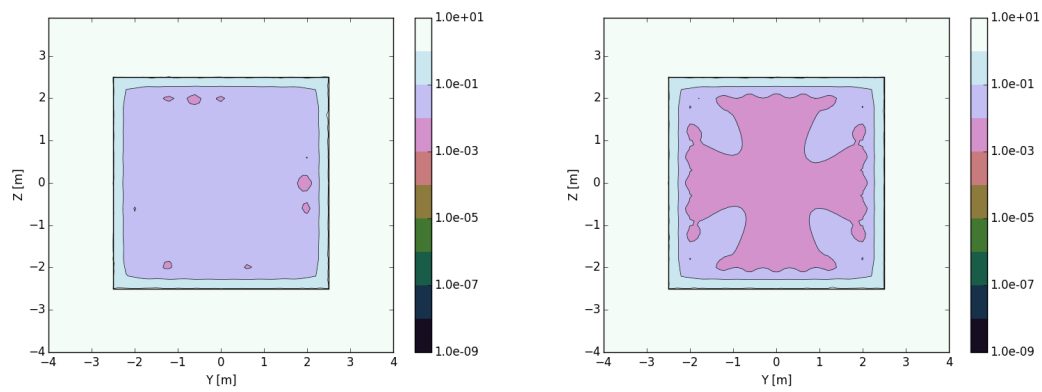
(a) 6x 9 coil system



(b) 6x64 coil system

Figure 4.26: Same as Fig. 4.25 but for the global scalar feedback mode.
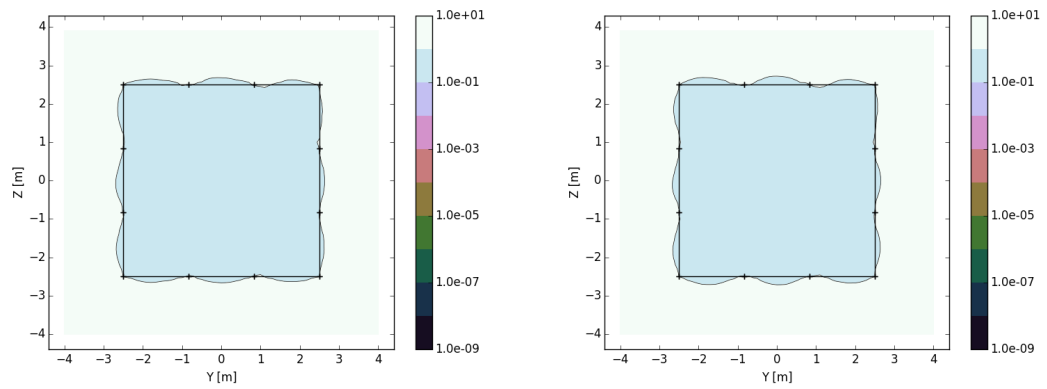
(a) 6x 9 coil system
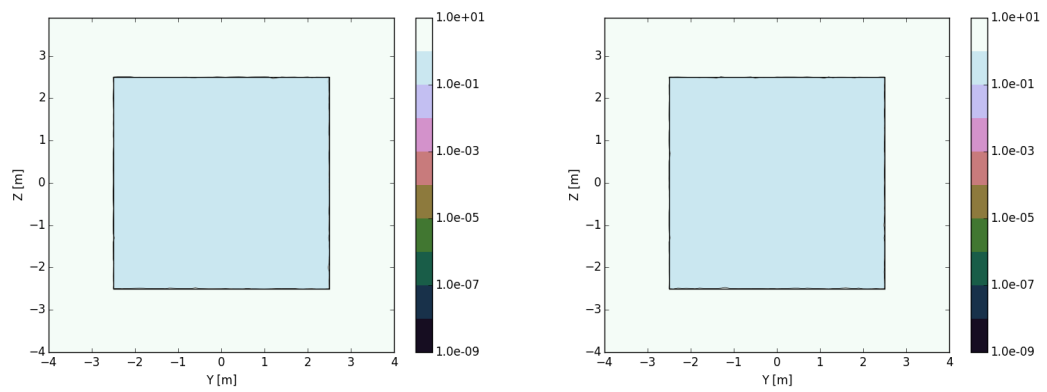


(b) 6x64 coil system

Figure 4.27: Same as Fig. 4.25 but for the non-regularized global vector feedback mode.
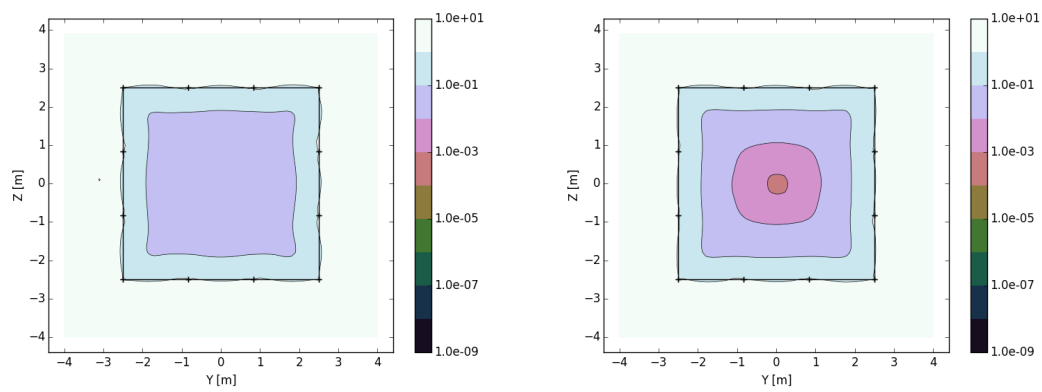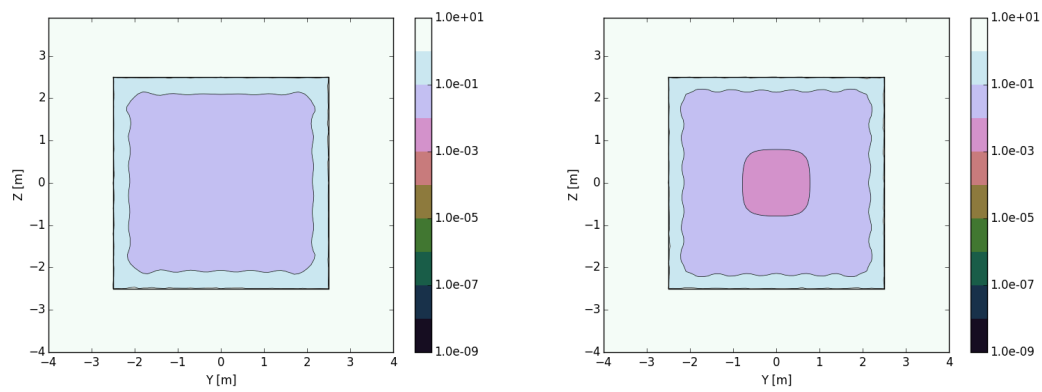
(a) 6x 9 coil system



(b) 6x64 coil system

Figure 4.28: Same as Fig. 4.25 but for the regularized global vector feedback mode.

## 4.4 Spherical coils

After a relatively modest level of improvement offered by advanced rectangular coil systems as compared to a simple 3-pair Helmholtz system (SFC), we decided to follow a more general approach which does not assume any specific coil shape right at the beginning. Rather the coil shape will be deduced mathematically. The starting point for this approach will be the decomposition of the static magnetic field in terms of the vector spherical harmonics [60], which are orthogonal functions. The coil will be designed such that one particular coil generates a single (orthogonal) spherical field component.

### 4.4.1 Magnetic field decomposition in terms of vector spherical harmonics
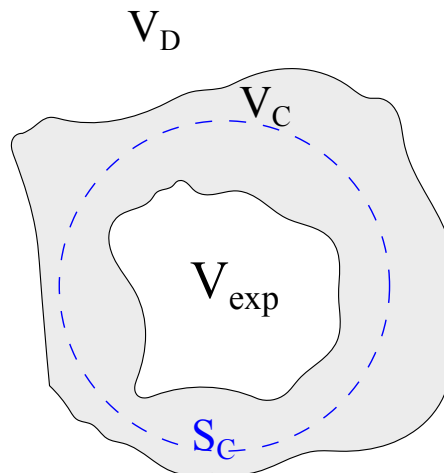


Figure 4.29: The definition of geometrical components used in the derivation of the spherical coil system. $V_{exp}$ is the volume, where the field is supposed to be compensated. $V_C$ is the volume, where compensating coils are supposed to be located. $S_C$ is the surface (see section 4.5), on which the solutions for coil turns will be obtained. $V_D$ is the volume, where the disturbing field originates from.

The general situation is illustrated in Fig. 4.29. We divide the whole space into three distinct regions. The central volume called the controlled volume $V_{exp}$ is free of magnetic field sources (electric currents) and is supposed to also be free of magnetic fields penetrating from external sources when the compensation system is active. The

controlled volume $V_{exp}$ is surrounded by a shell $V_C$ where electrical currents of the compensation system are contained. Outside $V_C$, in the volume $V_D$, magnetic field disturbances will be generated. $S_C$ is the surface, on which the solutions for coil turns will be obtained. We assume that all materials within $V_{exp}$ are isotropic and non-magnetic ($\mu_r = 1$) leading to the scalar magnetic potential $\phi(\vec{r})$, which has to fulfil the Laplace equation.

Electrical currents in the shell $V_C$ generate a magnetic field fulfilling Ampere's law:

$$\nabla \times \nabla \times \vec{A} = \mu_0 \vec{J}, \tag{4.19}$$

where $\vec{A}$ is a vector potential and $\vec{J}$ is a current density.

**Spherical harmonic decomposition of the scalar potential**

In the spherical coordinate system, the scalar potential $\phi(\vec{r})$ - the solution of the Laplace equation - is a series of spherical harmonics:

$$\phi(\vec{r}) = \sum_{l=0}^{\infty} \sum_{m=-l}^{l} \phi_{lm} r^l Y_{lm}(\theta, \varphi), \tag{4.20}$$

where a set of $\{\phi_{lm}\}$ describes, uniquely, the scalar potential function.

For not too large field disturbances coming from external sources one expects in the neighbourhood of the origin a fast convergence of expression (4.20). Only the first few terms with small $l$ values will contribute to the field description. An additional advantage of this form comes from the orthogonality of spherical harmonics. If the external field changes only a limited number of the terms in Eq. (4.20), then the reacting compensation system will have to drive currents only to the corresponding coils without affecting others.

**Current density distribution**

In order to compensate a field disturbance in the controlled volume $V_{exp}$, one has to drive currents in the shell $V_C$ such that the magnetic field distribution caused in $V_{exp}$ has the same amplitude as the disturbance and opposite sign. This problem is often referenced as the "Inverse source problem" (see e.g. Ref. [61]) and has been the subject

of many studies. Here we will present an analytical solution for a system exhibiting spherical symmetry. To accomplish this we begin with a synopsis of the vector spherical harmonics (VSH) essentials. A more detailed discussion can be found e.g. in [60]. Vector spherical harmonics are related to the scalar spherical harmonics in the following way:

$$\vec{\Psi}_{lm}(\theta, \varphi) \equiv r\nabla Y_{lm}(\theta, \varphi) \tag{4.21}$$

$$\vec{Y}_{lm}(\theta, \varphi) \equiv \hat{r} Y_{lm}(\theta, \varphi) \tag{4.22}$$

$$\vec{\Phi}_{lm}(\theta, \varphi) \equiv \hat{r} \times \vec{\Psi}_{lm}(\theta, \varphi). \tag{4.23}$$

This triad is a complete and orthogonal basis set, meaning that any vector function can be expressed as a series of VSH:

$$\vec{f}(r, \theta, \varphi) = \sum_{l=1}^{\infty} \sum_{m=-l}^{l} f_{lm}^Y(r)\vec{Y}_{lm}(\theta, \varphi) + f_{lm}^\Phi(r)\vec{\Phi}_{lm}(\theta, \varphi) +$$
$$+ f_{lm}^\Psi(r)\vec{\Psi}_{lm}(\theta, \varphi), \tag{4.24}$$

where $f_{lm}^Y$, $f_{lm}^\Psi$, $f_{lm}^\Phi$ are the coefficients given by:

$$f_{lm}^Y = \int d\Omega \vec{f} \cdot \vec{Y}_{lm}^\star \tag{4.25}$$

$$f_{lm}^\Psi = \frac{1}{l(l+1)} \int d\Omega \vec{f} \cdot \vec{\Psi}_{lm}^\star \tag{4.26}$$

$$f_{lm}^\Phi = \frac{1}{l(l+1)} \int d\Omega \vec{f} \cdot \vec{\Phi}_{lm}^\star. \tag{4.27}$$

A significant advantage of VSH is their well known behaviour under the action of differential operators (see Ref. [60]).

After acting with a gradient operator on these functions we get a description of the magnetic field in terms of the vector spherical harmonics:

$$\vec{B} = -\nabla\phi_M = -\sum_{l=0}^{\infty} \sum_{m=-l}^{l} \left(\frac{d}{dr}\phi_{lm}(r)\right)\vec{Y}_{lm} + \frac{\phi_{lm}(r)}{r}\vec{\Psi}_{lm}. \tag{4.28}$$

In Eq. 4.28, there is no component proportional to $\vec{\Phi}_{l,m}$ because this vector spherical

harmonic cannot be a result of a gradient operator acting on any function. The aim of this calculation is to find the current density, which would generate magnetic field described in equation (4.28). To achieve this, it is necessary to abandon the assumption that $\vec{J} = 0$ and solve the Ampere's law (in differential form):

$$\nabla \times \vec{B} = \nabla \times \left( \nabla \times \vec{A} \right) = \frac{4\pi}{c} \vec{J}. \tag{4.29}$$

General vector potential $A(r, \theta, \phi)$ can be decomposed into a series of vector spherical harmonics (compare Eq. (4.24)) :

$$\vec{A}(r, \theta, \phi) = \sum_{l=0}^{\infty} \sum_{m=-l}^{l} \left( A_{lm}^Y(r) \vec{Y}_{lm} + A_{lm}^\Psi(r) \vec{\Psi}_{lm} + A_{lm}^\Phi(r) \vec{\Phi}_{lm} \right). \tag{4.30}$$

Inserting the above series expansion into Eq. (4.29) leads to the current density form compatible to the (known) vector potential:

$$\vec{J}(r, \theta, \phi) = \sum_{l=0}^{\infty} \sum_{m=-l}^{l} \left( \frac{l(l+1)}{r^2} \left( A_{lm}^Y - \frac{d}{dr} r A_{lm}^\Psi \right) \vec{Y}_{lm} + \frac{1}{r} \frac{d}{dr} \left( A_{lm}^Y - \frac{d}{dr} r A_{lm}^\Psi \right) \vec{\Psi}_{lm} \right.$$
$$\left. + \frac{1}{r} \left( \frac{l(l+1)}{r} A_{lm}^\Phi - \frac{d^2}{dr^2} r A_{lm}^\Phi \right) \vec{\Phi}_{lm} \right). \tag{4.31}$$

Setting:

$$\vec{B} = \nabla \times \vec{A} \stackrel{!}{=} -\nabla \phi_M, \tag{4.32}$$

results in the condition that $\vec{A}$ should contain only the $\vec{\Phi}$ part of the series expansion which significantly simplifies Eq. (4.31):

$$\frac{1}{r^2} \frac{d}{dr} \left( r^2 \frac{d}{dr} A_{lm}^\Phi(r) \right) - \frac{l(l+1)}{r^2} A_{lm}^\Phi(r) = -\frac{4\pi}{c} J_{lm}^\Phi(r) \tag{4.33}$$

It is worth noticing that the application of the vector spherical harmonics reduces a 3-dimensional partial differential equation to an ordinary inhomogeneous differential equation.

The Green function (solution for $J_{lm}^\Phi = \delta(\vec{r} - \vec{r'})$) for this problem (for details see

Ref. [62]) is:

$$A^{\Phi}_{lm,G} = \frac{4\pi}{(2l+1)c} \frac{r^l_<}{r^{l+1}_>} (r')^2,$$ (4.34)

where:

$$(r_>, r_<) = \begin{cases} (r, r') & \text{for } r > r', \\ (r', r) & \text{for } r < r'. \end{cases}$$ (4.35)

It is assumed that currents flow outside $V_{exp}$. This means that the integration variable is limited to $r' > r$, which corresponds to the second case of (4.35), leading to

$$A^{\Phi}_{lm} = r^l \frac{4\pi}{(2l+1)c} \int_0^\infty (r')^{-l+1} J^{\Phi}_{lm}(r') \mathrm{d}r' \equiv r^l \alpha_{lm},$$ (4.36)

where $\alpha_{lm}$ is a coefficient which depends only on currents flowing outside the controlled volume $V_C$. After inserting (4.36) into Eq. (4.29) we obtain the expression for the magnetic field $\vec{B}$:

$$\vec{B} = \nabla \times \vec{A} = \sum_{l=0}^\infty \sum_{m=-l}^l \alpha_{lm} \nabla \times \left( r^l \vec{\Phi}_{lm}(\theta, \phi) \right)$$

$$= \sum_{l=0}^\infty \sum_{m=-l}^l \left( -\frac{l(l+1)}{r} r^l \vec{Y}_{lm} - \frac{1}{r} \frac{\mathrm{d}}{\mathrm{d}r} r^{l+1} \vec{\Psi}_{lm} \right) \alpha_{lm}.$$ (4.37)

Comparing equations (4.37) and (4.28), one can easily find that the scalar potential is given by:

$$\phi_{lm}(r) = (l+1) r^l \alpha_{lm} = \frac{4\pi}{c} r^l \frac{l+1}{2l+1} \int_0^\infty (r')^{-l+1} J^{\Phi}_{lm}(r') \mathrm{d}r',$$ (4.38)

This means, that to generate magnetic field related to scalar potential with only one spherical harmonic $\phi_M = r^l \phi_{l'm'} Y_{l'm'}$ term, it is sufficient to use the current described by the single harmonic of the same rank $\vec{j} = J^{\Phi}_{l'm'} \vec{\Phi}_{l'm'}$. This property makes it possible to generate each term of the field expansion in Eq. (4.28), independently.

**General current densities**

If we relax the constraints of an infinitely thin current density (the coefficients $J_{lm}^Y$ and $J_{lm}^\Psi$ do not vanish any more), we obtain the general expression:

$$\mu_0 \vec{J}(r,\theta,\varphi) = \sum_{l=0}^{\infty} \sum_{m=-l}^{l} \left( \frac{l(l+1)}{r^2} \left( A_{lm}^Y - \frac{d}{dr} r A_{lm}^\Psi \right) \vec{Y}_{lm} + \right.$$
$$+ \frac{1}{r} \frac{d}{dr} \left( A_{lm}^Y - \frac{d}{dr} r A_{lm}^\Psi \right) \vec{\Psi}_{lm} +$$
$$\left. + \frac{1}{r} \left( \frac{l(l+1)}{r} A_{lm}^\Phi - \frac{d^2}{dr^2} r A_{lm}^\Phi \right) \vec{\Phi}_{lm} \right). \tag{4.39}$$

Making use of the continuity relation for current ($\nabla \cdot \vec{J} = 0$) and Gauss's law for magnetism ($\nabla \cdot \vec{B} = 0$), as well as exploiting the relations for the divergence of the VSH, we arrive at:

$$J_{lm}^\Psi(r) = \frac{1}{l(l+1)} \frac{1}{r} \frac{\mathrm{d}}{\mathrm{d}r} \left( r^2 J_{lm}^Y(r) \right) \tag{4.40}$$

$$A_{lm}^\Psi(r) = \frac{1}{l(l+1)} \frac{1}{r} \frac{\mathrm{d}}{\mathrm{d}r} \left( r^2 A_{lm}^Y(r) \right). \tag{4.41}$$

This means that the $Y$ and $\Psi$ parts of the series expansion of $\vec{A}$ and $\vec{J}$ (see Eqns. (4.24) and (4.30)) are dependent and only one of them needs to be considered, e.g. $Y$. From the rotation of VSH (see [60]), we get:

$$\mu_0 J_{lm}^Y(r) = -\frac{l(l+1)}{r} B_{lm}^\Phi(r), \tag{4.42}$$

where $B_{lm}^\Phi(r)$ is the function describing the expansion of the magnetic field into $\vec{\Phi}$ component of the VSH. This means that for $\vec{x} \in V_{exp}$, ($\vec{J} = 0$) also

$$\vec{B}_{lm}^\Phi(r(\vec{x})) = 0. \tag{4.43}$$

The conclusion is that in the current density expansion in $V_C$ the terms proportional to $\vec{Y}_{lm}(\theta,\varphi)$ and $\vec{\Psi}_{lm}(\theta,\varphi)$ do not contribute to the field generated in the controlled volume $V_{exp}$. This means that only currents flowing on the surface of the sphere generate field

inside that sphere.

### Verification

To verify this description of the field, two simple configurations with known analytic solutions are used: (i) a single current loop and (ii) a Helmholtz coil pair.
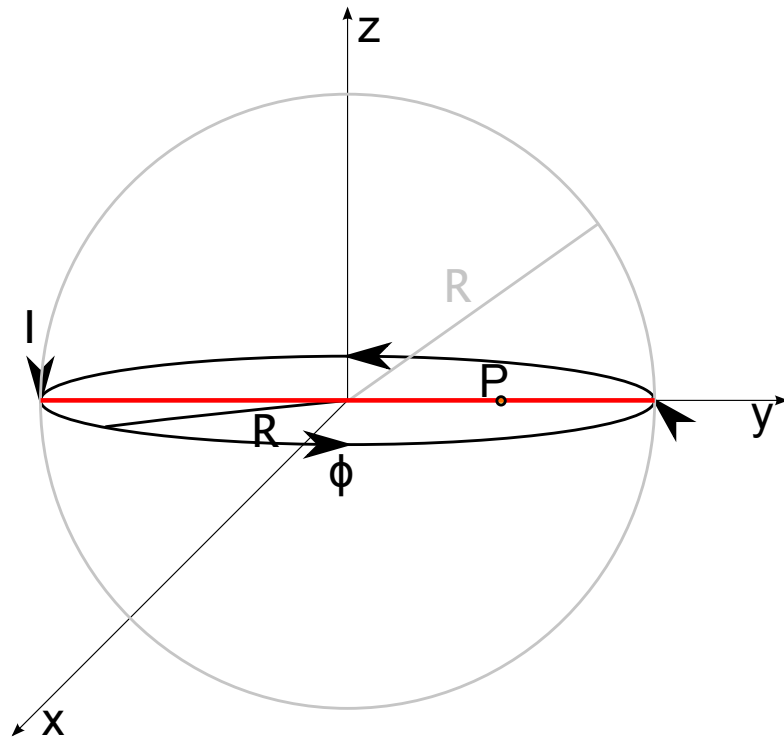


Figure 4.30: Single loop with current. Current flows in a $\hat{\phi}$ direction. The path marked with a thick red line and point $P$ are used for a visualisation of results.

**(i) Single loop** The configuration used in this calculation is shown in Fig. 4.30. The current density function is described by:

$$\vec{J}(r, \theta, \phi) = I\delta(\cos\theta)\frac{\delta(r-R)}{R}\hat{\phi} \tag{4.44}$$

The coefficients for the vector spherical harmonic expansion series can by calculated by the integration:

$$J_{lm}^{(2)}(r) = \frac{1}{l(l+1)} \int_\Omega \mathrm{d}(\cos\theta)\mathrm{d}\phi \vec{J} \cdot \vec{\Phi}_{lm}^* =$$

$$= \frac{I}{l(l+1)R}\delta(r-R) \int_0^{2\pi} \left.\frac{\partial}{\partial\theta}Y_{lm}^*\right|_{\theta=\pi/2} \mathrm{d}\phi. \tag{4.45}$$

This integral equals 0 for every $m \neq 0$. For $m = 0$ one obtains:

$$J_{l0}^{(2)} = \frac{2\pi I}{l(l+1)R}\delta(r-R)\left.\frac{\partial}{\partial\theta}Y_{lm}^*\right|_{\theta=\pi/2} \tag{4.46}$$

$$\alpha_{l0} = \frac{8\pi^2 I}{(2l+1)l(l+1)c}R^{-l+1}\left.\frac{\partial}{\partial\theta}Y_{lm}^*\right|_{\theta=\pi/2} \tag{4.47}$$

$$\vec{B}(r,\theta,\phi) = -\sum_{l=1}^{\infty} l(l+1)r^{l-1}\alpha_{l0}\vec{Y}_{l0} - (l+1)r^{l-1}\alpha_{l0}\vec{\Psi}_{l0} \tag{4.48}$$

Spherical harmonics for $m = 0$ become proportional to Legendre Polynomials $Y_{l0}(\theta) \propto P_l^0(\cos(\theta))$. From [63]:

$$\left.\frac{\mathrm{d}\,P_\nu^\mu(x)}{\mathrm{d}\,x}\right|_{x=0} = 2^{\mu+1}\pi^{-\frac{1}{2}}\sin\left(\frac{1}{2}\pi\left(\nu+\mu\right)\right)\frac{\Gamma\left(\frac{1}{2}\nu+\frac{1}{2}\mu+1\right)}{\Gamma\left(\frac{1}{2}\nu-\frac{1}{2}\mu+1\right)}, \tag{4.49}$$

where $\Gamma$ is the Gamma function. For $\mu = 0$, $\nu = l$ and $x = \cos(\theta)$:

$$\left.\frac{\mathrm{d}\,P_l(\cos\theta)}{\mathrm{d}(\cos\theta)}\right|_{\theta=\frac{\pi}{2}} = 2\pi^{-\frac{1}{2}}\sin\left(\pi\frac{l}{2}\right), \tag{4.50}$$

which is equal to $0$ for even values of $l$. This means that in the expansion in Eq. (4.48) $l$ takes only odd values. For comparison, we use analytic expressions for the magnetic field taken from [64]:

$$B_x^{theor} = \frac{Cxz}{2\alpha^2\beta\rho^2}\left((a^2+r^2)E(k^2) - \alpha^2 K(k^2)\right) \tag{4.51}$$

$$B_y^{theor} = \frac{Cyz}{2\alpha^2\beta\rho^2}\left((a^2+r^2)E(k^2) - \alpha^2 K(k^2)\right) \tag{4.52}$$

$$B_z^{theor} = \frac{C}{2\alpha^2\beta}\left((a^2-r^2)E(k^2) + \alpha^2 K(k^2)\right), \tag{4.53}$$

where: $\rho^2 = x^2 + y^2$, $r^2 = x^2 + y^2 + z^2$, $\alpha^2 = a^2 + r^2 - 2a\rho$, $\beta^2 = a^2 + r^2 + 2a\rho$, $k^2 = 1 - \alpha^2/\beta^2$, $\gamma = x^2 - y^2$, $C = \mu_0 I/\pi$, $E(k^2)$ is a complete elliptic integral of a second kind and $K(k^2)$ is the complete elliptic integral of the first kind [63]:

$$K(k^2) = \int_0^{\pi/2} \left(1 - k^2\sin^2\theta\right)^{-1/2} d\theta$$

$$E(k^2) = \int_0^{\pi/2} \left(1 - k^2\sin^2\theta\right)^{1/2} d\theta.$$

The first way to compare the exact predictions (equations (4.51), (4.52) and (4.53)) with calculations using the vector spherical harmonics (equation (4.48)) was by plotting $B_Z$ component along $x = 0, z = 0$ axis (see red axis in Fig. 4.30). Exact value and values calculated for the VSH expansion cut off to $l = 1, 3, 5$ are shown in Fig. 4.31, while the relative difference of them is presented in Fig. 4.32.

In Fig. 4.33, we present a relative difference at the point P (Fig. 4.30) as a function of $l_{max}$, at which the VSH expansion series is cut off. The last parameter, which was calculated, is the "radius of convergence" ($r_{min}$). It is the maximum size of a sphere, inside which the maximum relative difference is less than $0.01$ (set arbitrarily). $r_{min}$ is interpreted as the size of spherical control volume, therein the relative error in the reproduction of the magnetic field by the truncated VHS series is less than $0.01$.
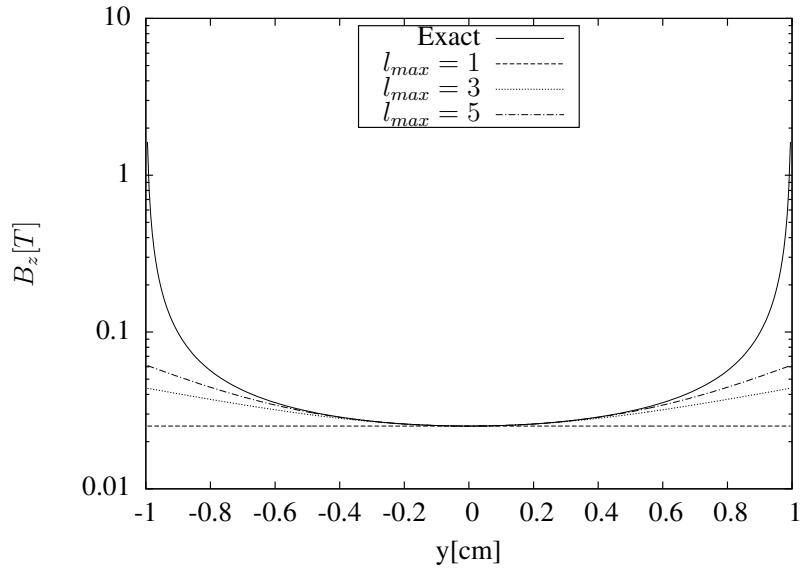
Figure 4.31: $z$ component of magnetic field on $x = 0, y = 0$ axis for exact analytical solution and VSH series expansion ending on $l = 1, l = 3$ and $l = 5$ for a single current loop
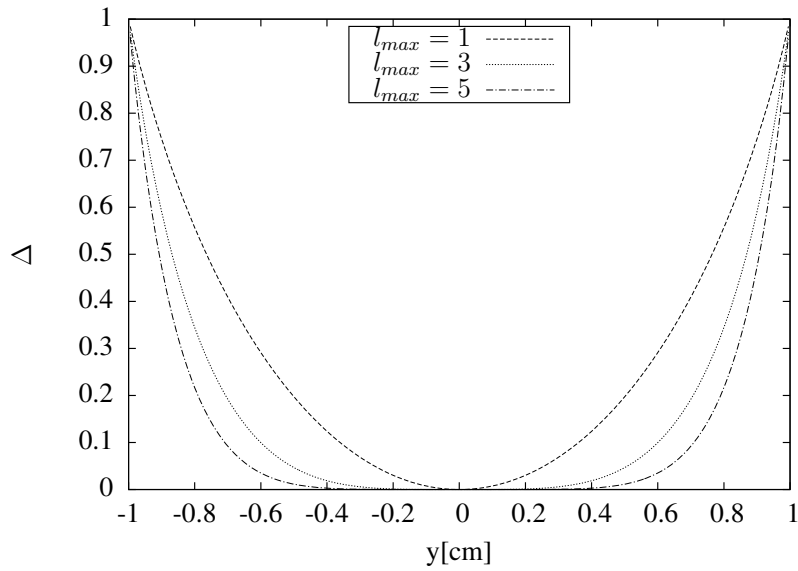


Figure 4.32: Relative difference between the analytical $\vec{B}$ and the one calculated with VSH for a single current loop in the function of the position on the axis $x = 0, z = 0$ ($\Delta = \left|\vec{B}_{exact} - \vec{B}_{approx}\right| / \left|\vec{B}_{exact}\right|$)
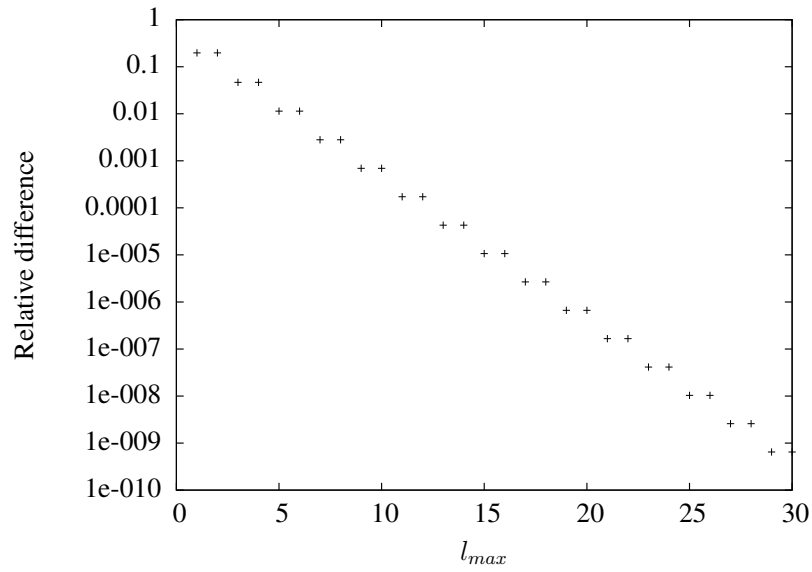
Figure 4.33: Relative difference between the analytical $B_z$ component and the one calculated as the VSH expansion as a function of the number of terms after which the series is cut off taken at point $P(0, 0.5, 0)$ (Fig. 4.30)
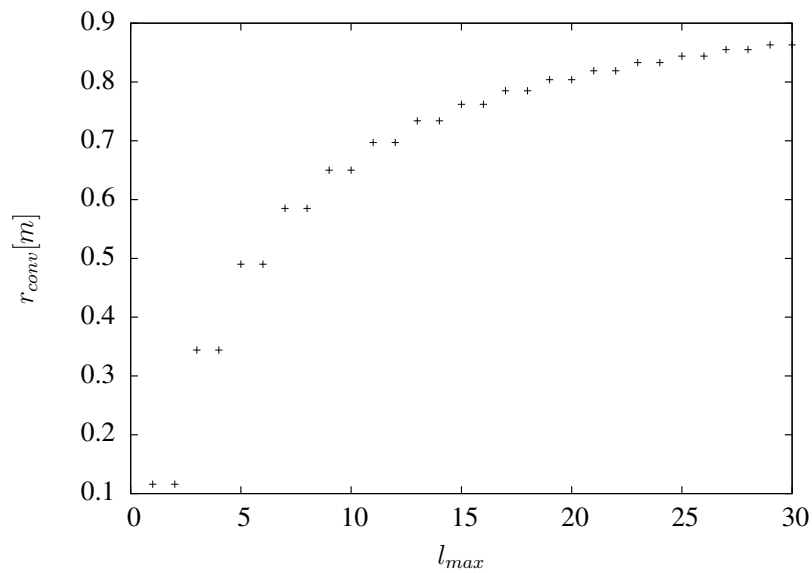


Figure 4.34: Radius of convergence for relative difference $< 0.01$ calculated along line with $\theta = \pi/2$, $\phi = \pi/2$ as a function of $l_{max}$, order after which the VSH expansion series is cut off
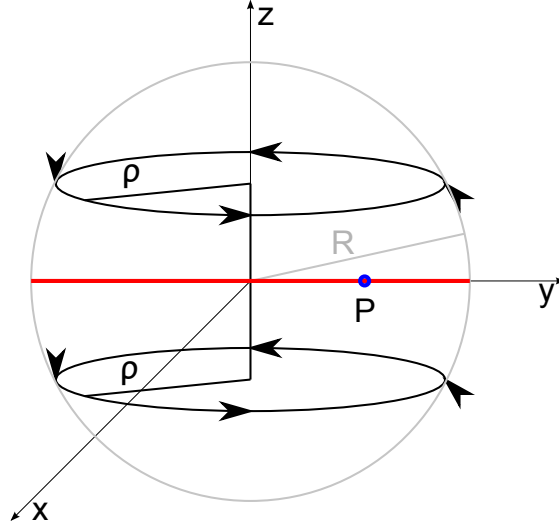
Figure 4.35: Helmholtz coil setup with definition of points and paths used in visualization of results. The path marked with a thick red line and point $P$ are used for visualisation of the results.

**(ii)Helmholtz coils** A similar test was made for Helmholtz coils. The setup is presented in Fig. 4.35. The current density function is expressed as:

$$\vec{J}(r, \theta, \phi) = I\left(\delta(\theta - \omega) + \delta(\theta - \pi + \omega)\right)\frac{\delta(r - R)}{R}\hat{\phi}, \tag{4.54}$$

$$\omega = \arctan 2$$

The coefficients for the VSH expansion are:

$$
\begin{aligned}
J_{lm}^{(2)} =& \frac{1}{l(l+1)} \int_{\Omega} \mathrm{d}(\cos\theta)\mathrm{d}\phi \vec{J} \cdot \vec{\Phi}_{lm}^{*} = \\
=& \frac{I\delta(r-R)\sin(\omega)}{l(l+1)R} \int_{0}^{2\pi} \left(\frac{\partial}{\partial\theta}Y_{lm}^{*}\bigg|_{\theta=\omega} + \frac{\partial}{\partial\theta}Y_{lm}^{*}\bigg|_{\theta=\pi-\omega}\right)\mathrm{d}\phi
\end{aligned}
\tag{4.55}
$$

This integrals are equal to zero, if $m \neq 0$. For $m = 0$:

$$J_{l0}^{(2)} = \frac{2\pi I\delta(r-R)\sin(\omega)}{l(l+1)R}\left(\frac{\partial}{\partial\theta}Y_{l0}^{*}\bigg|_{\theta=\omega} + \frac{\partial}{\partial\theta}Y_{l0}^{*}\bigg|_{\theta=\pi-\omega}\right) \tag{4.56}$$

$$\alpha_{l0} = \frac{8\pi^2 I}{(2l+1)l(l+1)c}R^{-l+1}\left(\frac{\partial}{\partial\theta}Y_{l0}^{*}\bigg|_{\theta=\omega} + \frac{\partial}{\partial\theta}Y_{l0}^{*}\bigg|_{\theta=\pi-\omega}\right) \tag{4.57}$$

$$\vec{B}(r, \theta, \phi) = -\sum_{l=1}^{\infty} l(l+1) r^{l-1} \alpha_{lm} \vec{Y}_{lm} - (l+1) r^{l-1} \alpha_{lm} \vec{\Psi}_{lm}. \tag{4.58}$$

For $l = 3$:

$$\frac{\partial}{\partial \theta} Y^*_{3,0} \bigg|_{\theta=\omega} = 0 \quad \text{and} \quad \frac{\partial}{\partial \theta} Y^*_{3,0} \bigg|_{\theta=\pi-\omega} = 0, \tag{4.59}$$

which is the reason why Helmholtz coils generate highly uniform magnetic field: coefficients for $l = 2$ and $l = 3$ are equal $0$, meaning that the most important non-uniform field component is $l = 5, m = 0$. This is why, in Figs. 4.36 and 4.37, plots for $l_{max} = 1$ and $l_{max} = 3$ are identical.

Analytical expressions for magnetic field for Helmholtz coils in cylindrical coordinates are (taken from [65]):

$$B_r^{anal} = \frac{\mu_0}{2\pi} \frac{I(z+R/2)}{r\left((R+r)^2 + (z+R/2)^2\right)^{1/2}} \left(-K_1 + \frac{R^2 + r^2 + (z+R/2)^2}{(R-r)^2 + (z+R/2)^2}\right) +$$
$$+ \frac{\mu_0}{2\pi} \frac{I(z-R/2)}{r\left((R+r)^2 + (z-R/2)^2\right)^{1/2}} \left(-K_2 + \frac{R^2 + r^2 + (z-R/2)^2}{(R-r)^2 + (z-R/2)^2}\right) \tag{4.60}$$

$$B_z^{anal} = \frac{\mu_0}{2\pi} \frac{I}{\left((R+r)^2 + (z+R/2)^2\right)^{1/2}} \left(K_1 + \frac{R^2 - r^2 - (z+R/2)^2}{(R-r)^2 + (z+R/2)^2}\right) +$$
$$+ \frac{\mu_0}{2\pi} \frac{I}{\left((R+r)^2 + (z-R/2)^2\right)^{1/2}} \left(K_2 + \frac{R^2 - r^2 - (z-R/2)^2}{(R-r)^2 + (z-R/2)^2}\right). \tag{4.61}$$

The $z$ component of magnetic field is plotted as a function of position for the exact solution and the VSH expansion series cut off after $l_{max} = 1, 3, 5$ in Fig. 4.36. For the same cases, relative difference is presented in Fig. 4.37. Relative difference at point P (see figure 4.35) is shown as a function of $l_{max}$ on figure 4.38. Radius of convergence for $\Delta < 0.01$ is shown in Fig. 4.39. Changes in monotonicity of the last two relations are caused by selection of point $P$ and the search path of the convergence radius. They are localized between two current loops, changing their position also changes the relations, e.g. Fig. 4.40.
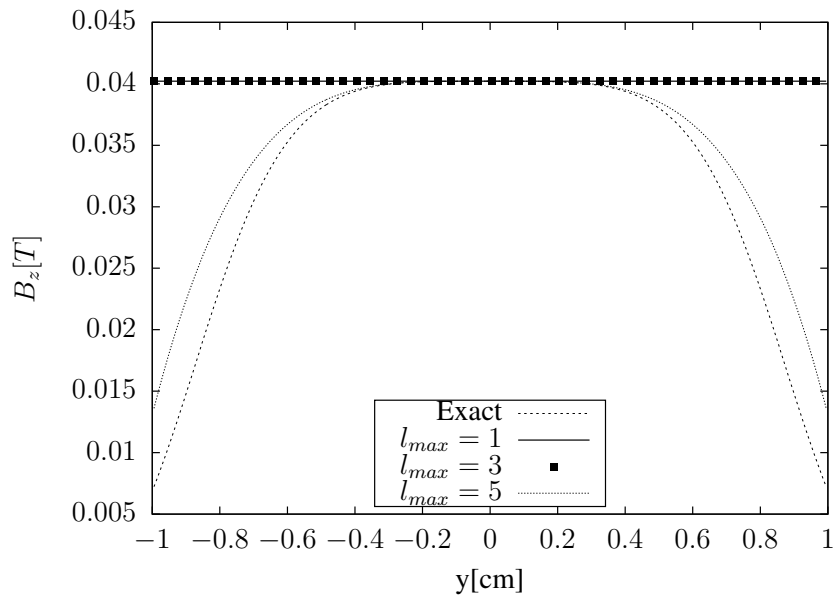
Figure 4.36: Comparison of exact solution of $z$ component of magnetic field generated by Helmholtz coil pair and the VSH series expansion cut off after $l_{max} = 1, 3, 5$ taken on $x = 0, z = 0$ axis
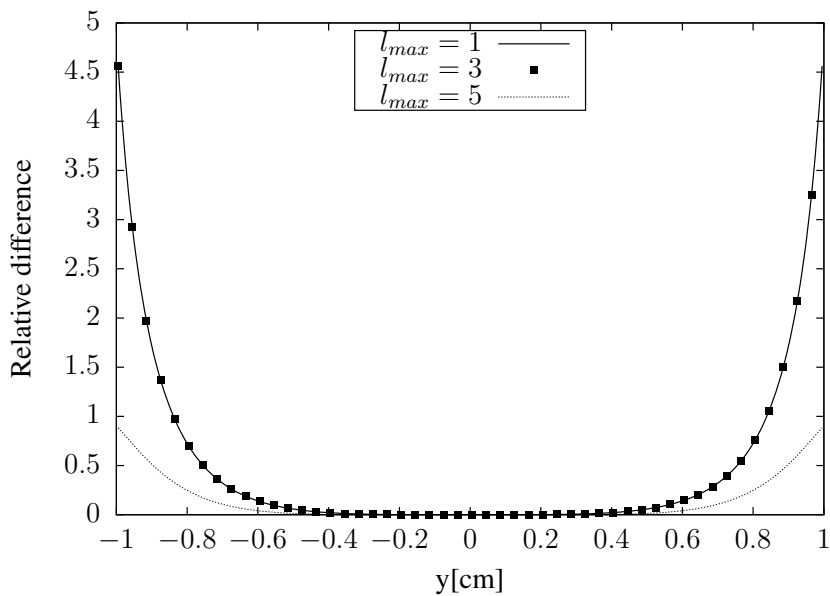


Figure 4.37: Relative difference between exact values and the VSH expansions series, cut off after $l_{max} = 1, 3, 5$ for a Helmholtz coil pair.
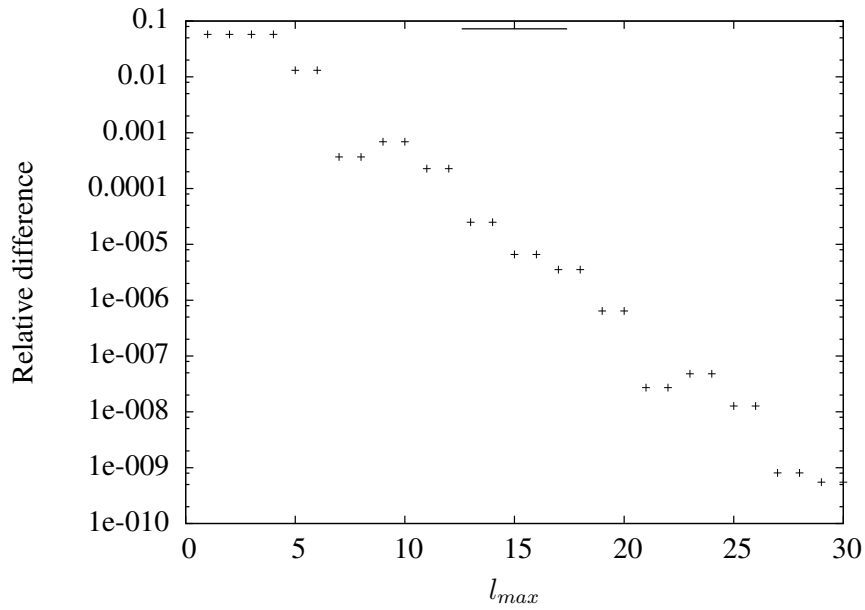
Figure 4.38: Relative difference between exact values and the VSH expansions series, taken at point $P(0, 0.5, 0)$ as a function of $l_{max}$, order after which the VSH expansion series is cut off for a Helmholtz coil pair
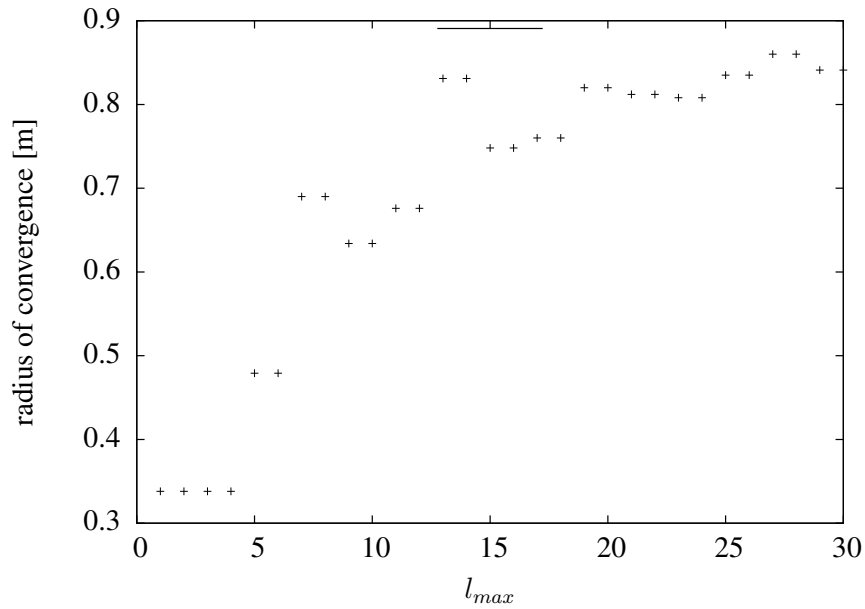


Figure 4.39: Convergence radius ($\Delta < 0.01$) for a Helmholtz coil pair.
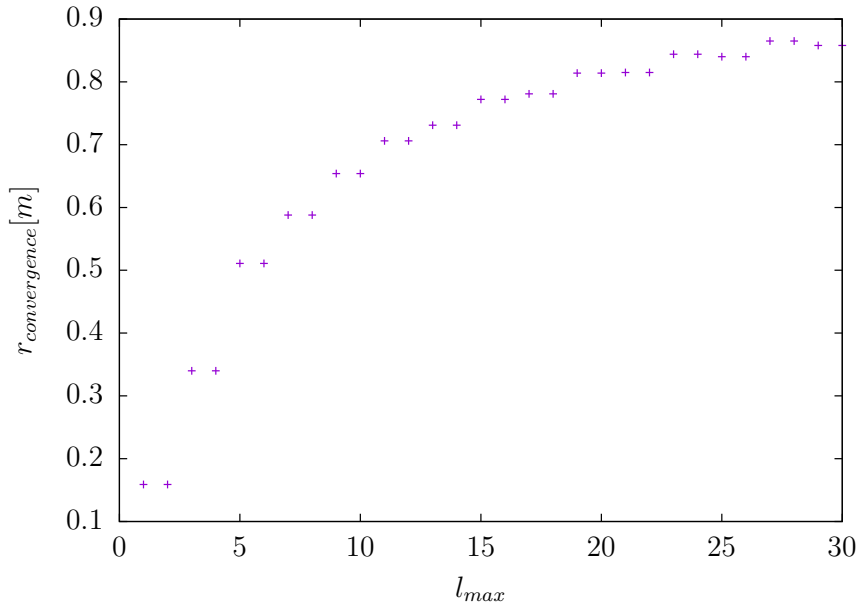
Figure 4.40: Convergence radius ($\Delta < 0.01$) for a Helmholtz coil pair, calculated along the axis with spherical coordinates $\theta = \pi/4$, $\phi = \pi/6$.

Above two examples show that the proposed description of magnetic field as the series of vector spherical harmonics is consistent. From the comparison between the exact magnetic field calculations and its approximation by the VSH expansion series, we can generalize that adding the following terms to the cut off series improves the average accuracy by almost an order of magnitude for each additional term. The level of improvement depends on the shape of the approximated field. Given the maximum $\Delta$ allowed in the control volume, it is possible to optimize the truncation point $l_{max}$. This can be performed using Figs. 4.39 and 4.34. For example, if the required accuracy is $\Delta < 0.01$ and the control volume is a sphere with $r = 0.5$ m, we would need $l_{max} = 7$ $((7 + 2) \cdot 7 = 63$ terms) to fulfil the requirement.

## 4.5 Coils - discretization of the current density distribution

In a practical application the required current density distribution $\vec{J}(x, y, z)$, where $(x, y, z) \in V_C$, will be generated using a coil system. We assume that coils consist of thin wire windings distributed on a sphere so that the volume $V_C$ reduces to a surface. Since all wire turns in a coil are connected serially, the only way to construct a given current density is by proper shaping and distributing of the wire turns. To perform this, we use the stream function from Ref. [66]. This approach is based on the fact that for a static current density function $\vec{J}(x, y, z)$ the divergence vanishes

$$\nabla \cdot \vec{J}(x, y, z) = 0. \tag{4.62}$$

If currents are constrained to a surface defined by a normal vector $\hat{\vec{n}}$, then the current density can be written as:

$$\vec{J}(x, y, z) = \nabla \psi(x, y, z) \times \hat{\vec{n}}, \tag{4.63}$$

where $\psi(x, y, z)$ is the so called stream function defined on the surface containing currents. This function must be differentiable on that surface. In order to fulfil the relation (4.62), it must be constant on the boundary of the surface leading to the requirement that currents are allowed to flow along the isolines of the stream function. We can identify the isolines with the coil wire turns.

Comparing Eq. (4.63) with the $\vec{\Phi}$ part of the VSH series in Eq. (4.23) we realize that wire turns of the spherical coils (isolines of $\vec{\Phi}$) are identical to the isolines of spherical harmonics.

$$\psi(x, y, z) \propto Y_{lm}(\theta, \varphi) \quad (x, y, z) = (r \sin\theta \cos\varphi, r \sin\theta \sin\varphi, r \cos\theta), \ r = const. \tag{4.64}$$

The necessary number of coil wire turns depends on the required field reproduction accuracy. Fig. 4.41 shows the dependence of the average relative reproduction accuracy as a function of the number of wire turns. Obviously, the more turns in a coil, the more accurate the reproduction of the continuous current distribution will be.

Figure 4.41: Accuracy of the current density discretization calculated with the stream function approach. Average relative error of the field reproduced by a coil with a given number of turns is shown for two coils: ($l = 1$, $m = 0$) - solid lines and ($l = 3$, $m = 2$) - dashed lines. The average is taken over the sphere with radius of $0.3R$ - black lines and $0.9R$ - grey lines. $R$ is the coil radius.

The example of such discretization on a sphere is presented in Fig. 4.42. For $l = 1$ the result was three coils (Fig. 4.42a), the so called $\cos\theta$ coils [67], identical to those obtained by J. E. Everett and J. E. Osemeikhian [68], produce a uniform magnetic field. Figures 4.42b and 4.42c present the wire distribution for $l = 2$ and $l = 3$, respectively.

For simulation done in this thesis, the isolines of spherical harmonics, which define the positions of wires, are calculated using the Marching Squares algorithm. It is a 2d modification of the Marching Cubes [69] algorithm, which allows to find isolines of functions using parallel processing. In this way, we used whole computing power of nVIDIA Tesla cards which were available gaining much performance in comparison to other, non-parallel algorithms.

## 4.5.1 Compensation performance

For comparison, we have used the coil systems with 8 and 15 coils. This shows how we can improve the compensation when adding higher orders to the VSH expansion series. Maps presented in Fig. 4.43 show the distribution of $\Delta$.
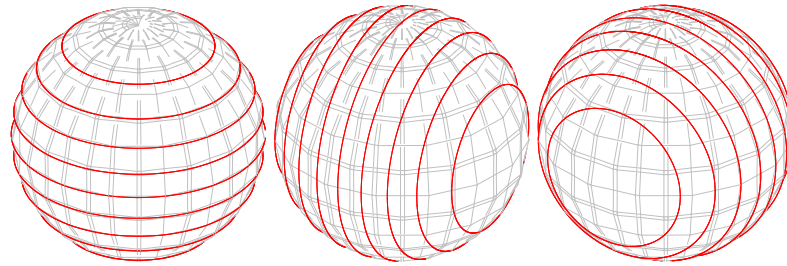
(a) Coils creating uniform magnetic fields ($l = 1$ case).
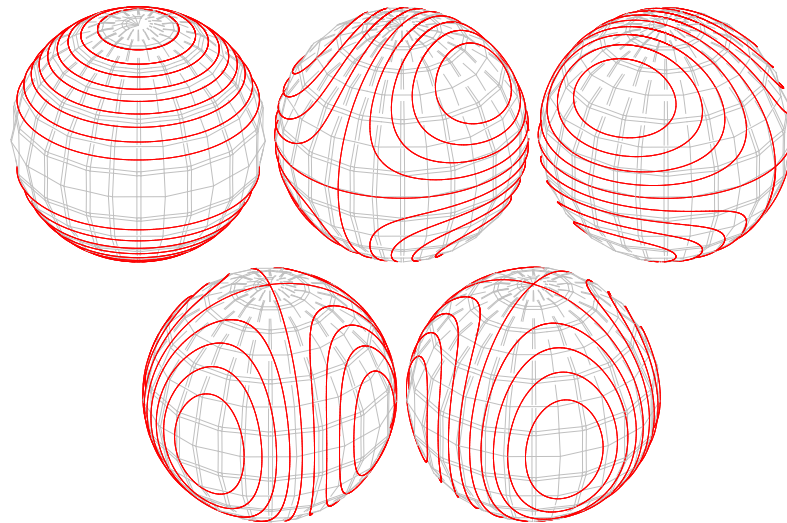


(b) Coils creating quadrupolar field($l = 2$ case).
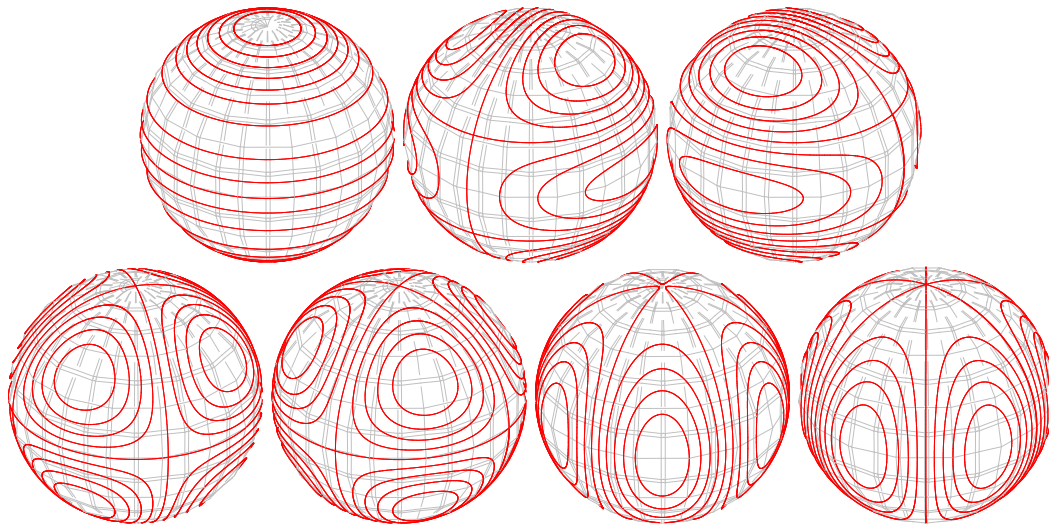


(c) Coils creating octupolar field ($l = 3$ case).

Figure 4.42: Coils wound on a sphere. For clarity, the number of turns is taken to be $n = 9$.
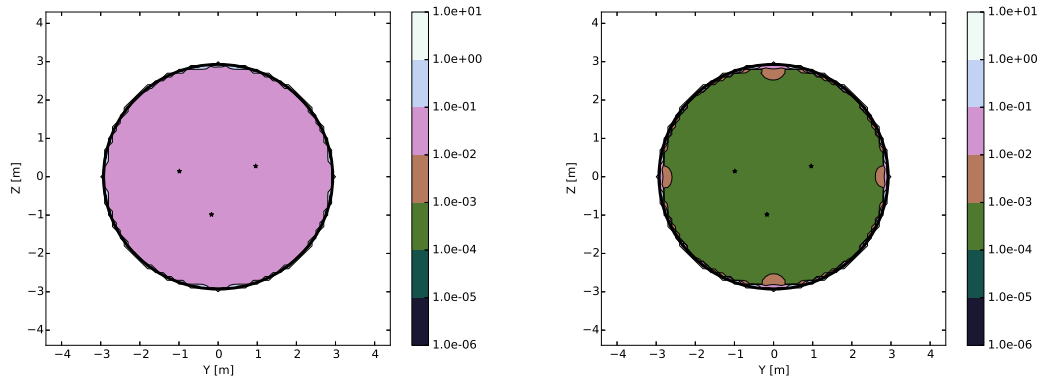
(a) 8 coil spherical system
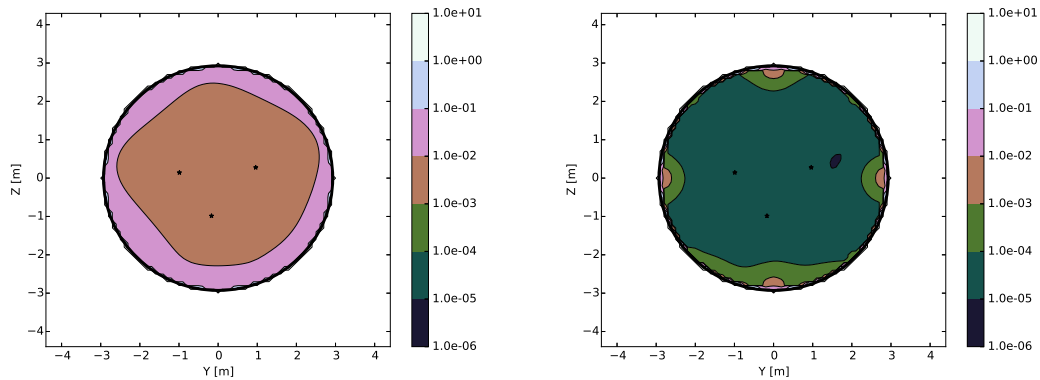


(b) 15 coils spherical system

Figure 4.43: Maps of simulated average $\Delta$ for spherical magnetic field compensation systems for disturbance sources located randomly 20 m away from the centre of system – left panel and 200 m – right panel. The map plane is at $x = 0.01$ m. The coil positions are marked with a black circle and position of two of the feedback sensors are marked with black stars.

These maps allow us to conclude that, for the spherical system, the magnetic field is fairly well compensated in almost an entire controlled volume. Adding the third order coils ($l = 3$) in the spherical systems still improves the shielding factor by almost an order of magnitude.

A more detailed discussion about simulated compensation performance of all considered systems is presented in Chapter 5.

# Chapter 5

# Simulation results

In the previous chapters, four magnetic field compensation systems were presented. They all work in a similar way: the magnetometers continuously sample the field and this information is then used for calculation of the reaction currents driven into the coils. The whole operation was simulated. In order to obtain comparable results, the systems were scaled to surround a similar volume. A view of the compared systems is shown in Fig. 5.1. For comparison, the sphere with $r = 1$ m is drawn inside the systems.

The first comparison of the systems was done with varying size of controlled volume $V_{exp}$. For all the systems except cellular, the position of simulated feedback sensors was chosen randomly from points laying on the surface of the control volume. The cellular system utilizes sensors in the centre of coils. Two different shapes of control volume are considered in this comparison - sphere (Figs. 5.2 and 5.3) and cube (Figs. 5.4 and 5.5). Two plots for each of the control volume shapes show relation for two different disturbance field source locations - more distant and closer to the system. In these plots, the averaged (over the controlled volume) $\Delta$ is plotted against the size of the controlled volume. All systems except cellular, show a distinct decrease of compensation performance with an increasing size of $V_{exp}$, thus decreasing distance from coils to the feedback field measurement point. Cellular coils show approximately constant shielding inside the whole volume. This is unique for these systems and this property is no longer valid when regularization is used for calculation of currents.

The lowest average $\Delta$, meaning lowest value of field after compensation, is obtained with the spherical coil system with 15 coils. Around 2 orders of magnitude worse is
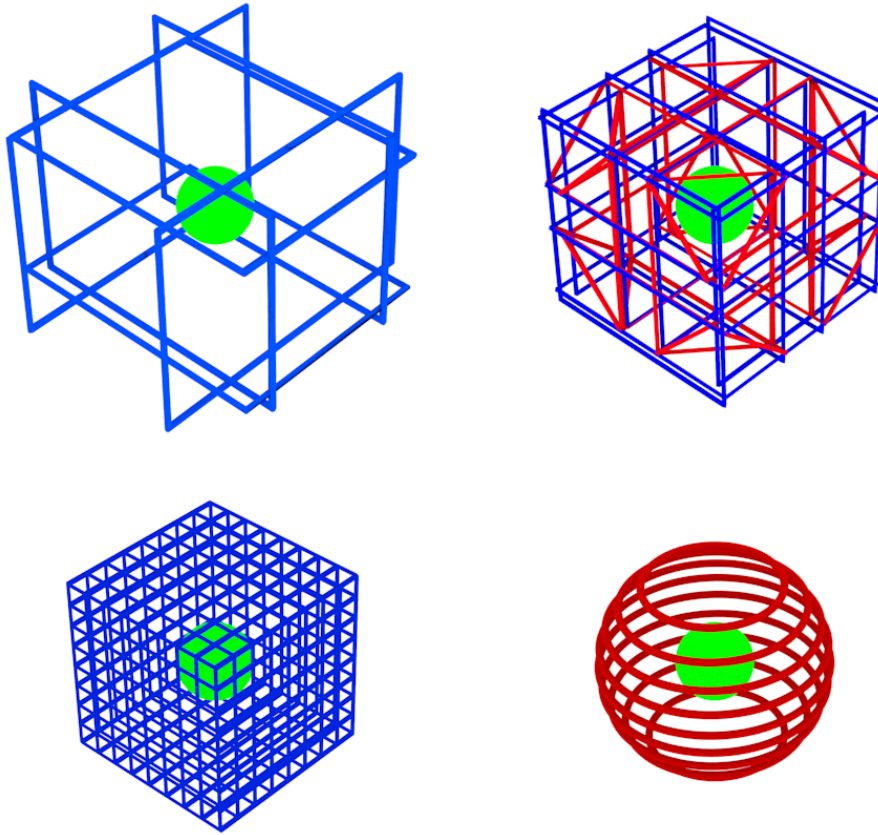
Figure 5.1: Three compensation systems used in the performance comparison - 6 rectangular coils of SFC, 24 coils of the Merritt setups (in blue 12 Merritt and in red additional 12 diagonal coils), 6x64 cellular coils and one example coil from the spherical system. For comparison, the spherical controlled volume with $r = 1$ m is drawn for all setups.

the system with 8 spherical coils and 24 modified Merritt coils. The result of a 24 rectangular coil system is a big improvement over the 12 Merritt coil system, which has a similar performance as the reference SFC setup. The only improvement over the 6 coil system is visible for big control volume sizes and source further away from system. This is a result of higher uniformity of the magnetic field, which is possible to obtain by Merritt coils, compared to Helmholtz-like setup of the SFC system.

Two considered cellular coil systems with regularized vector feedback show similar performance in simulations. It is the result of the big sensitivity of the system's performance to regularization parameter, which pays a bigger role than the number of coils in

the system.

The biggest advantage of the cellular coil systems is shown in the plot of relative spread of the $\Delta$ distribution inside the control volume (Fig. 5.6 for spherical control volume). The relative spread is defined as ratio of standard deviation of $\Delta$ distribution to average $\Delta$. Cellular coil systems with global scalar feedback exhibit 2-3 orders of magnitude lower values of this figure of merit, meaning much narrower $\Delta$ distribution than obtained with other systems.

Another way to compare the compensation system is to draw performance as a function of the disturbance field source's distance to the system - Fig. 5.7. For each of the points on this plot, 100 random positions and orientations of the sources at a given distance were used to get the most universal picture. To emphasize the theoretical limitations of the spherical coil system, in Fig. 5.8 the same relation for the 8 and 15 coil spherical systems is shown, marking a difference between coils consisting of 100 and 400 wires. The performance of the SFC and the cellular coil systems is almost independent on the distance from the disturbance source.

For spherical systems, the average $\Delta$ decays with distance to the source as $r^{-(l_{max})}$. The only deviation from this law can be observed for the 15 coil system. For big distances, the average $\Delta$ flattens. This effect can be attributed to errors introduced by using wire approximation instead of perfect continuous current distribution. Increasing the coil wire density (from 100 to 400 wires per coil) the lowest value of $\Delta$ gets 10 times smaller than before. For the 8 coil system, we do not see this effect because the error resulting from the cut-off of the vector spherical harmonic expansion is bigger than the one from the current discretization.

This gain in performance is not caused by increasing the number of degrees of freedom. Adding 6 new coils, resulting in a Merritt 12 coil system, does not improve the performance significantly, as can be seen on all of the plots. We have found the only noticeable improvement in larger sizes of controlled volume, where improved uniformity of the field created by the 12-coil system matters.

Table 5.1: Meaning of symbols used in graphs

| | |
|---|---|
| ◇ | 6 SFC coils |
| ⊙ | 8 Spherical coils |
| ● | 15 Spherical coils |
| ■ | 12 Merritt coils |
| ⊡ | 24 Modified Merritt coils |
| △ | 6x9 Cellular coils with global scalar feedback |
| ▲ | 6x64 Cellular coils with global scalar feedback |
| ▽ | 6x9 Cellular coils with regularized global vector feedback |
| ▼ | 6x64 Cellular coils with regularized global vector feedback |
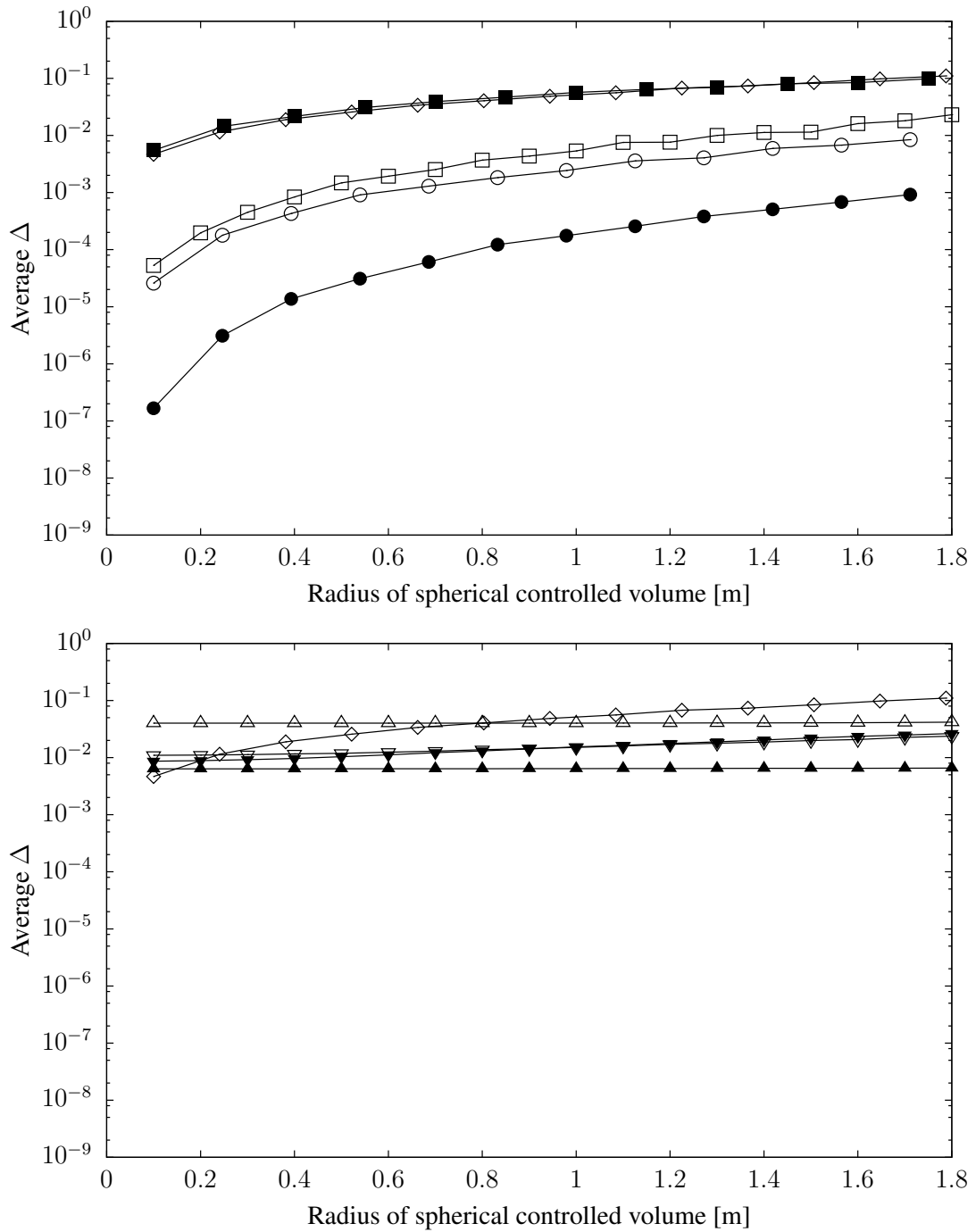
Figure 5.2: Average $\Delta$ as a function of the size of the spherical control volume with feedback sensors located on that surface for the disturbance field source located at $(10, 15, 20)$ m. Lines are to guide the eye.
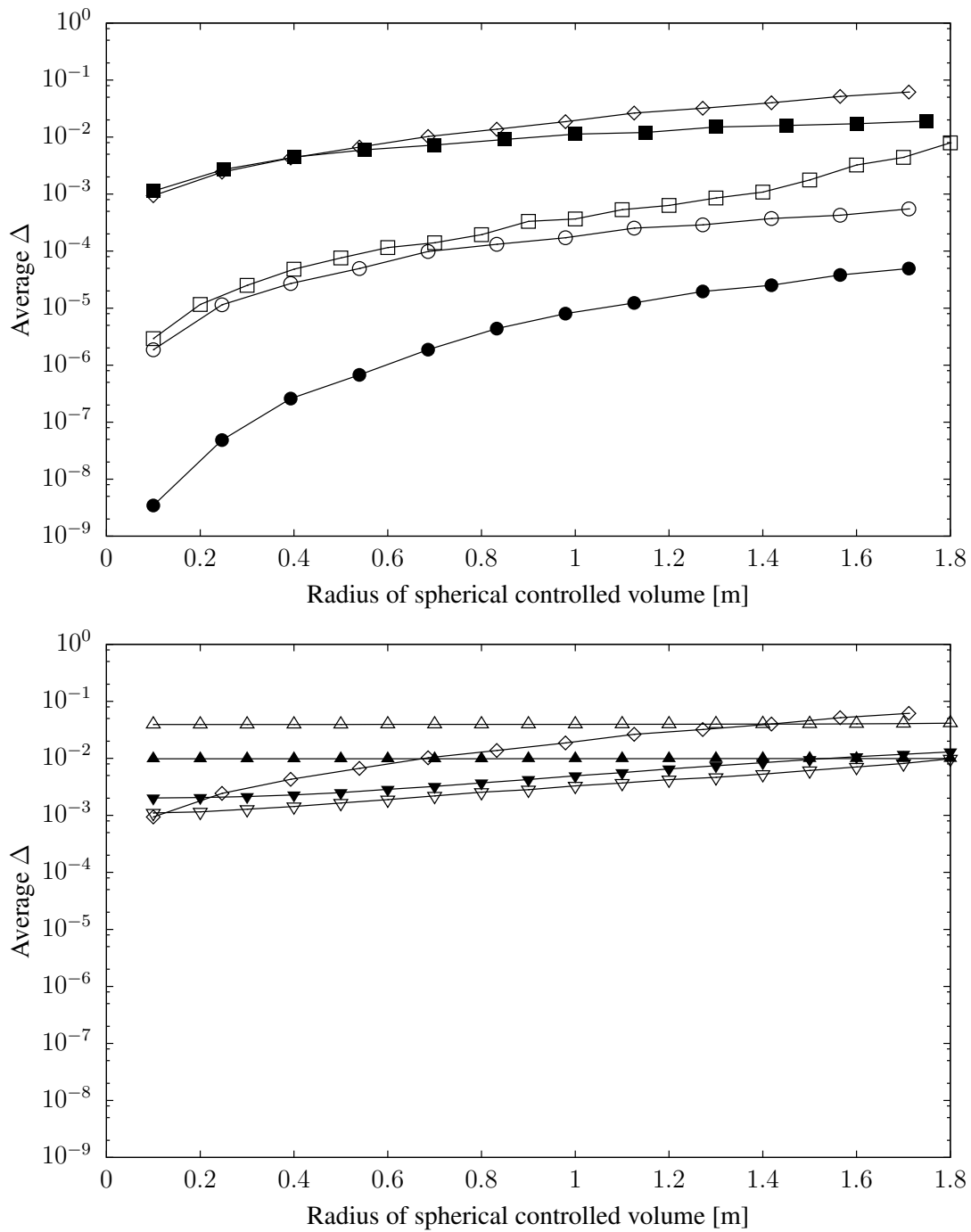
Figure 5.3: Same as Fig. 5.2 but for the disturbance field generated by the current loop located at $(50, 70, 60)$ m.
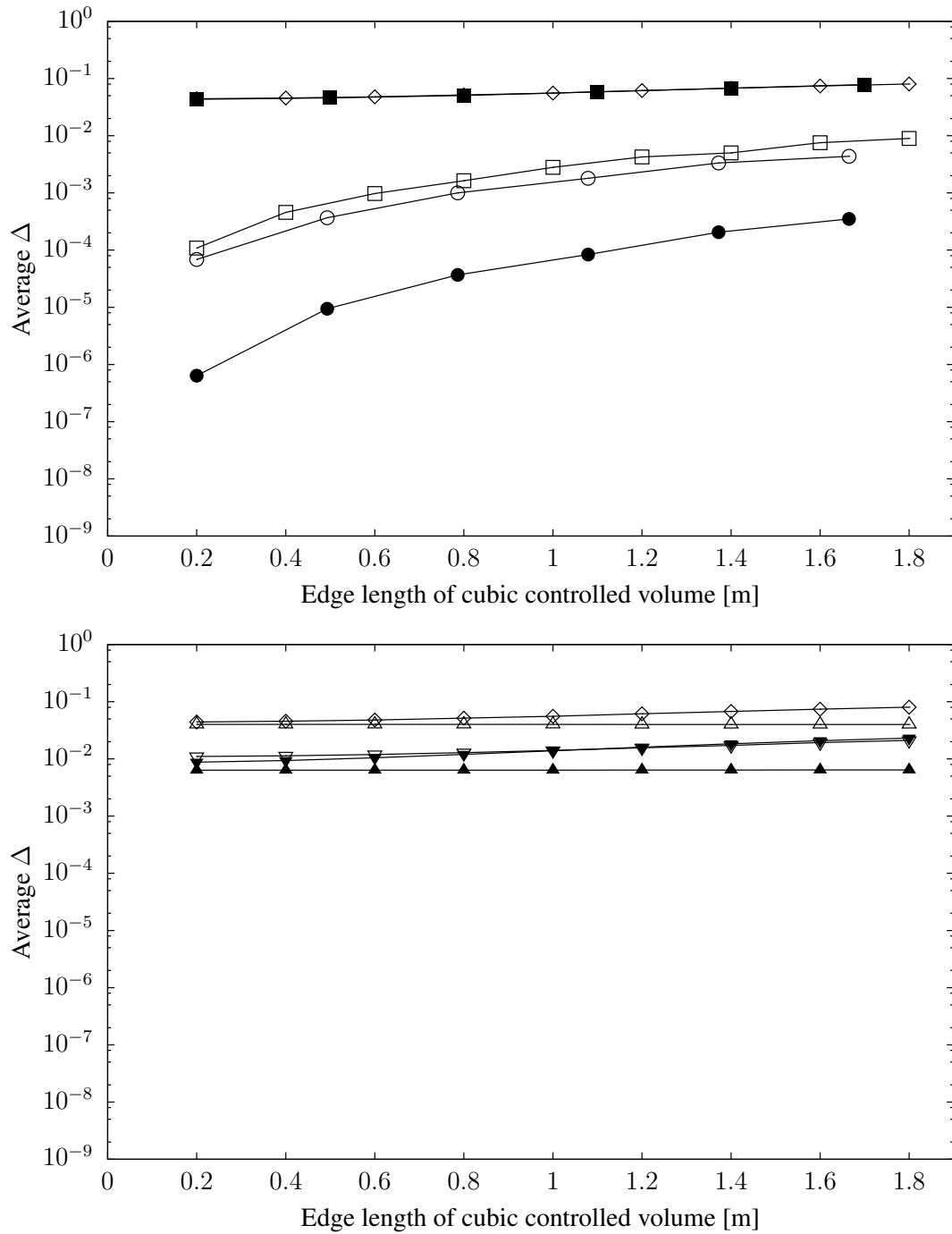
Figure 5.4: Same as Fig. 5.2, but for cubic controlled volume and disturbance field generated by current loop located at $(10, 15, 20)$ m.
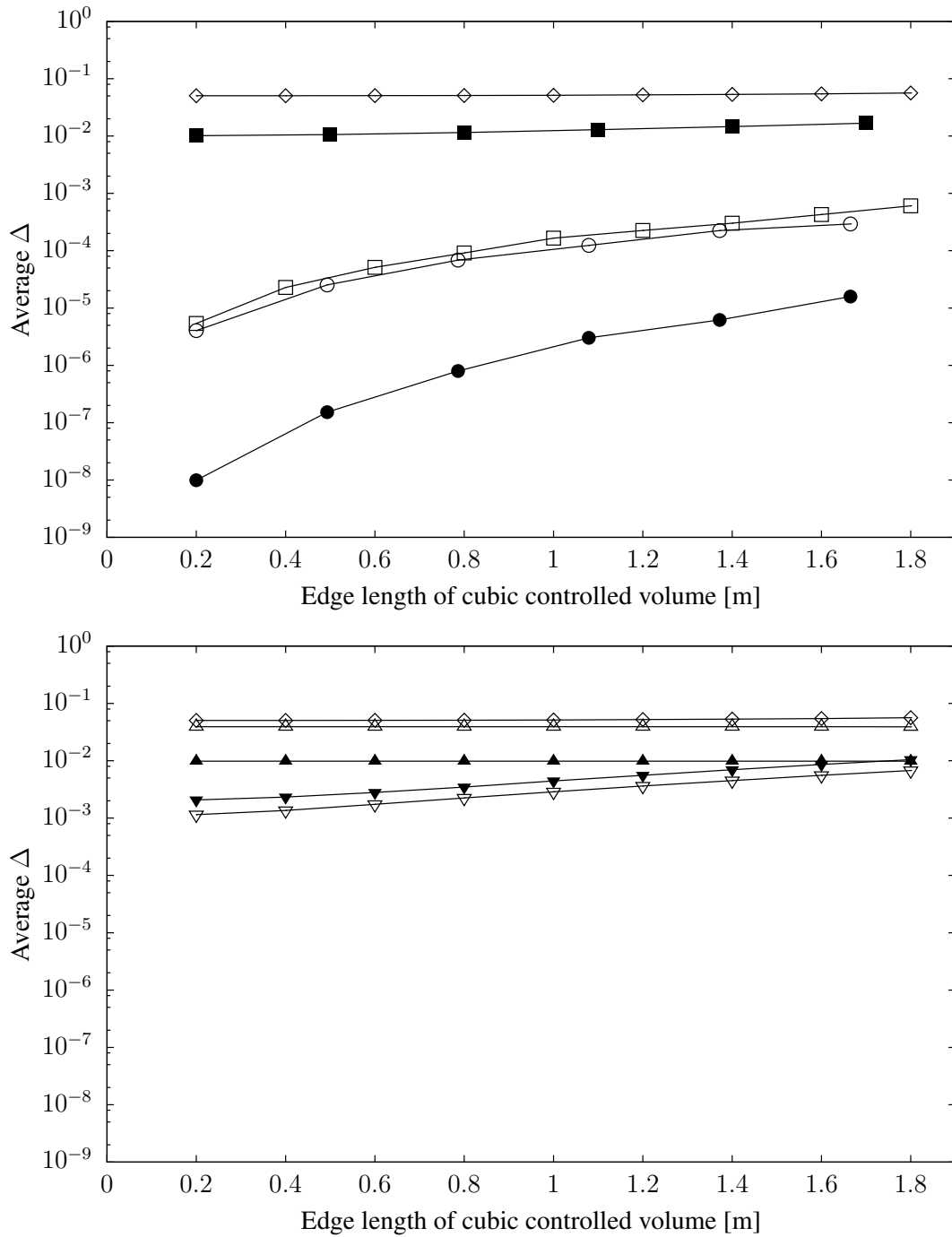
Figure 5.5: Same as Fig. 5.2, but for cubic controlled volume and disturbance field generated by current loop located at $(50, 70, 60)$ m.
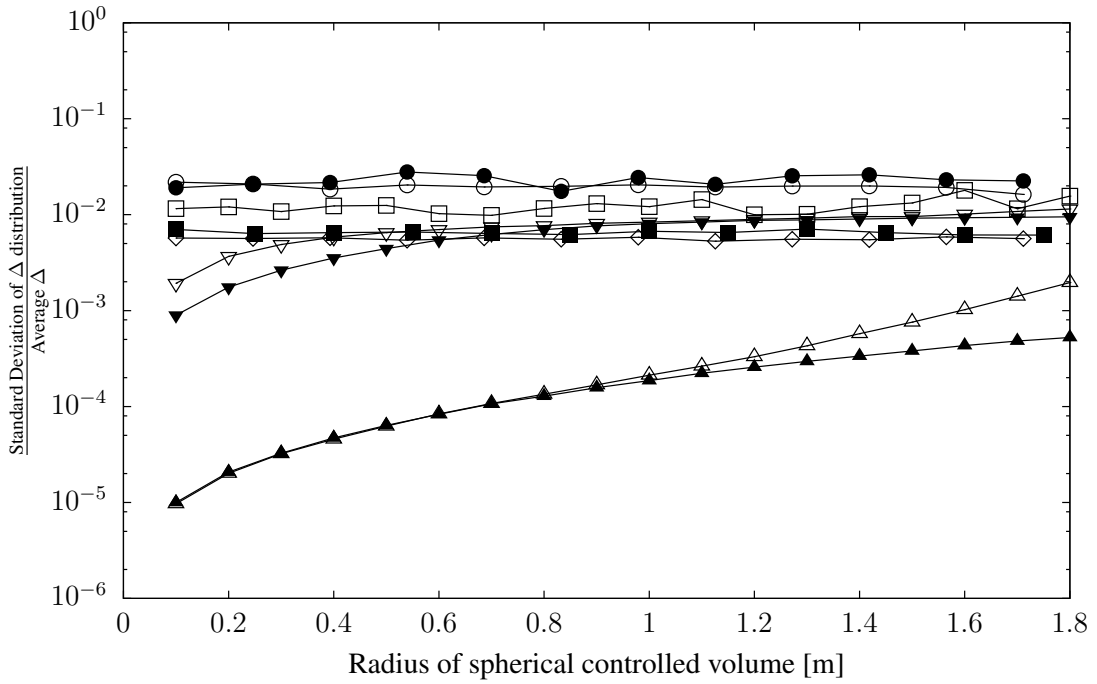
(a) Disturbance source located at $(50, 70, 60)$ m.
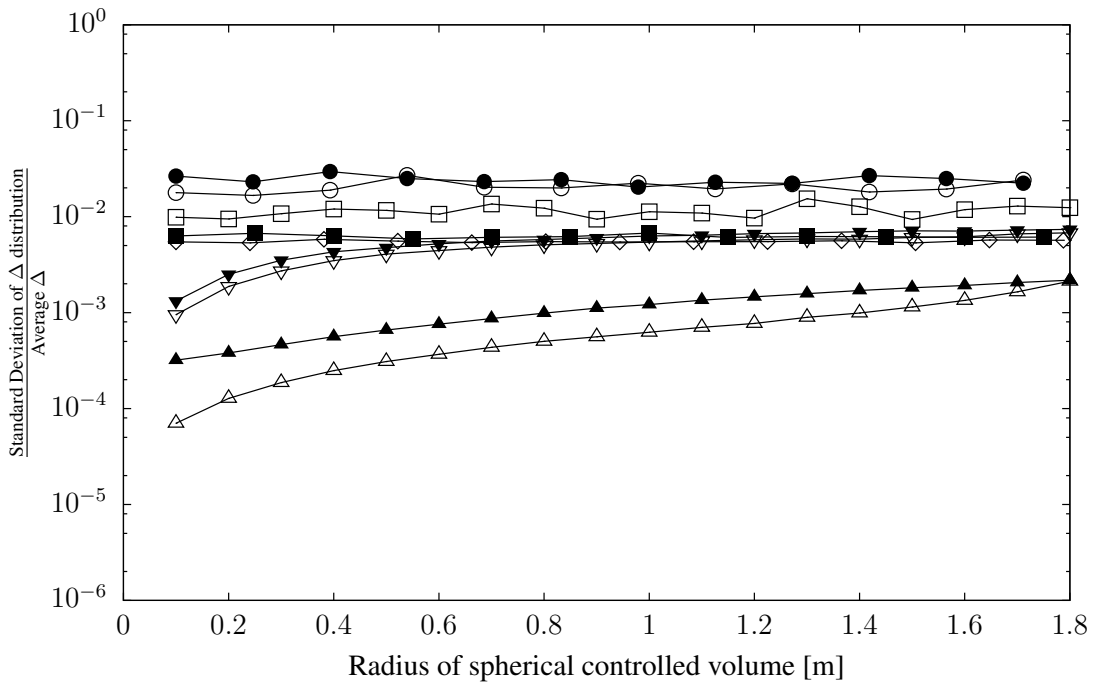


(b) Disturbance source located at $(10, 15, 20)$ m.

Figure 5.6: Relative spread of $\Delta$ distribution divided by average $\Delta$ as a function of the size of the spherical control volume. Lines are to guide the eye
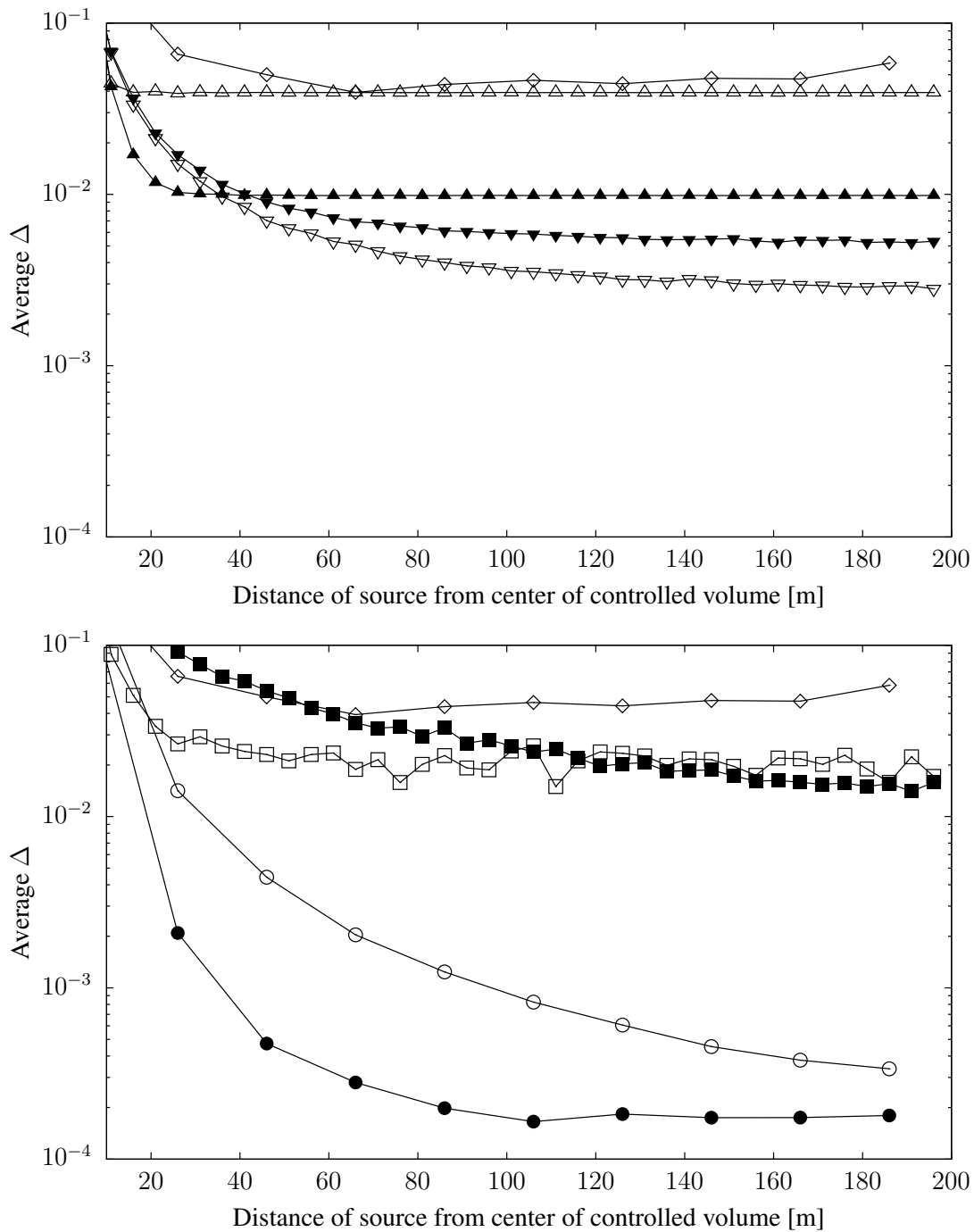
Figure 5.7: Average $\Delta$ as a function of the distance to the source of the disturbance of magnetic field. Lines are to guide the eye.
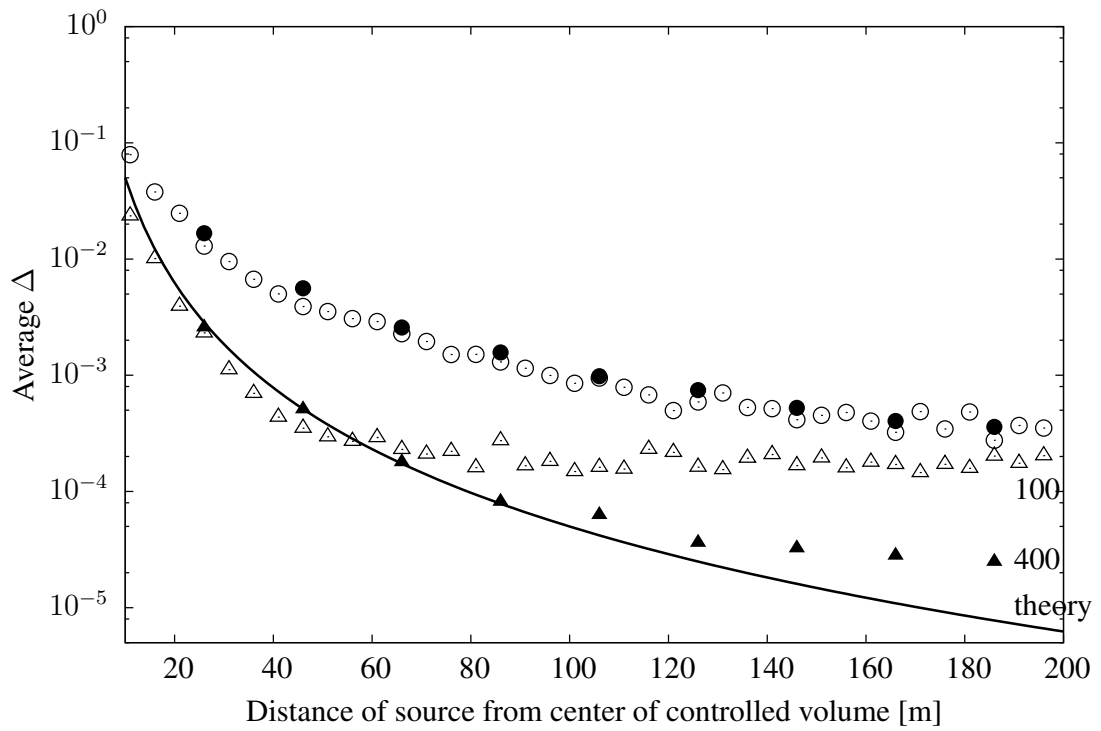
Figure 5.8: Average $\Delta$ in function of the distance of disturbance field (spherical control volume) for spherical coil systems. $\bigcirc$ mark the 8-coil spherical system, $\triangle$ – 15 coil. Empty symbols denote less dense coils (100 windings), while full ones correspond to 400 windings. The solid line marks the theoretical relation for the 15 coil system: $\Delta \propto r^{-3}$

The magnetic field compensation systems described in this part cover a broad spectrum of possibilities. Simple rectangular coil systems are the easiest to build, but the performance is modest as compared to e.g. spherical systems.

The modified Merritt system, built and tested, is the easiest improvement over the 6 coil SFC system. Its test operation, due to technical imperfections of current sources and readout system, was not optimal, thus obtained results were worse than the original SFC system. The most significant improvement of the test setup would be using of better current sources and replacing the analogue filter with the digital one. This should eliminate the ghosting effect.

Although, basing on the simulation results, the performance improvement would be visible only for perturbations of magnetic field located far away from the system. To improve the operation of this compensation system also against closer located magnetic field disturbances, one should consider adding additional 12 coils. This change makes the performance of the rectangular coil system comparable to the spherical system with 8 coils.

Spherical coil systems are the solutions with the best performance. The gain may be significant - $\Delta$ around $10^{-3}$ corresponds to the shielding factor of $1000$, comparable to the performance of two-layer passive shields [70]. The drawbacks are purely of technical nature - building the coil system by covering a full sphere, makes it very hard to access the controlled volume.

Interesting solutions are "cellular" coil systems. They show unique features, like the uniformity of shielding factor inside the system and independence of the shielding performance on the distance to the perturbation source. They are also relatively easy to build, thus may be an optimal option in many applications.

# Part III

# Magnetic field mapping

# Chapter 6

# Magnetic field mapping analysis

## 6.1  Introduction

Magnetic field gradients are the source of the biggest systematic uncertainties in measurement of the neutron electric dipole moment. In the nEDM experiment at PSI, besides the main coil, additional 33 coils are used in order to reduce the field gradients. In order to properly tune the trim coils, one should know the gradients' distribution. For this, measurement accuracy of one nT is crucial. To achieve that, it is necessary to take into account not only the sensor accuracy, but also imperfections of mechanical construction of the mapping device. This part of the dissertation is dedicated to the description and dealing with imperfection of the magnetic field mapping measurement.

The magnetic field mapping device was designed and built by workshops in the Laboratoire de Physique Corpusculaire de CAEN and is shown in Fig. 6.1. Its construction allows the use of both the fluxgate magnetometer and the vector caesium magnetometer. In this work, I will focus on the analysis of data taken by the fluxgate magnetometer.

## 6.2  The mapper

Basing on experience with previous mapping devices, this mapper is built completely from non-metallic parts. It consists of a rotating and vertically moving shaft, mounted to the aluminium vacuum chamber of the nEDM spectrometer with two bearings. A horizontal mapper arm is fixed to this shaft, holding a radially moving carrier with a

Figure 6.1: Mapping device located inside the vacuum tank.

magnetic field sensor. The rotation angle, height of arm and radial position of carrier are measured by reading out voltage drop on potentiometers connected to the mechanical parts by non-elastic threads.

The sensor is mounted inside a tube with a helix, used for rotating the fluxgate $180°$ around a radial axis, what is necessary for correcting the so-called reading offset.

Because of the construction of the mapper, the cylindrical system of coordinates is natural for the description of the field. Both measurements (field and position) are obtained in this system. Because the magnetic field is to be decomposed to the Cartesian harmonics (see Appendix A), it is necessary to transform this readings to the Cartesian coordinate system.

The change of the measurement position is performed by rotating the arm and then changing the position of the carrier. This results in data taken along circles of constant $r$ and $z$ coordinates. Measurements are performed with the mapper at rest.

## 6.3 Imperfections of the field mapper

Having in mind the requirement for the magnetic field uniformity and stability, it is mandatory to consider imperfections of the mapper itself and of the mapping procedure. They must be included in the analysis of maps and estimation of the resulting uncertainties. Some of those effects can be determined from an independent calibration

measurement. Others are not directly accessible, but influence the measured value in a systematic way and can be included in the analysis in a form of a model. Thus, the general fit of the model to the set of measured values may deliver both the field expansion coefficients and the imperfection parameters of the mapping procedure.

Real directions of measurement, marked as $\tilde{X}, \tilde{Y}, \tilde{Z}$, are related to orthogonal directions $\hat{X} = -\hat{\varphi}, \hat{Y} = -\hat{z}, \hat{Z} = \hat{r}$ via seven angular parameters and three offset values, describing the imperfections of the measurement device. These parameters can be divided into two such sets:

1. Sensor related:

   - Offsets - fluxgate sensors have internal offsets, which cause the readout value to be shifted by a constant, that does not change within a few subsequent readings. However, this imperfection may drift in time and there is a dedicated measurement needed for the offset value before and after each map measurement. There are 3 offset values to determine, one for each of the 3d sensor directions.

   - Non-orthogonality - it is related to the fact that 3 sensors creating one 3d fluxgate magnetometer are not aligned with an exact right angle. 5 independent angles marked with capital letters such as $A, B, C, D, E$, are used to describe the real sensor orientation $\tilde{X}, \tilde{Y}, \tilde{Z}$ with respect to the set of orthogonal directions, $X', Y', Z'$ (see Fig. 6.2). According to the specification [71], relative non-orthogonality of the Stefan Mayer FLC3-70 fluxgate sensors shall be smaller than $0.1°$.

2. Mapper related - Two angles, $\alpha$ - pitch and $\beta$ - roll, describe the rotation relation between orthogonal directions $X', Y', Z'$ and vectors describing directions in the cylindrical set of coordinates $- \hat{X} = -\hat{\varphi}, \hat{Y} = -\hat{z}, \hat{Z} = \hat{r}$ (see Fig. 6.2).

We assume that only offsets change with time. Other parameters are determined once for the whole measurement campaign. For determination of the offset values dedicated evaluation is performed before and after every field measurement.

A three dimensional fluxgate magnetometer consists physically of 3 separate sensors joined together inside one housing. This means that besides the non-orthogonality

angles, one also has to take into account the fact that 3 sensors measure the magnetic field in 3 separate places, 20 mm apart.
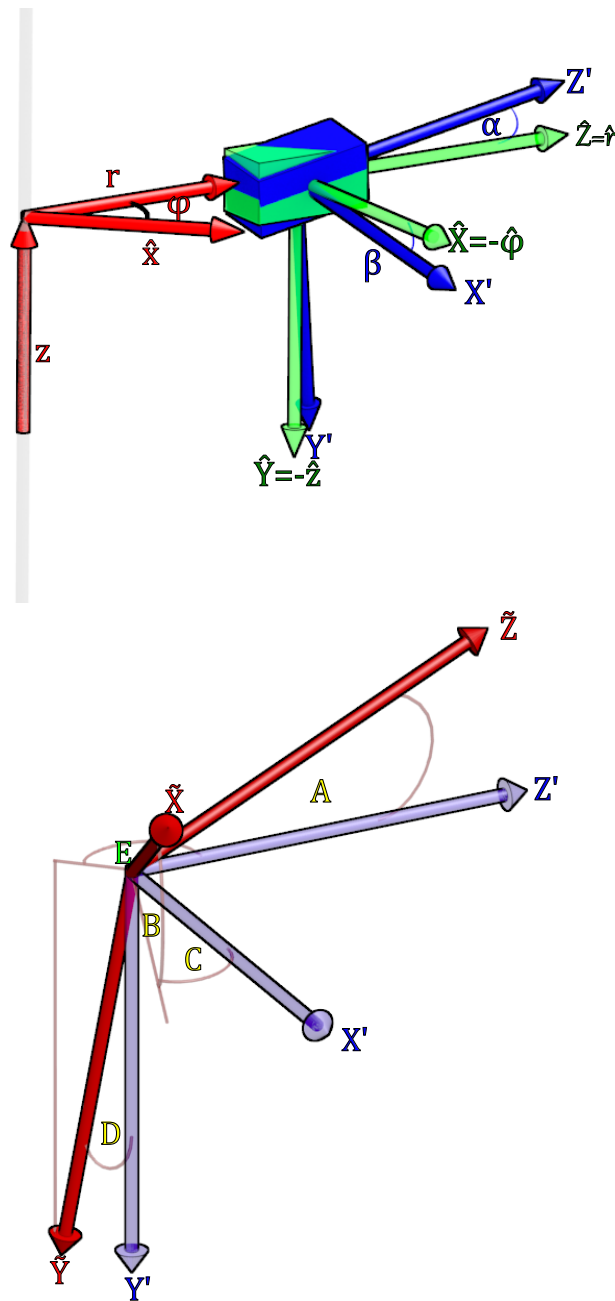
Figure 6.2: Real measurement axes - $\tilde{X}, \tilde{Y}, \tilde{Z}$ and their relation to ideal measurement axes $\hat{X} = -\hat{\varphi}, \hat{Y} = -\hat{z}, \hat{Z} = \hat{r}$

## 6.3.1 Offsets and non-orthogonalities

When measuring the magnetic field at angle $\varphi$, the measured field is described by:

$$\begin{pmatrix} \tilde{B}_X \\ \tilde{B}_Y \\ \tilde{B}_Z \end{pmatrix} = \begin{pmatrix} (R_z(\varphi)\tilde{X}) \cdot \vec{B} + x_{offset} \\ (R_z(\varphi)\tilde{Y}) \cdot \vec{B} + y_{offset} \\ (R_z(\varphi)\tilde{Z}) \cdot \vec{B} + z_{offset} \end{pmatrix}, \tag{6.1}$$

where $R_z(\varphi)$ is the rotation matrix with angle $\varphi$ around Z axis, $x_{offset}, y_{offset}, z_{offset}$ are three offset values and $\tilde{X}, \tilde{Y}, \tilde{Z}$ are three non-orthogonal axes, defined as:

- $\tilde{X}$ is a $X' = -\hat{\varphi}$ direction rotated around the $Y'$ axis by angle $C$ and then rotated by angle $B$ around $Z'$ axis.

- $\tilde{Y}$ is a $Y' = -\hat{z}$ direction rotated around the $Z'$ axis by angle $D$ and then rotated by angle $E$ around $Y'$ axis.

- $\tilde{Z}$ is a $Z' = \hat{r}$ direction rotated around the $Y'$ axis by angle $A$

In this way each of the sensor's directions can be described by:

$$\tilde{X} = \begin{pmatrix} 1 & 0 & 0 \\ 0 & \cos(B) & -\sin(B) \\ 0 & \sin(B) & \cos(B) \end{pmatrix} \begin{pmatrix} \cos(C) & -\sin(C) & 0 \\ \sin(C) & \cos(C) & 0 \\ 0 & 0 & 1 \end{pmatrix} \begin{pmatrix} 0 \\ -1 \\ 0 \end{pmatrix}, \tag{6.2}$$

$$\tilde{Y} = \begin{pmatrix} \cos(E) & -\sin(E) & 0 \\ \sin(E) & \cos(E) & 0 \\ 0 & 0 & 1 \end{pmatrix} \begin{pmatrix} 1 & 0 & 0 \\ 0 & \cos(D) & -\sin(D) \\ 0 & \sin(D) & \cos(D) \end{pmatrix} \begin{pmatrix} 0 \\ 0 \\ -1 \end{pmatrix}, \tag{6.3}$$

$$\tilde{Z} = \begin{pmatrix} \cos(A) & 0 & \sin(A) \\ 0 & 1 & 0 \\ -\sin(A) & 0 & \cos(A) \end{pmatrix} \begin{pmatrix} 1 \\ 0 \\ 0 \end{pmatrix}, \tag{6.4}$$

in basis $(\hat{r}, \hat{\varphi}, \hat{z})$. To correct for non-orthogonalities, the inverse of Eq. (6.1) has to be applied, solving for $\vec{B}$, resulting in cylindrical coordinates of the field, $(B'_r, B'_\varphi, B'_Z)$.

### 6.3.2   Misalignments

Misalignment angles result from imperfections of the mechanical design of the mapper. In this model, they are described by two angles, $\alpha$ - roll, which is related to plasticity leading to the arm bending, and $\beta$ - pitch, which is related to the shape of the surface on which the carrier is moving. These angles are functions of the $z, r$ global position coordinates in the cylindrical system.

Assuming $B_r, B_\varphi, B_z$ to be the cylindrical coordinates of the magnetic field (after correction for non-orthogonalities), misalignments would result in the following rotation of measured field:

$$\begin{pmatrix} \hat{B}_r \\ \hat{B}_\varphi \\ \hat{B}_z \end{pmatrix} = R_\varphi(\beta) R_r(\alpha) \begin{pmatrix} B'_r \\ B'_\varphi \\ B'_z \end{pmatrix}, \qquad (6.5)$$

where $R_\varphi(\beta)$ - rotation matrix around the $\hat{\varphi}$ axis by pitch angle $\beta$, $R_r(\alpha)$ - a rotation matrix around the $\hat{r}$ axis by roll angle $\alpha$. To correct for these misalignments, one needs to apply:

$$\vec{B}_{corrected} = R_r(-\alpha) R_\phi(-\beta) \vec{B}_{notcorrected}. \qquad (6.6)$$

## 6.4   Determination of imperfection parameters

### 6.4.1   Offsets and non-orthogonality angles

Offsets are drifting in time, which make it necessary to have dedicated measurement before and after each map. This, so-called "calibration run", consists of the following steps:

1. Positioning one of the axes of fluxgate magnetometer exactly on the axis of rotation of the mapper,

2. Measuring the magnetic field with the mapper rotated every $\varphi = 10°$,

3. Repeating the measurement for 2 other sensors,

4. Flipping the fluxgate by $180°$ around the $\hat{r}$ axis,

5. Measuring the magnetic field with the mapper rotated every $\varphi = 10°$,

6. Repeating the measurement for 2 other sensors.

Description of a field measurement by an imperfect sensor measure field is expressed in Eq. (6.1). One can parametrize the magnetic field at the point $(0, 0, 0)$ as:

$$\vec{B} = \begin{pmatrix} B_t \cos(\theta) \\ B_t \sin(\theta) \\ B_3 \end{pmatrix}. \tag{6.7}$$

After taking only first order terms in the Taylor expansion in small quantities for angles $A, B, D$, the expression for measured field simplifies to:

$$
\vec{B}_{1,meas} = \begin{pmatrix} B_t \sin(C) \cos(\theta) - B_t \cos(C) \sin(\theta) \\ B_t D \cos(E) \sin(\theta) - B_t D \sin(E) \cos(\theta) \\ B_t \cos(\theta) \end{pmatrix} \cos(\varphi) +
$$

$$
+ \begin{pmatrix} B_t \sin(C) \sin(\theta) + B_t \cos(C) \cos(\theta) \\ -B_t D \sin(E) \sin(\theta) - B_t D \cos(E) \cos(\theta) \\ B_t \sin(\theta) \end{pmatrix} \sin(\varphi) +
$$

$$
+ \begin{pmatrix} x_{offset} - B_3 B \cos(C) + O\left(B^2\right) \\ (y_{offset} - B_3) + O\left(D^2\right) \\ z_{offset} - AB_3 + O\left(A^2\right) \end{pmatrix} =
$$

$$
= \begin{pmatrix} A_{1cosx} \\ A_{1cosy} \\ A_{1cosz} \end{pmatrix} \cos(\varphi) + \begin{pmatrix} A_{1sinx} \\ A_{1siny} \\ A_{1sinz} \end{pmatrix} \sin(\varphi) + \begin{pmatrix} A_{1cx} \\ A_{1cy} \\ A_{1cz} \end{pmatrix}. \tag{6.8}
$$

Magnetic field seen by the flipped sensor positioned in the same point as in Eq. (6.8) can be expressed as:

$$
\vec{B}_{2,meas} = \begin{pmatrix} B_t \sin(C) \cos(\theta) + B_t \cos(C) \sin(\theta) \\ -B_t D \sin(E) \cos(\theta) - B_t D \cos(E) \sin(\theta) \\ B_t \cos(\theta) \end{pmatrix} \cos(\varphi) +
$$

$$+ \begin{pmatrix} B_t \sin(C) \sin(\theta) - B_t \cos(C) \cos(\theta) \\ B_t D \cos(E) \cos(\theta) - B_t D \sin(E) \sin(\theta) \\ B_t \sin(\theta) \end{pmatrix} \sin(\varphi) +$$

$$+ \begin{pmatrix} x_{offset} + B_3 B \cos(C) + O\left(B^2\right) \\ (B_3 + y_{offset}) + O\left(D^2\right) \\ z_{offset} + AB_3 + O\left(A^2\right) \end{pmatrix} =$$

$$= \begin{pmatrix} A_{2cosx} \\ A_{2cosy} \\ A_{2cosz} \end{pmatrix} \cos(\varphi) + \begin{pmatrix} A_{2sinx} \\ A_{2siny} \\ A_{2sinz} \end{pmatrix} \sin(\varphi) + \begin{pmatrix} A_{2cx} \\ A_{2cy} \\ A_{2cz} \end{pmatrix}. \qquad (6.9)$$

The relation between angle and field seen by an imperfect sensor is shown in Fig. 6.3. The fitted trigonometric functions are marked with solid lines. Coefficients in brackets in Eqs. (6.8) and (6.9) can be extracted from measurements using the Fast Fourier Transform algorithm. From this, all needed angles and offset values can be calculated:

$$\tan \theta = \frac{A_{1sinz} + A_{2sinz}}{A_{1cosz} + A_{2cosz}} \qquad (6.10)$$

$$A_t = \frac{1}{2} \left( \sqrt{A_{1cosx}^2 + A_{1sinx}^2} + \sqrt{A_{2cosx}^2 + A_{2sinx}^2} \right), \qquad (6.11)$$

$$\tan(C) = \frac{1}{2} \left( -\tan\theta \frac{A_{1cosx} + A_{2cosx}}{A_{1cosx} - A_{2cosx}} + \frac{1}{\tan\theta} \frac{A_{1sinx} + A_{2sinx}}{A_{1sinx} - A_{2sinx}} \right), \qquad (6.12)$$

$$\tan(E) = \frac{1}{2} \left( -\tan\theta \frac{A_{1cosy} + A_{2cosy}}{A_{1cosy} - A_{2cosy}} + \frac{1}{\tan\theta} \frac{A_{1siny} + A_{2siny}}{A_{1siny} - A_{2siny}} \right), \qquad (6.13)$$

$$A = -\frac{A_{1cz} - A_{2cz}}{2A_3}, \qquad (6.14)$$

$$B = -\frac{A_{1cx} - A_{2cx}}{2A_3 \cos(C)}, \qquad (6.15)$$

$$D = \frac{1}{4} \left( -\frac{A_{1cosy}}{A_t \sin(E-\theta)} - \frac{A_{2cosy}}{A_t \sin(E+\theta)} - \frac{A_{1siny}}{A_t \cos(E-\theta)} + \frac{A_{2siny}}{A_t \cos(E+\theta)} \right), \qquad (6.16)$$

$$x_{offset} = \frac{1}{2} \left( A_{1cx} + A_{2cx} \right), \qquad (6.17)$$

$$y_{offset} = \frac{1}{2} \left( A_{1cy} + A_{2cy} \right), \qquad (6.18)$$

$$z_{offset} = \frac{1}{2} \left( A_{1cz} + A_{2cz} \right). \qquad (6.19)$$

Equations (6.17) - (6.19) are used for determination of the offset values from each of the calibration runs.



(a) X sensor
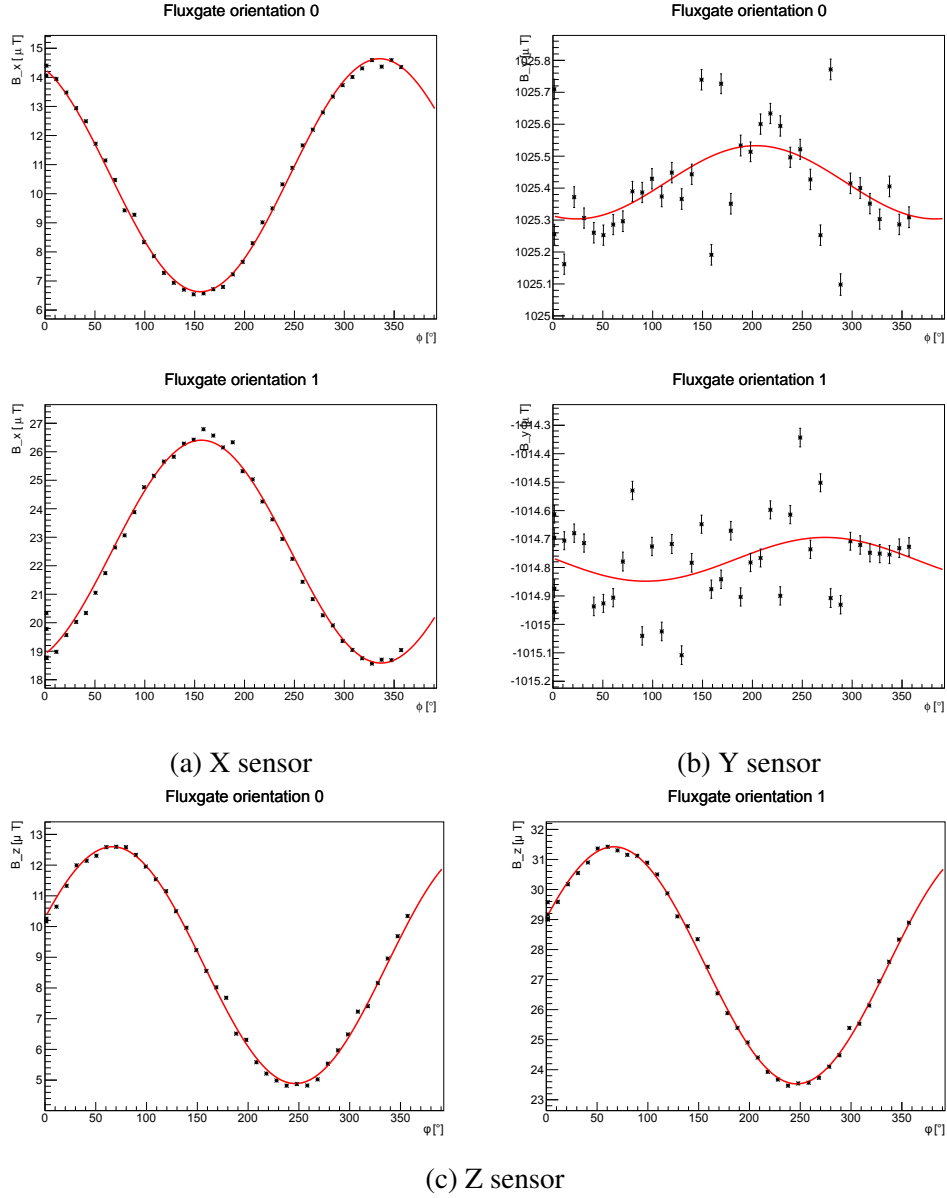
(b) Y sensor

(c) Z sensor

Figure 6.3: The magnetic field measured during calibration runs as a function of angle $\varphi$. Orientation 0 corresponds to the $X$ sensor in the $\hat{\varphi}$ direction, orientation 1 is rotated by $\pi$ around the $\hat{r}$ direction. This measurements are not corrected for any imperfections. Solid lines correspond to the result of the FFT fitting (for details see text).

### 6.4.2 Misalignments

To determine the misalignment angles $\alpha$ and $\beta$ two assumptions are needed:

1. These two angles change only while changing the radius - for each measurement cycle at constant $r, z$ (cylindrical coordinates) they stay constant.

2. The magnetic field for each measurement cycle at constant $(r, z)$ can be expressed as:

$$\vec{B} = \begin{pmatrix} B_x \\ B_y \\ B_z \end{pmatrix} + G_1 \begin{pmatrix} \sin(\varphi)R \\ \cos(\varphi)R \\ 0 \end{pmatrix} + G_2 \begin{pmatrix} 0 \\ Z \\ \sin(\varphi)R \end{pmatrix} +$$

$$+ G_3 \begin{pmatrix} -2\cos(\varphi)R \\ -2\sin(\varphi)R \\ 4Z \end{pmatrix} + G_4 \begin{pmatrix} Z \\ 0 \\ \cos(\varphi)R \end{pmatrix} + G_5 \begin{pmatrix} -2\cos(\varphi)R \\ -2\sin(\varphi)R \\ 0 \end{pmatrix},$$

$$(6.20)$$

where $(B_x, B_y, B_z)$ describe an uniform component of magnetic field in Cartesian coordinates while $G_1$ to $G_5$ describe 5 independent first order gradients in Cartesian coordinates $(x, y, z)$ expressed as a function of angle $\varphi$ in cylindrical coordinates. This assumptions mean that we neglect other components of the field.

With this two assumptions we can calculate the real value as a function of the cylindrical angle $\varphi$:

$$\begin{pmatrix} B'_r \\ B'_\varphi \\ B'_z \end{pmatrix} = R_\varphi(\beta)R_r(\alpha) \begin{pmatrix} \cos(\varphi) & \sin(\varphi) & 0 \\ -\sin(\varphi) & \cos(\varphi) & 0 \\ 0 & 0 & 1 \end{pmatrix} \vec{B} =$$

$$\begin{pmatrix} (B_z + 4G_3Z)\sin(\beta) \\ (B_z + 4G_3Z)\cos(\beta)\sin(\alpha) \\ (B_z + 4G_3Z)\cos(\alpha)\cos(\beta) \end{pmatrix} +$$

$$+ \sin(\varphi) \begin{pmatrix} -B_y\cos(\beta) - G_2Z\cos(\beta) + G_2R\sin(\beta) \\ B_x\cos(\alpha) + G_4Z\cos(\alpha) + G_2R\cos(\beta)\sin(\alpha) + B_y\sin(\alpha)\sin(\beta) + G_2Z\sin(\alpha)\sin(\beta) \\ G_2R\cos(\alpha)\cos(\beta) - B_x\sin(\alpha) - G_4Z\sin(\alpha) + B_y\cos(\alpha)\sin(\beta) + G_2Z\cos(\alpha)\sin(\beta) \end{pmatrix} +$$

$$+ \cos(\varphi) \begin{pmatrix} B_x \cos(\beta) + G_4 Z \cos(\beta) + G_4 R \sin(\beta) \\ B_y \cos(\alpha) + G_2 Z \cos(\alpha) + G_4 R \cos(\beta) \sin(\alpha) - B_x \sin(\alpha) \sin(\beta) - G_4 Z \sin(\alpha) \sin(\beta) \\ G_4 R \cos(\alpha) \cos(\beta) - B_y \sin(\alpha) - G_2 Z \sin(\alpha) - B_x \cos(\alpha) \sin(\beta) - G_4 Z \cos(\alpha) \sin(\beta) \end{pmatrix} +$$

$$+ \sin(2\varphi) \begin{pmatrix} 2G_3 R \cos(\beta) + 2G_5 R \cos(\beta) \\ G_1 R \cos(\alpha) - 2G_3 R \sin(\alpha) \sin(\beta) - 2G_5 R \sin(\alpha) \sin(\beta) \\ -G_1 R \sin(\alpha) - 2G_3 R \cos(\alpha) \sin(\beta) - 2G_5 R \cos(\alpha) \sin(\beta) \end{pmatrix} +$$

$$+ \cos(2\varphi) \begin{pmatrix} 2G_5 R \cos(\beta) - 2G_3 R \cos(\beta) \\ G_1 R \cos(\alpha) + 2G_3 R \sin(\alpha) \sin(\beta) - 2G_5 R \sin(\alpha) \sin(\beta) \\ -G_1 R \sin(\alpha) + 2G_3 R \cos(\alpha) \sin(\beta) - 2G_5 R \cos(\alpha) \sin(\beta) \end{pmatrix} \equiv \qquad (6.21)$$

$$\equiv \begin{pmatrix} A_{fr} \\ A_{f\varphi} \\ A_{fz} \end{pmatrix} + \sin(\varphi) \begin{pmatrix} A_{sr} \\ A_{s\varphi} \\ A_{sz} \end{pmatrix} + \cos(\varphi) \begin{pmatrix} A_{cr} \\ A_{c\varphi} \\ A_{cz} \end{pmatrix} + \sin(2\varphi) \begin{pmatrix} A_{s2r} \\ A_{s2\varphi} \\ A_{s2z} \end{pmatrix} + \cos(2\varphi) \begin{pmatrix} A_{c2r} \\ A_{c2\varphi} \\ A_{c2z} \end{pmatrix},$$

$$(6.22)$$

where $R_\phi(\beta)$ is the rotation matrix around the basis vector by angle $\beta$, $R_r(\alpha)$ is the rotation matrix around the first basis vector by angle $\alpha$, $\varphi$ is the angular position of the sensor and $A_{fi}$, $A_{si}$, $A_{ci}$, $A_{s2i}$ and $A_{c2i}$ for $i \in \{r, \varphi, z\}$ are coefficients of the Fourier series describing the field as a function of measurement angle $\varphi$. Using the Fast Fourier Transform algorithm we obtain from measurement data the experimental values of those coefficients, denoted by $B_{fi}$, $B_{si}$, $B_{ci}$, $B_{s2i}$ and $B_{c2i}$ for $i \in \{r, \varphi, z\}$, respectively. To get misalignment angles, we minimize the chi-square function:

$$\chi^2 = \sum_{i \in \{f,s,c,s2,c2\}} \sum_{j \in \{r, \varphi. z\}} (A_{ij} - B_{ij})^2, \qquad (6.23)$$

using for example GSL [50] multidimensional minimization functions, resulting in estimation of angles $\alpha$ and $\beta$ as a function of distance from rotation axis $r$ and height $z$.

## 6.5 Fit of the expansion coefficients and estimation of their uncertainties

A measurement run is performed using the mapping device for a set of points. This set may change from measurement to measurement, making a direct (point-to-point) comparison impossible. Instead, we expand the measured field maps in Cartesian harmonics

defined in Tab. A.1 and compare the expansion coefficients. We can then express the magnetic field in whole volume as a set of components $h_i$:

$$\vec{B}(x, y, z) = \sum_{i=1}^{48} h_i \mathcal{H}_i(x, y, z), \tag{6.24}$$

where $\vec{B}(x, y, z)$ is the magnetic field induction at each point inside the precession volume and $\mathcal{H}_i(x, y, z)$ is Cartesian Harmonic (see Tab. A.1). To obtain the decomposition coefficients $h_i$, we have to solve the following set of equations:

$$B_x(x_1, y_1, z_1) = \sum_{i=1}^{48} h_i \mathcal{H}_{x,i}(x_1, y_1, z_1)$$

$$B_y(x_1, y_1, z_1) = \sum_{i=1}^{48} h_i \mathcal{H}_{y,i}(x_1, y_1, z_1)$$

$$B_z(x_1, y_1, z_1) = \sum_{i=1}^{48} h_i \mathcal{H}_{z,i}(x_1, y_1, z_1)$$

$$B_x(x_2, y_2, z_2) = \sum_{i=1}^{48} h_i \mathcal{H}_{x,i}(x_2, y_2, z_2)$$

$$\dots$$

$$B_z(x_N, y_N, z_N) = \sum_{i=1}^{48} h_i \mathcal{H}_{z,i}(x_N, y_N, z_N), \tag{6.25}$$

where $(x_1, y_1, z_1) \dots (x_N, y_N, z_N)$ are coordinates of measurement points. These equations can be written as a matrix equation:

$$\begin{pmatrix} B_x(x_1,y_1,z_1) \\ B_y(x_1,y_1,z_1) \\ B_z(x_1,y_1,z_1) \\ B_x(x_2,y_2,z_2) \\ B_y(x_2,y_2,z_2) \\ \dots \\ B_x(x_N,y_N,z_N) \\ B_y(x_N,y_N,z_N) \\ B_z(x_N,y_N,z_N) \end{pmatrix} = \begin{pmatrix} \mathcal{H}_{x,1}(x_1,y_1,z_1) & \mathcal{H}_{x,2}(x_1,y_1,z_1) & \cdots & \mathcal{H}_{x,48}(x_1,y_1,z_1) \\ \mathcal{H}_{y,1}(x_1,y_1,z_1) & \mathcal{H}_{y,2}(x_1,y_1,z_1) & \cdots & \mathcal{H}_{y,48}(x_1,y_1,z_1) \\ \mathcal{H}_{z,1}(x_1,y_1,z_1) & \mathcal{H}_{z,2}(x_1,y_1,z_1) & \cdots & \mathcal{H}_{z,48}(x_1,y_1,z_1) \\ \mathcal{H}_{x,1}(x_2,y_2,z_2) & \mathcal{H}_{x,2}(x_2,y_2,z_2) & \cdots & \mathcal{H}_{x,48}(x_2,y_2,z_2) \\ \mathcal{H}_{y,1}(x_2,y_2,z_2) & \mathcal{H}_{y,2}(x_2,y_2,z_2) & \cdots & \mathcal{H}_{y,48}(x_2,y_2,z_2) \\ \dots \\ \mathcal{H}_{x,1}(x_N,y_N,z_N) & \mathcal{H}_{x,2}(x_N,y_N,z_N) & \cdots & \mathcal{H}_{x,48}(x_N,y_N,z_N) \\ \mathcal{H}_{y,1}(x_N,y_N,z_N) & \mathcal{H}_{y,2}(x_N,y_N,z_N) & \cdots & \mathcal{H}_{y,48}(x_N,y_N,z_N) \\ \mathcal{H}_{z,1}(x_N,y_N,z_N) & \mathcal{H}_{z,2}(x_N,y_N,z_N) & \cdots & \mathcal{H}_{z,48}(x_N,y_N,z_N) \end{pmatrix} \begin{pmatrix} h_1 \\ h_2 \\ \dots \\ h_{48} \end{pmatrix}$$

$$\mathbf{B} = \hat{\mathcal{H}} \mathbf{h}, \tag{6.26}$$

where $\mathbf{B}$ is the column of the corrected magnetic field measured at each point, $\hat{\mathcal{H}}$ is the matrix of the Cartesian harmonic values and $\mathbf{h}$ is the column of the expansion coefficients. To solve Eq. (6.26) for $\mathbf{h}$, we can use the Singular Value Decomposition method.

Obviously, the field measurements have their statistical and systematic uncertainties which are not well known. This is why we have decided to apply the Bootstrap method (see Refs [72, 73]) for estimation of errors of the expansion coefficients $h_i$.

**Bootstrap method**

Let us assume, that we have a map consisting of $N$ points. This gives us $3N$ values of field, meaning $3N$ equations with 48 unknown parameters. Solving them would give us the values of harmonic expansion coefficients. Estimation of the covariance matrix of $n$ parameters can be obtained in the following steps:

1. Pick, randomly, $3N$ equations with repetitions from a set of $3N$ equations. This means that some of the equations will be taken into account more than once (having higher weight) and others are not taken into account at all.

2. From the resulting set of equations, calculate harmonic expansion coefficients ($\{h_i\}$, $i$ - coefficient number)

3. Repeat the first two steps $N_{boot}$ times (in this case, $N_{boot} = 3N/2$), leading to a set of coefficient values: $\{h_i^j\}$, where $i$ - coefficient number and $j$ - repetition number (from 1 to $N_{boot}$).

4. Treat these numbers as independent measurements and calculate the expected values and covariance matrix:

$$E(h_i) = \bar{h}_i = \frac{1}{N_{boot}} \sum_{j=1}^{N_{boot}} h_i^j, \tag{6.27}$$

$$\Sigma_{k,l} = \text{cov}(h_k, h_l) = \frac{1}{N_{boot}} \sum_{j=1}^{N_{boot}} (h_k^j - \bar{h}_k)(h_l^j - \bar{h}_l). \tag{6.28}$$
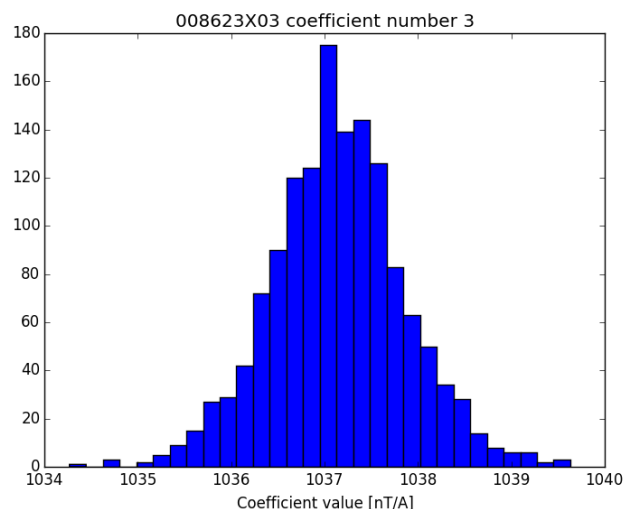
Figure 6.4: Example distribution of the coefficient number 3 of expansion in Eq. (6.24) for map number 008623X03 (map of main coil)

## 6.6  Analysis chain

To analyse one set of data (a field map) the following information is needed:

1. Offset values. They are obtained from a calibration run taken directly before and after the run to be analysed.

2. Non-orthogonality angles. They are obtained from one calibration run for all the runs. The best accuracy is obtained while using two separate calibration runs – the map with a large horizontal field component is used for determining $C, E$ angles and large vertical field is used for determining remaining angles.

3. Misalignment angles. They are obtained from the map of the main field coil.

The flow chart for analysis of magnetic field mapping measurement is presented in Fig. 6.5. The mapper data is stored in an ASCII file containing both position data and magnetic field data in cylindrical coordinates. Firstly, this data is corrected for offset values, then non-orthogonality of sensors, for misalignments and finally, transformed into Cartesian coordinates. The set of corrected data points is then used in the fit to Eq. (6.24) and the expansion coefficients of the field in the Cartesian harmonics are deduced.
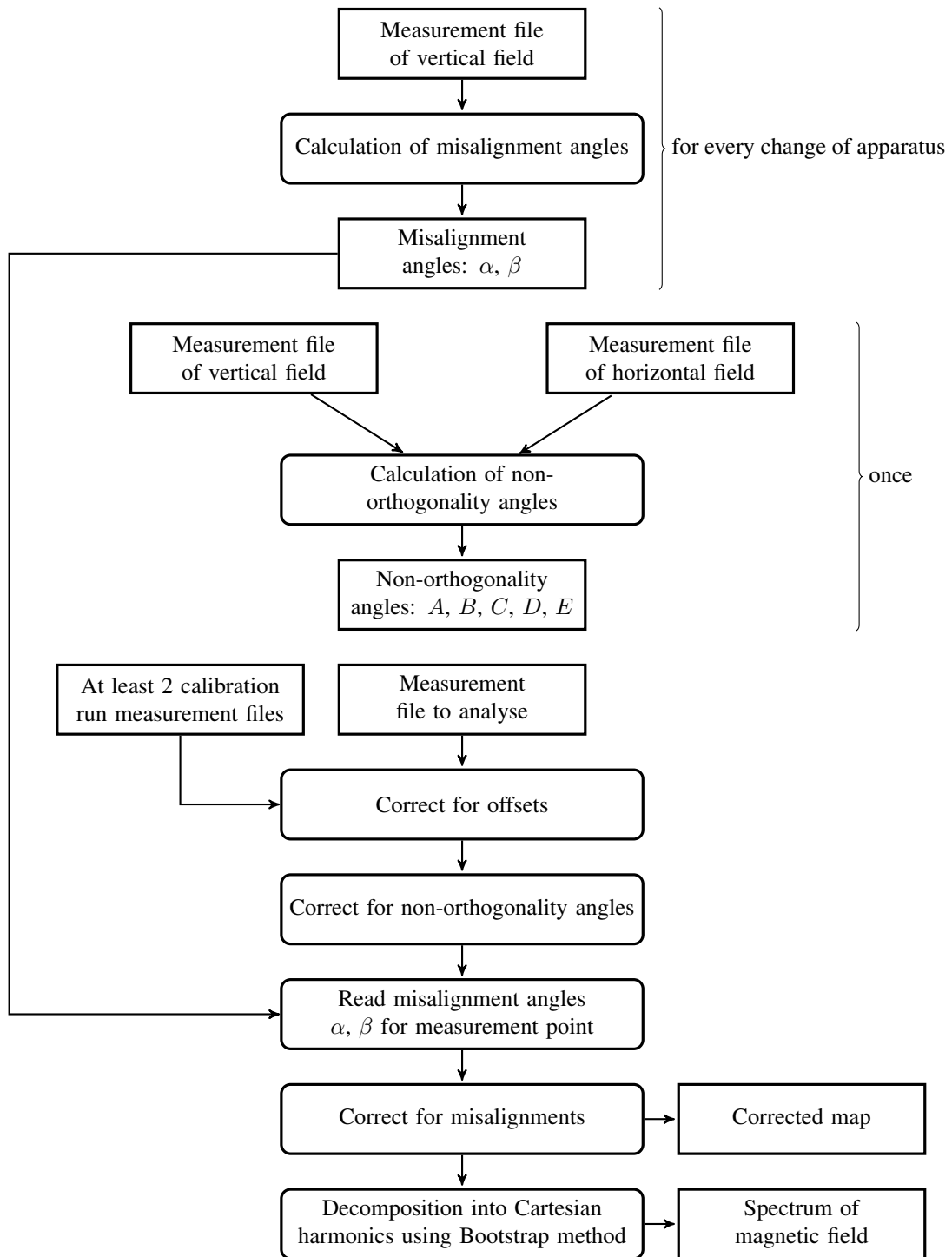
Figure 6.5: Flow graph for analysis of magnetic field mapping

## 6.7 Verification

### 6.7.1 Simulation

The analysis chain was verified with toy data. An artificial field map was constructed starting from the set of expansion coefficients for a real map of the main coil. This set is presented as crosses in Fig. 6.6. Constant value of 10 nT was added to each of measurements as the offset value, constant non-orthogonality angle transformation was applied. The misalignment angles were modelled as a function of position of measurement (see Fig. 6.7). The format of simulated data is the same as the one obtained from a real measurement. The full analysis chain was applied to this artificial map. The expansion coefficients were compared to that of the input field spectrum as can be seen in Fig. 6.6. Excellent matching shows that this analysis is consistent.
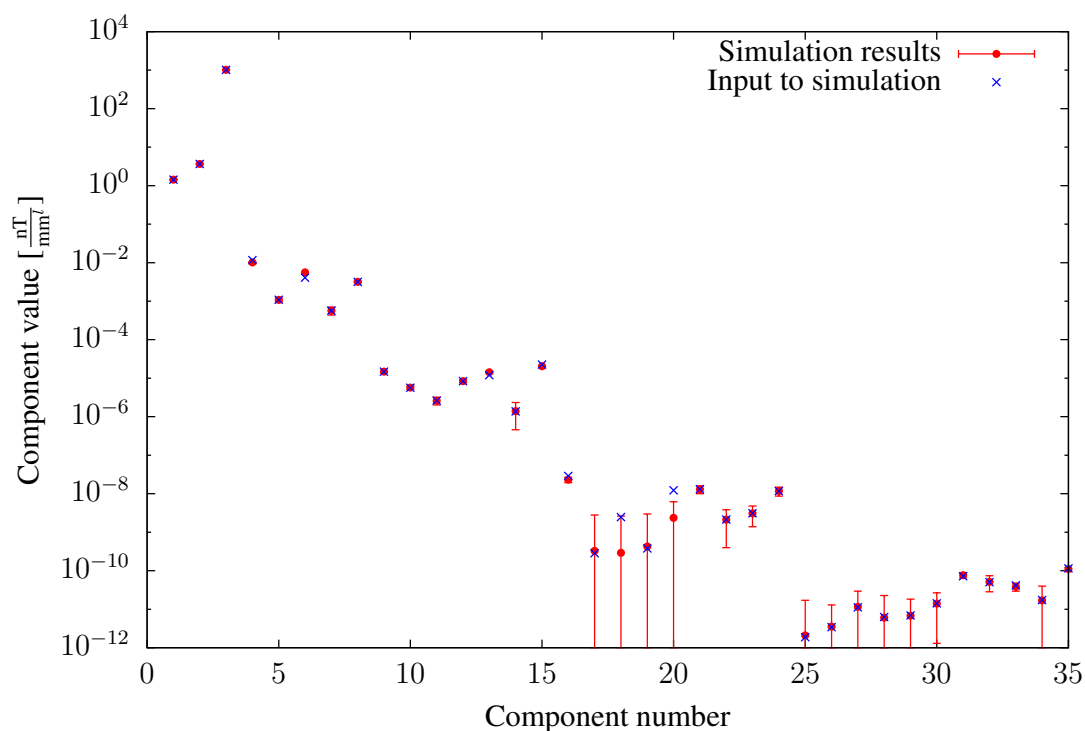


Figure 6.6: Results of simulated mapping analysis. Input was simulated with assumptions of constant pitch and roll angles and non-orthogonalities taken from real calculation. As an input field, we used field described by decomposition into harmonics defined in Tab. A.1. This decomposition was also taken from one of the measured maps.
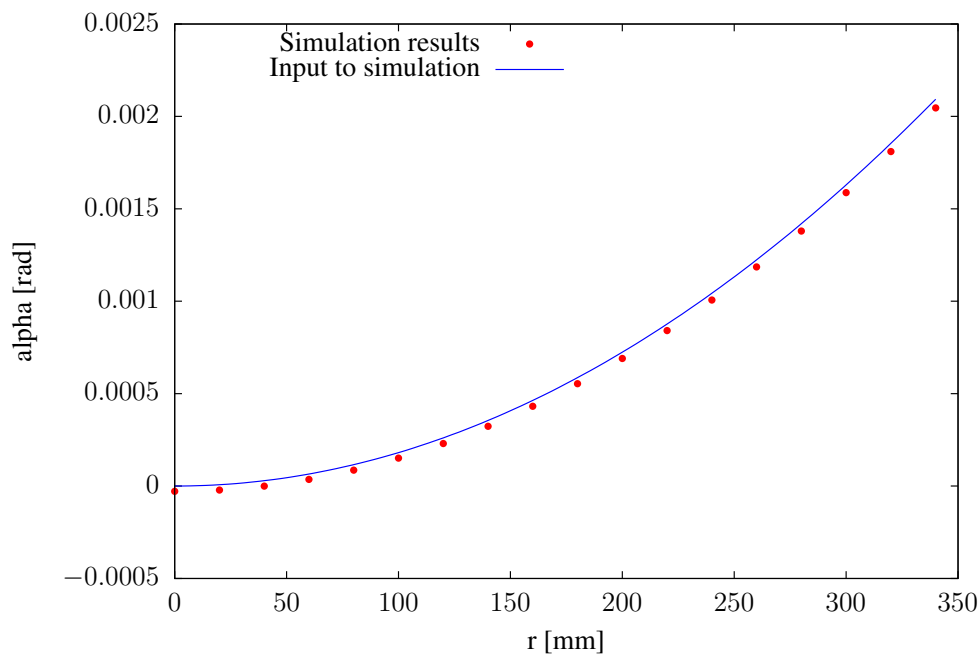
Figure 6.7: Pitch angle used as an input to simulation and obtained from analysis of simulated data

## 6.7.2 Impact of model corrections on real maps

Using the method described in Sec. 6.5, the analysis of the particular map No. 008650X14 was performed in two ways:

1. with application of corrections for non-orthogonalities and misalignments,

2. without these corrections.

Then the fit residuals of the field expansion are plotted in Figs. 6.8a and 6.8b. From those plots, it is obvious that the inclusion of corrections significantly improves the fit. Nevertheless, the distribution of the residuals for the corrected data is not centred at $(0, 0)$ and is relatively broad suggesting that, still, some effects are not included in the model.

Figure 6.8a indicates that the fit residuals have an anomalous distribution, with local minimum around $(0, 0)$. This should not happen for the field distribution fulfilling Maxwell's equations. The corrected (Fig. 6.8b) field behaves better: the fit residuals have a single and well defined maximum not too far from zero.

(a) without applied corrections of misalignments and non-orthogonality of sensor

(b) with applied corrections of misalignments and non-orthogonality of sensor

Figure 6.8: Two dimensional histogram of residuals of field in $x$ and $y$ directions

This model can still be improved with the local correction of misalignments. This could be possible with a magnetically quiet inclinometer mounted on the carrier alongside the magnetometer.

Summarizing, the corrections are essential and significantly improve the field map. However, they are still incomplete.

## 6.8 Results of the field map analysis

### 6.8.1 Corrections

Using the procedure described in the previous section, the non-orthogonality angles were calculated from measurement data taken in 2014: $A = 0.00088$ rad, $B = 0.0041$ rad, $C = 0.0083$ rad, $D = 0.015$ rad, $E = 0.59$ rad.

Offsets vary from run to run. All the values taken from calibration runs are presented in Fig. 6.9. The offset jumps are correlated with the shield demagnetization actions which change the magnetization of the fluxgate sensor's iron yoke and cause shifts in offset values. Also significant offset change from year to year is clearly visible.

Misalignment angles were evaluated in the field map analysis and it is possible to
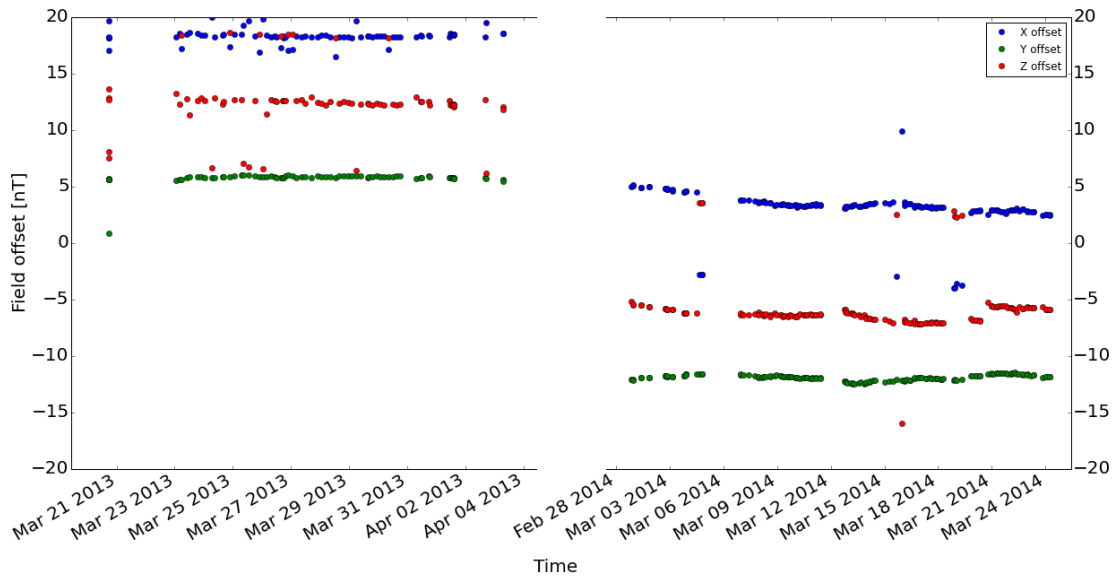
Figure 6.9: Fluxgate sensor offset values for all maps measured in 2013 and 2014.

verify them independently with the inclinometer, measuring the orientation of the carrier with respect to vertical direction defined by gravity. The comparison of results obtained with both methods for $z = 0$ is presented in Fig. 6.10. The shape is reproduced astonishingly well, but the absolute normalizations differ most probably due to magnetic field being not perfectly vertical. Pitch angle plot indicates clearly, that the mapper's arm is bent downwards when going to large $r$. Such a distortion of few millimetres was observed on site by the naked eye.

Changes of roll angle with changing radial position suggest that the rails on which the carrier is moving are not perfectly flat.

In Fig. 6.11, the comparison between measurements in 2013 and 2014 is presented. One can clearly see the change in roll angle shape. This may be related to the fact that, before the 2014 mapping campaign, the carrier had been equipped with rubber rings on its wheels. On the other hand, pitch angle measurements from both years are consistent with each other.
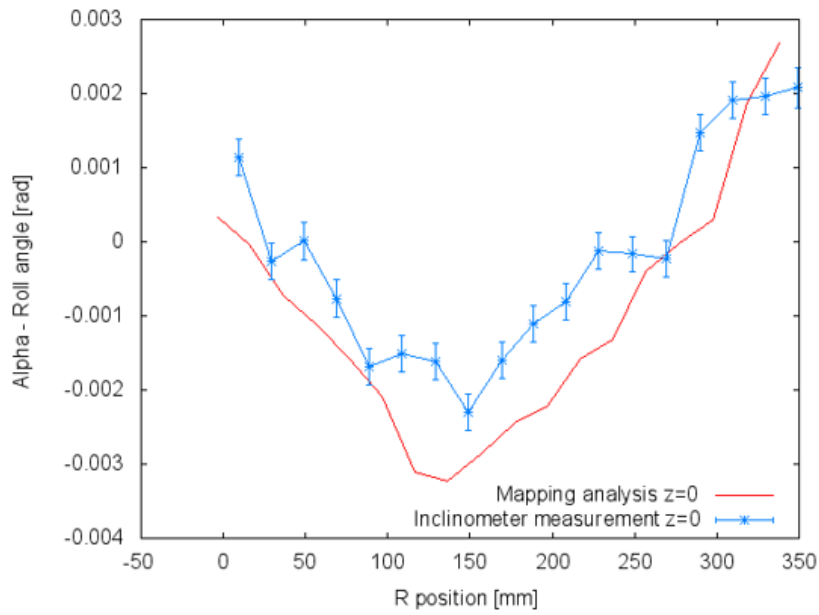
(a) Roll angle $\alpha$
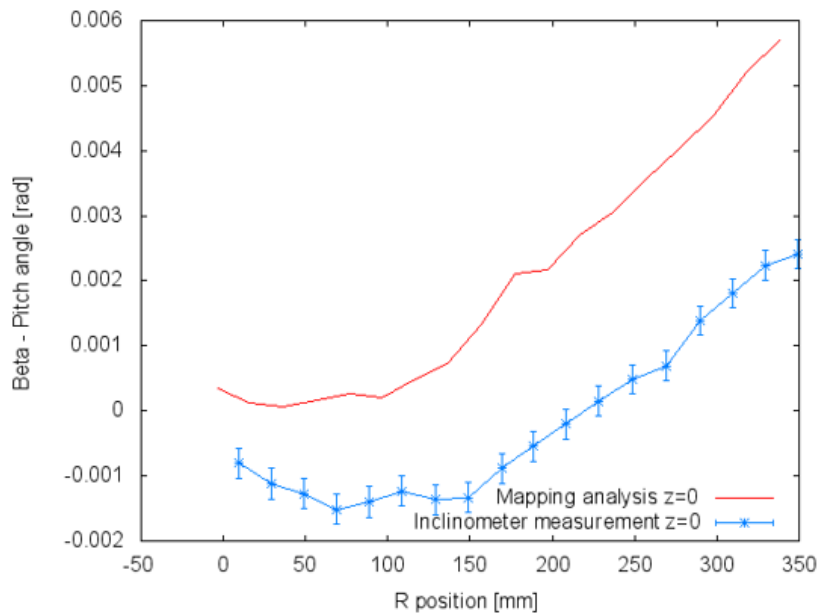


(b) Pitch angle $\beta$

Figure 6.10: Comparison of misalignment angles $\alpha$ and $\beta$ obtained from maps and from inclinometer measurements with $z = 0$.

(a) Roll angle $\alpha$ obtained from 2013 data



(b) Roll angle $\alpha$ obtained from 2014 data



(c) Pitch angle $\beta$ obtained from 2013 data



(d) Pitch angle $\beta$ obtained from 2014 data
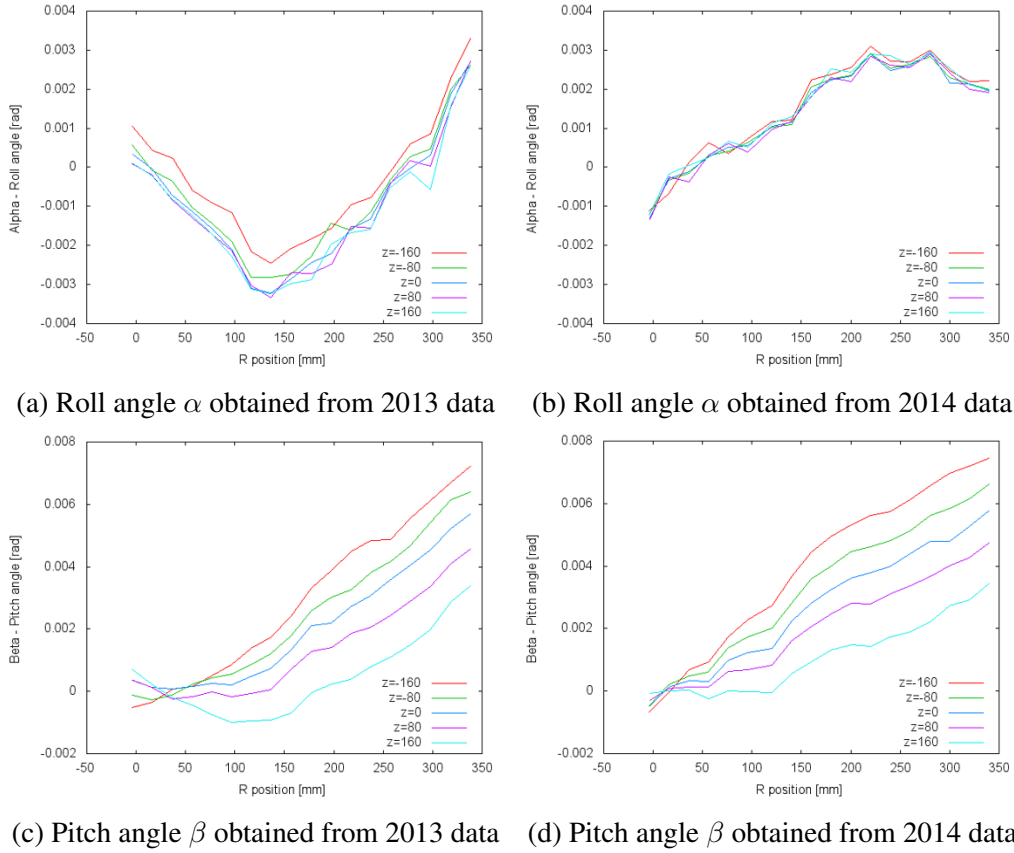
Figure 6.11: Comparison of misalignment angles $\alpha$ and $\beta$ obtained from analysis in 2013 and 2014.

## 6.9 Field stability

The results obtained from maps can be used to judge the stability of the field. To do that one can compare the results from measurements taken without any currents flowing through main field coil and trim coils. This magnetic field is the ambient magnetic field, resulting from material composition of the apparatus' construction and from magnetic field sources not related to the experiment.

In Figures 6.12 to 6.15 evolution of the harmonic expansion coefficients number 1, 2, 3 and 9 for background field are presented. Points on the left side of vertical line present results from the 2013 mapping campaign, while the ones on the right were taken in 2014.

Surprisingly, the results from both years are not far apart. The biggest disturbance of

the field is observed in the maps no. 008684X04 and 008684X10 where a new (unusual) demagnetization method of the passive shield was tested.
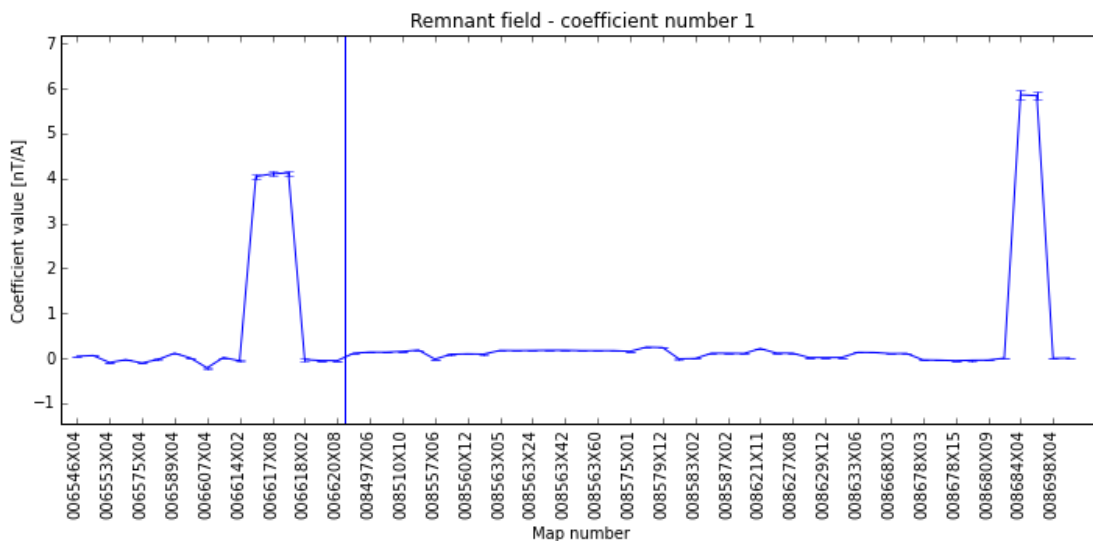


Figure 6.12: 1st Harmonic expansion coefficient (uniform in $x$ direction) of background field in the function of map number. Vertical line separates 2013 measurements from 2014.
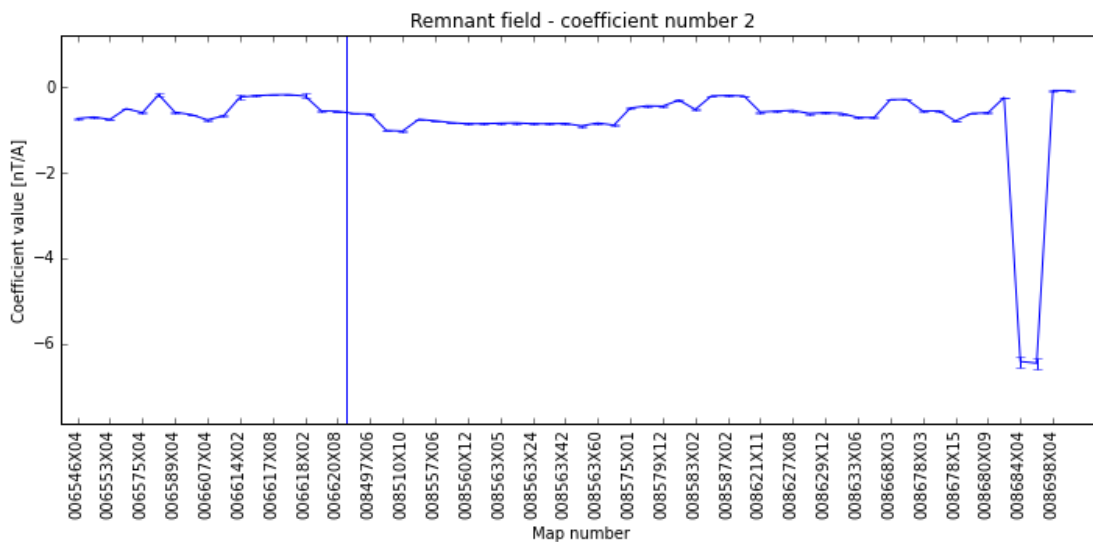


Figure 6.13: Same as Fig. 6.12, but for the 2nd harmonic expansion coefficient (uniform component in $y$ direction).
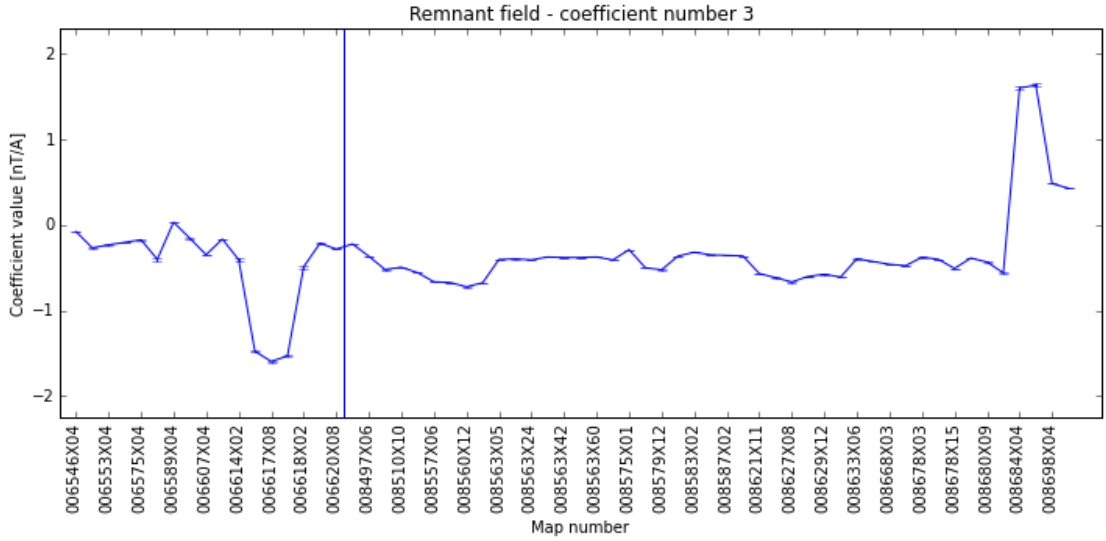
Figure 6.14: Same as Fig. 6.12, but for the 3rd harmonic expansion coefficient (uniform component in $z$ direction).
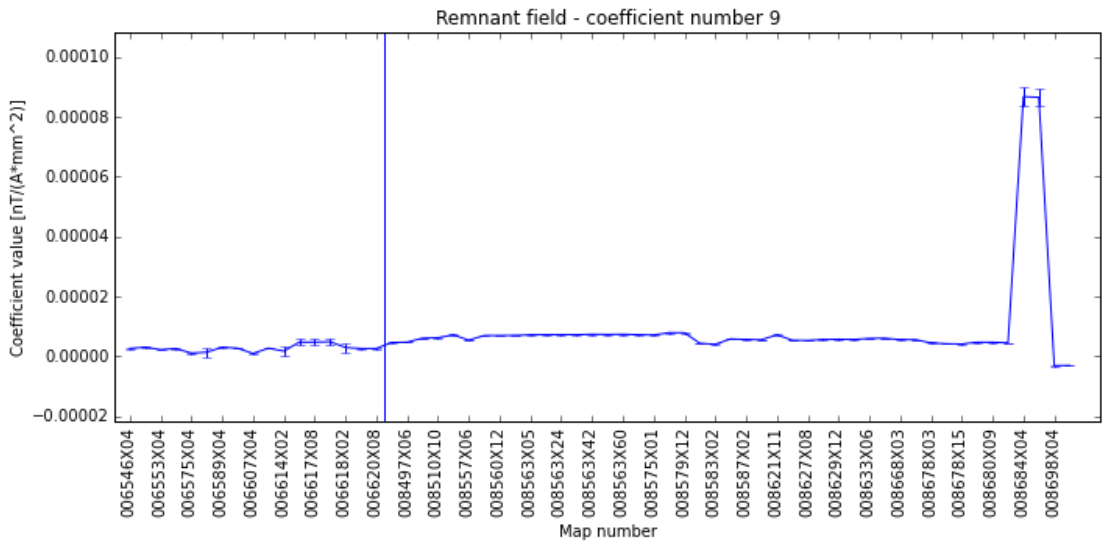


Figure 6.15: Same as Fig. 6.12, but for the 9th harmonic expansion coefficient (component proportional to $(x^2 - z^2, 0, -2xz)$).

## 6.10 Trim coil current optimization with data from field mapping

The main reason for the field mapping effort was the hope that the field maps will allow to predict the optimal currents in the trim coils such that the field gradients are eliminated. The indication of the success would be a long $T_2$ time.

Having the decomposition coefficients of field produced by each of the coils – $h_i$, it is possible to calculate optimal currents for all coils, such that the generated magnetic field is uniform and oriented in the $z$ direction. This corresponds to the condition, that all the coefficients shall be equal 0 except the $h_3$, which shall be non-zero. This condition can be represented by the set of equations,

$$0 = h_{i,notcorrected} + \sum_{j=0}^{n_{coils}} I_j \tilde{h}_{i,j} \text{ for } i \neq 3, \tag{6.29}$$

where $i$ - denotes the harmonic coefficient number, $j$ - denotes the coil number, $h_{i,notcorrected}$ is the harmonic expansion coefficient for the magnetic field not originating from coils, $I_j$ is the j-th current in coil and $\tilde{h}_{i,j}$ is the $i$-th harmonic coefficient of the magnetic field generated by $j$-th coil measured during mapping, divided by the current flowing through this coil during measurement.

The set (6.29) can be solved using the Singular Value Decomposition method. However, to estimate uncertainty of currents, the following method was used.

The analysis described in previous sections results in expectation values of the coefficients $h_{i,j}$ and their covariance matrices $\text{cov}(h_{k,j}, h_{l,j})$. Each magnetic field map contains information about total field, i.e. field created by a coil and field coming from other apparatus parts and outside sources. To extract net field coming from coils, the remnant field was subtracted from the individual coil calibration maps. For that purpose, two background field maps were used (one taken before and one after the coil calibration map measurement). This operation transforms the covariance matrix cov to:

$$\text{cov}(h_{k,j} - \frac{h_{k,\text{background},1} + h_{k,\text{remnant},2}}{2}, h_{l,j} - \frac{h_{l,\text{background},1} + h_{l,\text{background},2}}{2})$$
$$= \text{cov}(h_{k,j}, h_{l,j}) + \frac{1}{4} \left( \text{cov}(h_{k,\text{background},1}, h_{l,\text{background},1}) + \text{cov}(h_{k,\text{background},2}, h_{l,\text{background},2}) \right), \tag{6.30}$$

where $\text{cov}(h_{k,j} - \frac{h_{k,\text{remnant},1} + h_{k,\text{remnant},2}}{2}, h_{l,j} - \frac{h_{l,\text{remnant},1} + h_{l,\text{remnant},2}}{2})$ is the covariance matrix of the expansion coefficients of the pure coil field map - obtained after removal of remnant field, $\text{cov}(h_{k,\text{remnant},1}, h_{l,\text{remnant},1})$ is the covariance matrix of the expansion coefficients of the remnant field map taken before the coil map measurement. Similarly $\text{cov}(h_{k,\text{remnant},2}, h_{l,\text{remnant},2})$ is the covariance matrix of the expansion coefficients of the remnant field map taken after the coil map measurement. Equation (6.30) assumes, that maps are independent, resulting in cross covariation equal to 0.

This operation leads to a set of expansion coefficients and covariance matrices for each coil. These matrices have eigenvalues $\lambda_{k,j}$ and corresponding eigenvectors $\vec{v}_{k,j}$, where $j$ denotes the coil number and $k$ denotes the eigenvector/eigenvalue number. To include complete information about uncertainties of the expansion coefficients, the following Monte Carlo algorithm is used:

1. Expansion coefficients vector $\vec{h}_{j,\text{simulated}}$ for each of the coils (6.29) is picked at random from equation:

$$\vec{h}_{j,\text{simulated}} = \text{E}(\vec{h}_j) + \sum_{k=1}^{48} \vec{v}_{k,j}\,\text{random}(0, \sqrt{\lambda_{k,j}}), \qquad (6.31)$$

where $\vec{h}_{j,\text{simulated}}$ is the vector containing harmonic expansion coefficients including uncertainties, which is used later in calculation of the current, $\text{E}(\vec{h}_j)$ is the expectation value of vector containing harmonic expansion coefficients, $\text{random}(0, \sqrt{\lambda_{k,j}})$ is a pseudo-random number taken from the Gaussian distribution centred around zero with $\sigma = \sqrt{\lambda_{k,j}}$.

2. Randomly picked expansion coefficients are used as an input to solve Eq. (6.29) for currents in coils $I_j$.

3. This procedure is repeated $10{,}000$ times. The expected values for currents and their uncertainties are estimated using arithmetic mean and standard deviation estimators.

Results of these calculations are presented in Figs 6.16 for the main field in down direction and 6.17 for the field in up direction. They are compared with the results of previous trim coils' currents optimization, performed in 2010 by Gilles Quemener [74,

75]. The optimized currents for some of the coils are consistent, but there are significant differences in other coils, like BTC, HVK and BAC. Potentially the proposed approach can improve the $T_2$ time leading to better sensitivity of measurement of neutron EDM, but still it has to be verified on site.
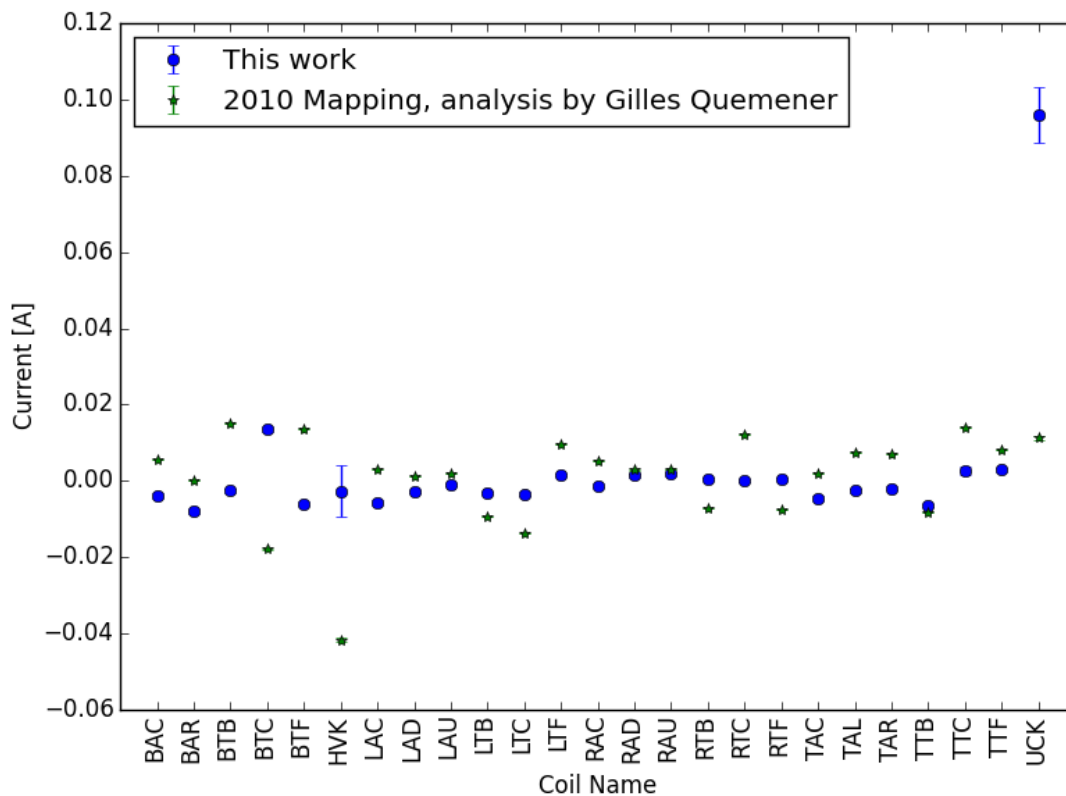


Figure 6.16: Optimal currents calculated for each of the trim coils for the main field down configuration.
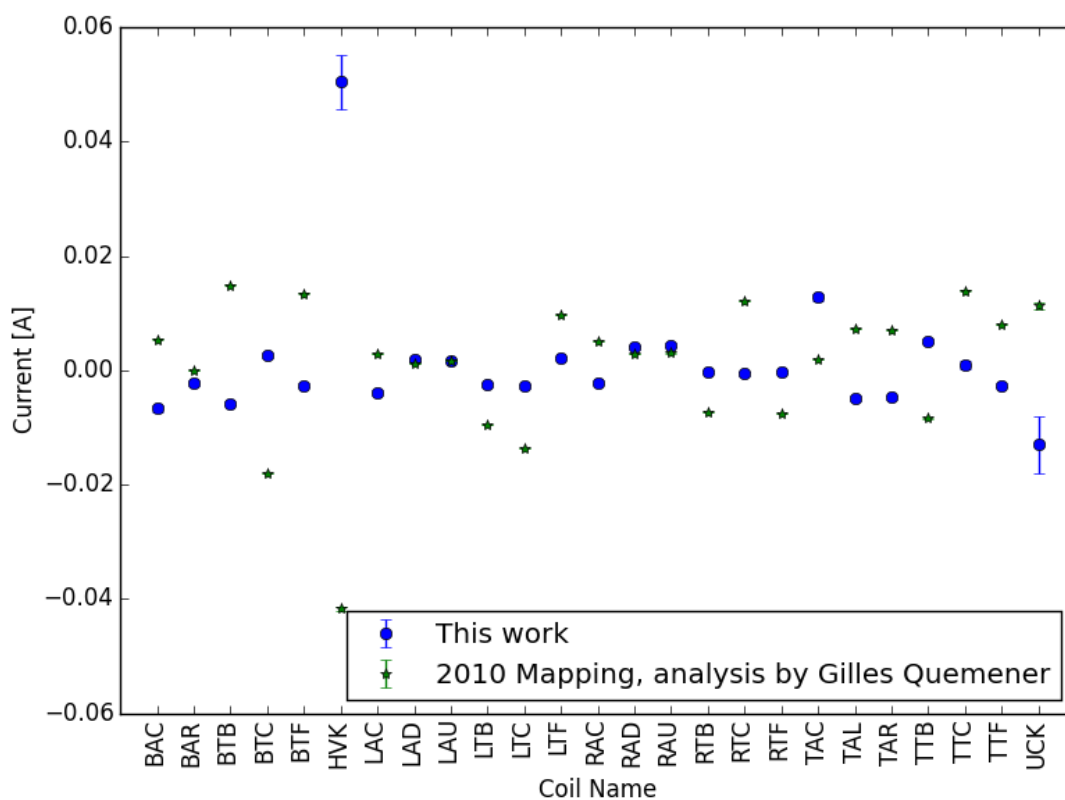
Figure 6.17: Same as Fig. 6.16 but for the main field up configuration.

# Chapter 7

# Summary

Magnetic field control is a crucial issue in measurements of the neutron electric dipole moment. Magnetic field in such precise experiments must be as stable as possible and also well known. The first goal is achieved using a passive shield working together with an active magnetic shielding. In this work, four magnetic field compensation systems were considered and compared. It turns out that the field is shielded most efficiently by the spherical coil system configured using solid mathematical foundations.

The simplest considered system, the SFC, is in operation as a part of the nEDM experiment at PSI. It has a relatively simple construction consisting of 6 coils. Astonishingly, the measured performance is significantly better than the first results from the more sophisticated Merritt setup, but simulations show that it is possible to achieve better results with other systems.

The Merritt setup is based on a concept for highly uniform magnetic field generation. This is achieved by adding 6 coils to the SFC setup, resulting in 12 coils in total. The prototype was built, but it was performing below expectations. The main reasons were the hardware problems mostly related to crosstalk between acquisition channels. The simulation of operation of this system shows that the expected improvement over the SFC setup is modest. In order to significantly improve performance adding 12 diagonal coils is considered. This would result in satisfactory operation, but on the cost of much more complicated construction and much higher costs of power supplies needed to drive current through coils.

The third compensation system is the cellular coil setup, consisting of a large num-

ber of small coils with sensors in the coil centres. The simulated performance of such a setup is the worst (in terms of relative difference $\Delta$) of all considered systems, but it compensates the magnetic field uniformly inside the volume surrounded by the compensation coils. It has also some practical advantages. The implementation of doors and other openings would be easier than in other systems.

According to simulations, the spherical coil system provides an optimal compensation: its performance is 2-5 orders of magnitude better than for other setups. This property comes from the fact that it utilizes orthogonal decomposition of the field by vector spherical harmonics. Combining these basis functions with stream function formalism for determining wire shapes and positions results in a set of spherical coils, grouped in multipoles. Further performance improvement is possible by simply adding higher multipole coils. However, the practical realization of such a system is difficult. Several design possibilities were considered, but none of them solved the problem – how to design doors through wires covering the whole surface of a sphere.

Another crucial part of the magnetic field control in the nEDM experiment at PSI is based on magnetic field mapping on the experiment site. The magnetic field map would allow to estimate systematic effects, but also to tune the field uniformity. Field mapping is performed by a specially constructed robot placed inside the passive shield and using a fluxgate sensor or a c vector caesium magnetometer. In this work, I have concentrated my efforts on the analysis of data taken by a fluxgate sensor.

Both the used sensor and mapping device itself are not perfect, leading to necessary corrections. A special model was developed to include in the analysis misalignments of the mapper elements and non-orthogonalities of sensors. Dedicated runs were used for estimation of the read offset values. The misalignment angles, extracted from the fit of the model to the experimental data were verified with the measurement using an inclinometer. Validation of the analysis was performed using a simulated field map with assumed imperfection parameters.

It was shown with a real field map, that the application of correction deduced from model fit, significantly improve the map consistency.

For easier comparison, the results of the map analysis are expressed in terms of the Cartesian harmonic expansion coefficients. In this way, it is possible to compare the maps spanned on different mesh structures. Comparisons show stability of the field at a level of one nT throughout two measurement campaigns. The uncertainty of the

expansion coefficients was described by the covariance matrices, estimated using the Bootstrap method. Additionally, the successful verification of this process was performed.

For the nEDM Experiment at PSI, the most important result delivered by the analysis of field maps would be the optimal configuration for trim coils' currents. The presented results can be used as starting points for manual fine tuning.

All in all, in this work, two aspects of magnetic field control were addressed. In the first one, several active magnetic field compensation systems are compared suggesting optimal solutions for future use. In the second, the measurements of magnetic field maps were analysed, leading to a set of the Cartesian harmonic expansion coefficients ready for calculations of systematic effects and for use as input for Monte Carlo simulations.

# Appendix A

# Cartesian harmonic basis functions

Table A.1: List of used Cartesian harmonic basis functions

| Nr | coordinate | | |
|---|---|---|---|
| | x | y | z |
| 1 | $1$ | $0$ | $0$ |
| 2 | $0$ | $1$ | $0$ |
| 3 | $0$ | $0$ | $1$ |
| 4 | $x$ | $0$ | $-z$ |
| 5 | $y$ | $x$ | $0$ |
| 6 | $0$ | $y$ | $-z$ |
| 7 | $z$ | $0$ | $x$ |
| 8 | $0$ | $z$ | $y$ |
| 9 | $x^2 - z^2$ | $0$ | $-2xz$ |
| 10 | $2xy$ | $x^2 - z^2$ | $-2yz$ |
| 11 | $y^2 - z^2$ | $2xy$ | $-2xz$ |
| 12 | $0$ | $y^2 - z^2$ | $-2yz$ |
| 13 | $2xz$ | $0$ | $x^2 - z^2$ |
| 14 | $yz$ | $xz$ | $xy$ |
| 15 | $0$ | $2yz$ | $y^2 - z^2$ |
| 16 | $x^3 - 3xz^2$ | $0$ | $z^3 - 3x^2 z$ |
| 17 | $3x^2 y - 3yz^2$ | $x^3 - 3xz^2$ | $-6xyz$ |
| 18 | $3xy^2 - 3xz^2$ | $3x^2 y - 3yz^2$ | $-3x^2 z - 3y^2 z + 2z^3$ |
| 19 | $y^3 - 3yz^2$ | $3xy^2 - 3xz^2$ | $-6xyz$ |
| 20 | $0$ | $y^3 - 3yz^2$ | $z^3 - 3y^2 z$ |
| 21 | $3x^2 z - z^3$ | $0$ | $x^3 - 3xz^2$ |
| 22 | $6xyz$ | $3x^2 z - z^3$ | $3x^2 y - 3yz^2$ |
| 23 | $3y^2 z - z^3$ | $6xyz$ | $3xy^2 - 3xz^2$ |
| 24 | $0$ | $3y^2 z - z^3$ | $y^3 - 3yz^2$ |
| 25 | $x^4 - 6x^2 z^2 + z^4$ | $0$ | $4xz^3 - 4x^3 z$ |
| 26 | $4x^3 y - 12xyz^2$ | $x^4 - 6x^2 z^2 + z^4$ | $4yz^3 - 12x^2 yz$ |
| 27 | $3x^2 y^2 - 3x^2 z^2 - 3y^2 z^2 + z^4$ | $2x^3 y - 6xyz^2$ | $-2x^3 z - 6xy^2 z + 4xz^3$ |
| 28 | $2xy^3 - 6xyz^2$ | $3x^2 y^2 - 3x^2 z^2 - 3y^2 z^2 + z^4$ | $-6x^2 yz - 2y^3 z + 4yz^3$ |
| 29 | $y^4 - 6y^2 z^2 + z^4$ | $4xy^3 - 12xyz^2$ | $4xz^3 - 12xy^2 z$ |
| 30 | $0$ | $y^4 - 6y^2 z^2 + z^4$ | $4yz^3 - 4y^3 z$ |
| 31 | $4x^3 z - 4xz^3$ | $0$ | $x^4 - 6x^2 z^2 + z^4$ |
| 32 | $3x^2 yz - yz^3$ | $x^3 z - xz^3$ | $x^3 y - 3xyz^2$ |
| 33 | $6xy^2 z - 2xz^3$ | $6x^2 yz - 2yz^3$ | $3x^2 y^2 - 3x^2 z^2 - 3y^2 z^2 + z^4$ |
| 34 | $y^3 z - yz^3$ | $3xy^2 z - xz^3$ | $xy^3 - 3xyz^2$ |
| 35 | $0$ | $4y^3 z - 4yz^3$ | $y^4 - 6y^2 z^2 + z^4$ |
| 36 | $x^5 - 10x^3 z^2 + 5xz^4$ | $0$ | $-5x^4 z + 10x^2 z^3 - z^5$ |
| 37 | $5x^4 y - 30x^2 yz^2 + 5yz^4$ | $x^5 - 10x^3 z^2 + 5xz^4$ | $-20x^3 yz + 20xyz^3$ |
| 38 | $10x^3 y^2 - 10x^3 z^2 - 30xy^2 z^2 + 10xz^4$ | $5x^4 y - 30x^2 yz^2 + 5yz^4$ | $-5x^4 z - 30x^2 y^2 z + 20x^2 z^3 + 10y^2 z^3 - 3z^5$ |
| 39 | $x^2 y^3 - 3x^2 yz^2 - y^3 z^2 + yz^4$ | $x^3 y^2 - x^3 z^2 - 3xy^2 z^2 + xz^4$ | $-2x^3 yz - 2xy^3 z + 6xyz^3$ |
| 40 | $5xy^4 - 30xy^2 z^2 + 5xz^4$ | $10x^2 y^3 - 30x^2 yz^2 - 10y^3 z^2 + 10yz^4$ | $-30x^2 y^2 z - 10y^4 z + 5x^2 z^3 + 20y^2 z^3 - 3z^5$ |
| 41 | $y^5 - 10y^3 z^2 + 5yz^4$ | $5xy^4 - 30xy^2 z^2 + 5xz^4$ | $-20xy^3 z + 20xyz^3$ |
| 42 | $0$ | $y^5 - 10y^3 z^2 + 5yz^4$ | $-5y^4 z + 10y^2 z^3 - z^5$ |
| 43 | $5x^4 z - 10x^2 z^3 + z^5$ | $0$ | $x^5 - 10x^3 z^2 + 5xz^4$ |
| 44 | $20x^3 yz - 20xyz^3$ | $5x^4 z - 10x^2 z^3 + z^5$ | $5x^4 y - 30x^2 yz^2 + 5yz^4$ |
| 45 | $15x^2 y^2 z - 5x^2 z^3 - 5y^2 z^3 + z^5$ | $10x^3 yz - 10xyz^3$ | $5x^3 y^2 - 5x^3 z^2 - 15xy^2 z^2 + 5xz^4$ |
| 46 | $10xy^3 z - 10xyz^3$ | $15x^2 y^2 z - 5x^2 z^3 - 5y^2 z^3 + z^5$ | $5x^2 y^3 - 15x^2 yz^2 - 5y^3 z^2 + 5yz^4$ |
| 47 | $5y^4 z - 10y^2 z^3 + z^5$ | $20xy^3 z - 20xyz^3$ | $5xy^4 - 30xy^2 z^2 + 5xz^4$ |
| 48 | $0$ | $5y^4 z - 10y^2 z^3 + z^5$ | $y^5 - 10y^3 z^2 + 5yz^4$ |

# Appendix B

# Simplification of spherical coils by approximation with truncated icosahedron

Building spherical coils of the size big enough to enclose the neutron EDM experiment would be a challenge. To reduce costs and simplify the assembly, various approximations of the sphere were considered. As the most promising, the truncated icosahedron was found. It is a structure built up of 32 walls - 20 hexagonal and 12 pentagonal. This shape resembles Buckminsterfullerene (see Ref. [76]) and the classical football, hence the nickname for those coils: football coils.

The football coil wire positions are obtained by the projection of the spherical coil on the surface of a truncated icosahedron along the radii of the sphere. The resulting coils are presented in Figures B.1a and B.1b.

Even though they are not spherical, the magnetic field generated by them is an approximation of the one produced by exact spherical coils within 1% accuracy. An example map of relative deviation is shown in Fig. B.2.

Several methods for exact positioning of the wires were considered. None of the turned to be satisfactory. The most promising are:

**Printed Board Circuits** – Each of 32 faces of coil was considered to be manufactured using a multi-layer printed board circuit with thick layers for driving 1 A currents. This method is the least time consuming, but the most expensive. Estimated cost

of the whole set of 8 coils would be around $50,000$ CHF for a set of coils with radius of $1$ m.

**Mechanical support** – We have also considered planes made of PVC as a support for the wires. On top of them, the grooves would be milled to position wires exactly. This method has main disadvantage: manual winding requires plenty of time - single uniform field coil, which could compensate the Earth's magnetic field with a current of $1$ A requiring around $400$ m of wire, would weigh around $28$ kg. To obtain optimal performance, 8 coils are necessary, which makes mechanical construction very difficult.
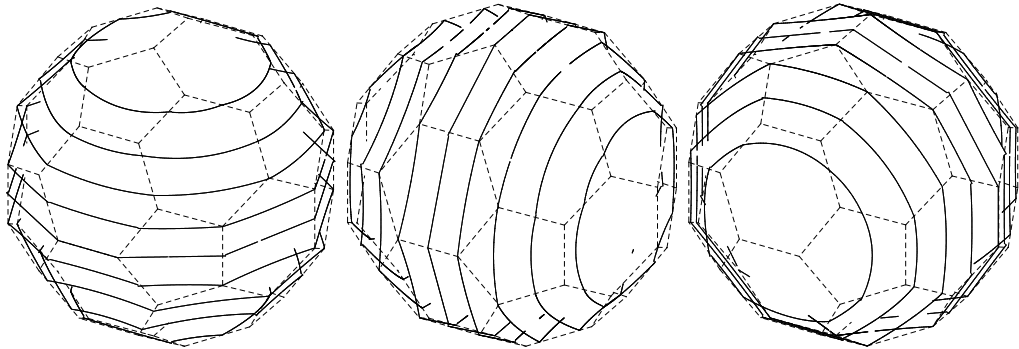
(a) Coils creating uniform magnetic fields ($l = 1$ case).
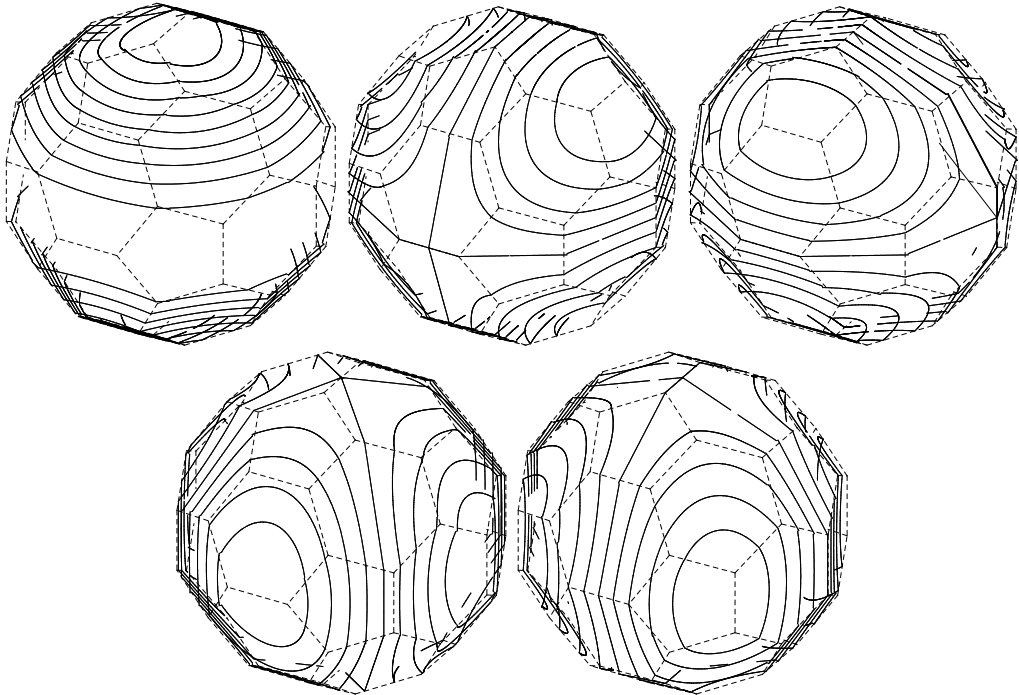


(b) Coils creating quadrupolar field components ($l = 2$ case).

Figure B.1: „Football Coils" wound on a surface of a truncated icosahedron. For clarity, the number of turns is taken to be $n = 9$.
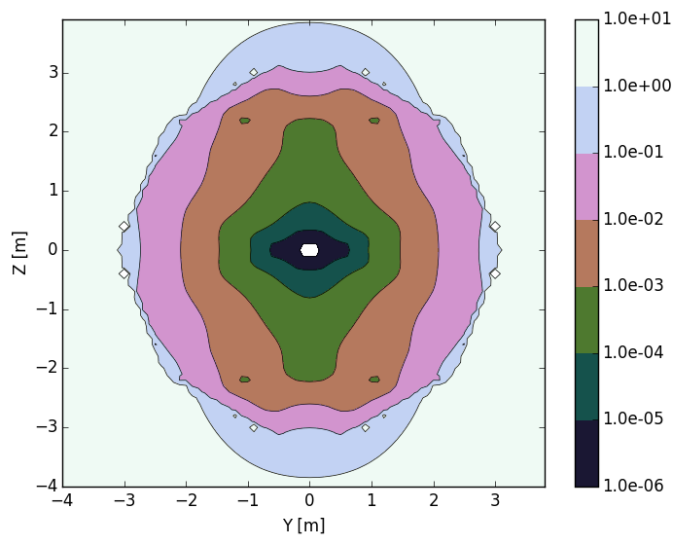
Figure B.2: Map of relative difference between theoretical field, described by Eq. (4.37) with $\alpha_{lm} = \delta_{l,1}\delta_{m,0}$ (uniform field in $z$ direction) and real field generated by the coil in Fig. B.1a

# Appendix C

# Verification of the covariance matrix estimation with the Bootstrap method

The Bootstrap method is a commonly used method for non-parametric estimation. Both the expectation value and its uncertainty are correctly estimated by this method (see Ref. [77]). To verify the estimation of the covariance matrix of the Cartesian harmonic expansion coefficient, we apply the following procedure:

1. The magnetic field is described by the harmonic spectrum as in Fig. C.1 - values of all coefficients are equal to 1 except the 3rd one, which is equal to 1000. This simulates a real measurement of magnetic field created by the main coil in the nEDM experiment giving the dominant, mostly uniform, vertical field component along the $z$ axis. Other components are much smaller.

2. The measurement of the magnetic field component in space is simulated by picking a pseudo-random number from the Gaussian distribution with the mean value $\vec{B}_{mean,simulated}$ calculated using a harmonic spectrum from Fig. C.1 (see Eq. (C.1) below) and standard deviation $\sigma = 1$ for all components.

$$\vec{B}_{mean,simulated}(x,y,z) = \sum_{i=1}^{48} h_i \mathcal{H}_i(x,y,z) \quad h_i = 1,\ i \neq 3,\ h_3 = 1000 \quad \text{(C.1)}$$

3. A map of magnetic field obtained in this way can be used now to calculate back harmonic expansion coefficients with their covariance matrix using the Bootstrap
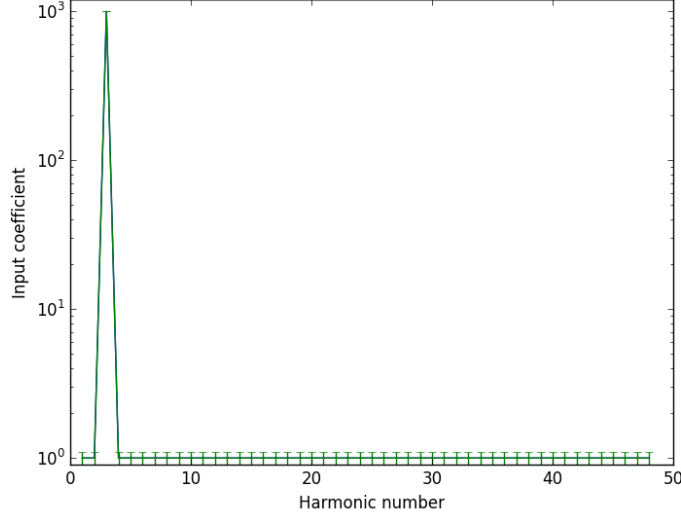
Figure C.1: Harmonic spectrum used as input for verification of Bootstrap method. Values for all functions are 1 except the 3rd function, for which the value is equal 1000.

method (for more details see chapter 6.5).

4. To include information about the covariance between two coefficients in further calculations, we need to find eigenvalues and eigenvectors of the covariance matrix. This method is commonly used as a part of Principal Component Analysis (see Ref. [78]). Eigenvectors $\vec{v}_i$ of the covariance matrix span base describing uncertainties of coefficients, while eigenvalues $\lambda_i$ describe variances corresponding to each eigenvector. This means that value of the magnetic field at point $(x, y, z)$, which includes uncertainty estimated by covariance matrix is described by:

$$\vec{B}_{bootstrap,result}(x, y, z) = \mathcal{H}_{tot}\left(\mathrm{E}(h) + \sum_{i=1}^{48} \vec{v}_i \, \mathrm{random}(0, \sqrt{\lambda_i}), x, y, z\right),$$
(C.2)

where:

$$\mathcal{H}_{tot}(\vec{v}, x, y, z) = \sum_{i=1}^{48} v_i \mathcal{H}_i(x, y, z),$$
(C.3)

$\mathrm{E}(h)$ is the vector of expectation values of harmonic expansion coefficients, $\vec{v}_i$ are eigenvectors of covariance matrix, $\lambda_i$ are corresponding eigenvalues, $\mathrm{random}(0, \sqrt{\lambda_i})$

is a pseudo-random number generated with Gaussian distribution centred around 0 with $\sigma = \sqrt{\lambda_i}$. Repeating the procedure many more times than the size of the matrix (we use 1000 repetitions) allows us to calculate the expectation value in the point (x,y,z):

$$B_{k,bootstrap,mean}(x, y, z) = \frac{1}{1000} \sum_{i=1}^{1000} B_{k,bootstrap,result,i}(x, y, z), \qquad \text{(C.4)}$$

where $k \in \{x, y, z\}$ - denotes the component, $\vec{B}_{k,bootstrap,result,i}(x, y, z)$ is the $k$-th component of the result of Eq. (C.2) for i-th repetition. The uncertainty of this value can be obtained from the standard deviation estimator:

$$\vec{\sigma}\left(B_{k,bootstrap}(x, y, z)\right) =$$

$$= \sqrt{\frac{1}{1000} \sum_{i=1}^{1000} \left(B_{k,bootstrap,result,i}(x, y, z) - B_{k,bootstrap,mean}(x, y, z)\right)^2} \quad \text{(C.5)}$$

5. The above procedure is repeated for 1000 times to get an adequate number of trials and the value

$$B_{k,normalized} \frac{B_{k,bootstrap,result}(x, y, z) - \vec{B}_{k,mean,simulated}(x, y, z)}{\sigma(\vec{B}_{k,bootstrap}(x, y, z))} \qquad \text{(C.6)}$$

is included on the histogram. If all the assumptions made are correct, this variable should follow Normal Distribution. Two resulting histograms are presented in Figs. C.2 and C.3. These histograms show the distributions of normalized $y$ and $z$ component at the point $(6.840, -18.79, 80)$. Good description by the Normal Distribution allow us to conclude that the assumptions are correct and the analysis is valid.
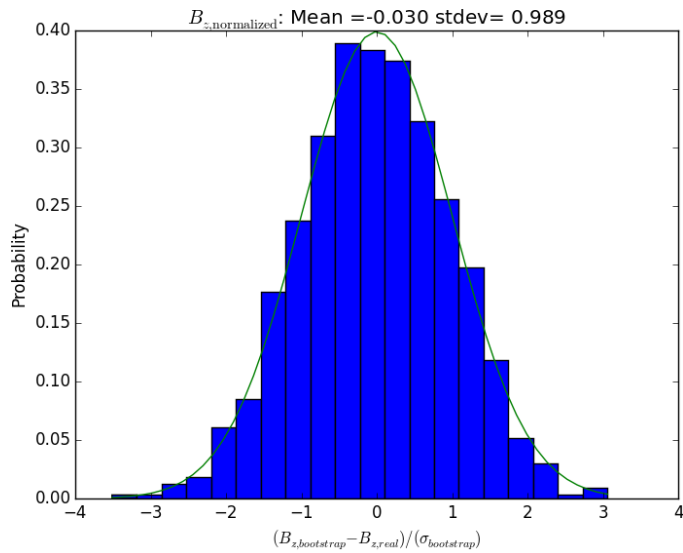
Figure C.2: Histogram of $B_{y,normalized}$ for point $(6.8, -18.8, 80)$mm obtained from the Bootstrap verification procedure. More details in Section C. Line marks normal distribution.
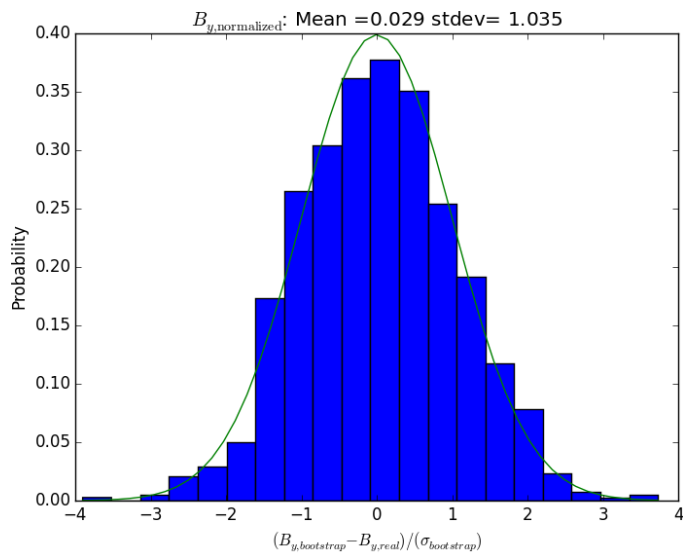


Figure C.3: Same as FigC.2, but for $B_{z,normalized}$ for the same point.

# Bibliography

[1]  C. D. Anderson. "The Positive Electron". In: *Phys. Rev.* 43 (6 Mar. 1933), pp. 491–494. DOI: `10.1103/PhysRev.43.491`.

[2]  J. H. Christenson et al. "Evidence for the $2\pi$ Decay of the $K_2^0$ Meson". In: *Phys. Rev. Lett.* 13 (4 July 1964), pp. 138–140. DOI: `10.1103/PhysRevLett.13.138`.

[3]  A. D. Sakharov. "Violation of CP in variance, C asymmetry, and baryon asymmetry of the universe". In: *Soviet Physics Uspekhi* 34.5 (1991), p. 392.

[4]  V. Fanti et al. "A new measurement of direct CP violation in two pion decays of the neutral kaon". In: *Physics Letters B* 465 (1999), pp. 335–348. ISSN: 0370-2693. DOI: `10.1016/S0370-2693(99)01030-8`.

[5]  A. Alavi-Harati et al. "Observation of Direct *CP* Violation in $K_{S,L} \rightarrow \beta\beta$ Decays". In: *Phys. Rev. Lett.* 83 (1 July 1999), pp. 22–27. DOI: `10.1103/PhysRevLett.83.22`.

[6]  B. Aubert et al. "Measurement of $CP$-Violating Asymmetries in $B^0$ Decays to $CP$ Eigenstates". In: *Phys. Rev. Lett.* 86 (12 Mar. 2001), pp. 2515–2522. DOI: `10.1103/PhysRevLett.86.2515`.

[7]  K. Abe et al. "Observation of Large $CP$ Violation in the Neutral $B$ Meson System". In: *Phys. Rev. Lett.* 87 (9 Aug. 2001), p. 091802. DOI: `10.1103/PhysRevLett.87.091802`.

[8]  R. Aaij et al. "Observation of $D^0 - \overline{D}^0$ Oscillations". In: *Phys. Rev. Lett.* 110 (10 Mar. 2013), p. 101802. DOI: `10.1103/PhysRevLett.110.101802`.

[9]  J. D. Jackson. "Classical Electrodynamics". In: John Wiley & Sons, Inc., 1999. Chap. 4.1, pp. 145–146.

[10] Y. Nagashima. "Elementary Particle Physics: Quantum Field Theory and Particles, Volume 1". In: *Elementary Particle Physics*. Wiley-VCH Verlag GmbH & Co. KGaA, 2010. Chap. Symmetries, pp. 221–266. ISBN: 9783527630097. DOI: `10.1002/9783527630097.ch9`.

[11] S. K. Lamoreaux and R. Golub. *Lepton Dipole Moments*. Ed. by B. L. Roberts and W. J. Marciano. Vol. 20. Advanced Series on Directions in High Energy Physics. 2009. Chap. The Neutron Electric Dipole Moment: Yesterday, Today and Tomorrow, pp. 583–634. DOI: `10.1142/9789814271844_0015`.

[12] J. H. Smith, E. M. Purcell, and N. F. Ramsey. "Experimental Limit to the Electric Dipole Moment of the Neutron". In: *Phys. Rev.* 108 (1 Oct. 1957), pp. 120–122. DOI: `10.1103/PhysRev.108.120`.

[13] C. A. Baker et al. "Improved Experimental Limit on the Electric Dipole Moment of the Neutron". In: *Phys. Rev. Lett.* 97 (13 Sept. 2006), p. 131801. DOI: `10.1103/PhysRevLett.97.131801`.

[14] W. B. Dress et al. "Search for an electric dipole moment of the neutron". In: *Phys. Rev. D* 15 (1 Jan. 1977), pp. 9–21. DOI: `10.1103/PhysRevD.15.9`.

[15] F. M. Piegsa. "New concept for a neutron electric dipole moment search using a pulsed beam". In: *Phys. Rev. C* 88 (4 Oct. 2013), p. 045502. DOI: `10.1103/PhysRevC.88.045502`.

[16] J. Byrne. *Neutrons, Nuclei and Matter: An Exploration of the Physics of Slow Neutrons*. Dover Publications, 2011.

[17] F. Atchison et al. "Measurement of the Fermi potential of diamond-like carbon and other materials". In: *Nuclear Instruments and Methods in Physics Research Section B: Beam Interactions with Materials and Atoms* 260.2 (2007), pp. 647–656. ISSN: 0168-583X. DOI: `10.1016/j.nimb.2007.04.253`.

[18] V. Ignatovich. *The Physics of Ultracold Neutrons*. Clarendon Press, Oxford, 1990.

[19] L. W. Alvarez and F. Bloch. "A Quantitative Determination of the Neutron Moment in Absolute Nuclear Magnetons". In: *Phys. Rev.* 57 (2 Jan. 1940), pp. 111–122. DOI: `10.1103/PhysRev.57.111`.

[20] P. G. Harris et al. "New Experimental Limit on the Electric Dipole Moment of the Neutron". In: *Phys. Rev. Lett.* 82 (5 Feb. 1999), pp. 904–907. DOI: `10.1103/PhysRevLett.82.904`.

[21] J. Zenner. "The search for the neutron electric dipole moment". PhD thesis. Johannes Gutenberg-Universität, Mainz, Aug. 2013.

[22] A. Anghel et al. "The PSI ultra-cold neutron source". In: *Nuclear Instruments and Methods in Physics Research Section A: Accelerators, Spectrometers, Detectors and Associated Equipment* 611 (2009). Particle Physics with Slow Neutrons, pp. 272–275. ISSN: 0168-9002. DOI: `10.1016/j.nima.2009.07.077`.

[23] M. Wohlmuther and G. Heidenreich. "The spallation target of the ultra-cold neutron source UCN at PSI". In: *Nuclear Instruments and Methods in Physics Research Section A: Accelerators, Spectrometers, Detectors and Associated Equipment* 564.1 (2006), pp. 51–56. ISSN: 0168-9002. DOI: `10.1016/j.nima.2006.03.040`.

[24] F. Atchison et al. "The simulation of ultracold neutron experiments using {GEANT4}". In: *Nuclear Instruments and Methods in Physics Research Section A: Accelerators, Spectrometers, Detectors and Associated Equipment* 552.3 (2005), pp. 513–521. ISSN: 0168-9002. DOI: `10.1016/j.nima.2005.06.065`.

[25] L. Hayen. "Cesium Magnetometers in the Neutron Electric Dipole Moment Experiment". MA thesis. KU Leuven, 2014.

[26] N. F. Ramsey. "Resonance Transitions Induced by Perturbations at Two or More Different Frequencies". In: *Phys. Rev.* 100 (4 Nov. 1955), pp. 1191–1194. DOI: `10.1103/PhysRev.100.1191`.

[27] J. M. Pendlebury et al. "Geometric-phase-induced false electric dipole moment signals for particles in traps". In: *Phys. Rev. A* 70 (3 Sept. 2004), p. 032102. DOI: `10.1103/PhysRevA.70.032102`.

[28] P. G. Harris and J. M. Pendlebury. "Dipole-field contributions to geometric-phase-induced false electric-dipole-moment signals for particles in traps". In: *Phys. Rev. A* 73 (1 Jan. 2006), p. 014101. DOI: `10.1103/PhysRevA.73.014101`.

[29]  M. V. Berry. "Quantal Phase Factors Accompanying Adiabatic Changes". English. In: *Proceedings of the Royal Society of London. Series A, Mathematical and Physical Sciences* 392.1802 (1984), pp. 45–57. ISSN: 00804630.

[30]  E. D. Commins. "Berry's geometric phase and motional fields". In: *American Journal of Physics* 59.12 (1991), pp. 1077–1080. DOI: 10.1119/1.16616.

[31]  S. K. Lamoreaux and R. Golub. "Detailed discussion of a linear electric field frequency shift induced in confined gases by a magnetic field gradient: Implications for neutron electric-dipole-moment experiments". In: *Phys. Rev. A* 71 (3 Mar. 2005), p. 032104. DOI: 10.1103/PhysRevA.71.032104.

[32]  G. Pignol and S. Roccia. "Electric-dipole-moment searches: Reexamination of frequency shifts for particles in traps". In: *Phys. Rev. A* 85 (4 Apr. 2012), p. 042105. DOI: 10.1103/PhysRevA.85.042105.

[33]  A. Steyerl et al. "Calculation of geometric phases in electric dipole searches with trapped spin-1/2 particles based on direct solution of the Schrödinger equation". In: *Phys. Rev. A* 89 (5 May 2014), p. 052129. DOI: 10.1103/PhysRevA.89.052129.

[34]  S. Afach et al. "A measurement of the neutron to 199Hg magnetic moment ratio". In: *Physics Letters B* 739 (2014), pp. 128–132. ISSN: 0370-2693. DOI: 10.1016/j.physletb.2014.10.046.

[35]  K. Green et al. "Performance of an atomic mercury magnetometer in the neutron EDM experiment". In: *Nuclear Instruments and Methods in Physics Research Section A: Accelerators, Spectrometers, Detectors and Associated Equipment* 404 (1998), pp. 381–393. ISSN: 0168-9002. DOI: 10.1016/S0168-9002(97)01121-2.

[36]  M. Reta-Hernandez and G. G. Karady. "Attenuation of low frequency magnetic fields using active shielding". In: *Electric Power Systems Research* 45.1 (1998), pp. 57–63. ISSN: 0378-7796. DOI: 10.1016/S0378-7796(97)01232-7.

[37]  A. Keshtkar, A. Maghoul, and A. Kalantarnia. "Magnetic Shield Effectiveness in Low Frequency". In: *International Journal of Computer and Electrical Engineering* 3.4 (2011), pp. 507–513.

[38] S.-K. Lee and M. V. Romalis. "Calculation of magnetic field noise from high-permeability magnetic shields and conducting objects with simple geometry". In: *Journal of Applied Physics* 103.8, 084904 (2008). DOI: `10.1063/1.2885711`.

[39] nEDM Collaboration. *Progress Report 2009 of PSI Proposal R-05-03.1*. Tech. rep. PSI, 2010.

[40] M. Kuzniak. "The Neutron Electric Dipole Moment Experiment: Research and Development for the New Spectrometer". PhD thesis. Jagiellonian University, 2009.

[41] P. Ripka. "Review of fluxgate sensors". In: *Sensors and Actuators A: Physical* 33.3 (1992), pp. 129–141. ISSN: 0924-4247. DOI: `10.1016/0924-4247(92)80159-Z`.

[42] F. Primdahl. "The fluxgate magnetometer". In: *Journal of Physics E: Scientific Instruments* 12.4 (1979), p. 241.

[43] D. Robbes. "Highly sensitive magnetometers - a review". In: *Sensors and Actuators A: Physical* 129 (2006). {EMSA} 2004 Selected Papers from the 5th European Magnetic Sensors; Actuators Conference - {EMSA} 2004, Cardiff, UK, 4-6 July 2004., pp. 86–93. ISSN: 0924-4247. DOI: `10.1016/j.sna.2005.11.023`.

[44] C. Baker et al. "The search for the neutron electric dipole moment at the Paul Scherrer Institute". In: *Physics Procedia* 17 (2011). 2nd International Workshop on the Physics of fundamental Symmetries and Interactions - PSI2010, pp. 159–167. ISSN: 1875-3892. DOI: `10.1016/j.phpro.2011.06.032`.

[45] G. Bison et al. "A new optical magnetometer for MCG measurements in a low-cost shielding room". In: *International Congress Series* 1300 (2007). New Frontiers in Biomagnetism. Proceedings of the 15th International Conference on Biomagnetism, Vancouver, BC, Canada, August 21-25, 2006, pp. 561–564. ISSN: 0531-5131. DOI: `10.1016/j.ics.2007.02.039`.

[46] H. Ohta et al. "Neuromagnetic SQUID measurement in a superconducting magnetic shield". In: *Applied Superconductivity, IEEE Transactions on* 9.2 (1999), pp. 4073–4076. ISSN: 1051-8223. DOI: `10.1109/77.783921`.

[47]   J. Bork et al. "The 8-layered magnetically shielded room of the PTB: Design and construction". In: *Biomag2000, Proc. 12th Int. Conf. on Biomagnetism*. Ed. by J. Nenonen, R. Ilmoniemi, and T. Katila. Helsinki Univ. of Technology, Espoo, Finland, 2001.

[48]   J. D. Jackson. *Classical Electrodynamics*. Third Edition. John Wiley & Sons, Inc., 1999, 95–111and 196.

[49]   R. Merritt, C. Purcell, and G. Stroink. "Uniform magnetic field produced by three, four, and five square coils". In: *Review of Scientific Instruments* 54.7 (1983), pp. 879–882. DOI: 10.1063/1.1137480.

[50]   M. Galassi et al. *GNU Scientific Library Reference Manual (3rd Ed.)* 2012. ISBN: 0954612078.

[51]   N. Wilt. *The CUDA Handbook: A Comprehensive Guide to GPU Programming*. Pearson Education, 2013. ISBN: 9780133261509.

[52]   G. Golub and W. Kahan. "Calculating the Singular Values and Pseudo-Inverse of a Matrix". In: *Journal of the Society for Industrial and Applied Mathematics, Series B: Numerical Analysis* 2.2 (1965), pp. 205–224. DOI: 10.1137/0702016.

[53]   A. N. Tikhonov. "Resolution of ill-posed problems and the regularization method". In: *Dokl. Akad. Nauk SSSR* 151 (1963), pp. 501–504.

[54]   D. Calvetti et al. "Tikhonov regularization and the L-curve for large discrete ill-posed problems". In: *Journal of Computational and Applied Mathematics* 123 (2000). Numerical Analysis 2000. Vol. III: Linear Algebra, pp. 423–446. ISSN: 0377-0427. DOI: 10.1016/S0377-0427(00)00414-3.

[55]   S. Afach et al. "Dynamic stabilization of the magnetic field surrounding the neutron electric dipole moment spectrometer at the Paul Scherrer Institute". In: *Journal of Applied Physics* 116.8, 084510 (2014). DOI: 10.1063/1.4894158.

[56]   J. L. Kirschvink. "Uniform magnetic fields and double-wrapped coil systems: Improved techniques for the design of bioelectromagnetic experiments". In: *Bioelectromagnetics* 13.5 (1992), pp. 401–411. ISSN: 1521-186X. DOI: 10.1002/bem.2250130507.

[57]  *How Do I Eliminate Ghosting from My Measurements?* Tech. rep. National Instruments, 2014.

[58]  *Magnetic Alloy 2705M (cobalt-based).* Tech. rep. Metglas®, Inc., 2014.

[59]  N. Mingard. *Dokumentation Spannung-Strom Verstärker.* Tech. rep. ETH Zurich, 2012.

[60]  R. Barrera, G. Estevez, and J. Giraldo. "Vector spherical harmonics and their application to magnetostatics". In: *European Journal of Physics* 6.4 (1985), p. 287.

[61]  A. Sezginer. "The inverse source problems of magnetostatics and electrostatics". In: *Inverse Problems* 3.4 (1987), p. L87.

[62]  J. D. Jackson. "Classical Electrodynamics". In: John Wiley & Sons, Inc., 1999. Chap. 3.9, pp. 120–121.

[63]  M. Abramowitz and I. A. Stegun. *Handbook of mathematical functions.* National Bureau of Standards, 1972. Chap. Elliptic Integrals.

[64]  J. C. Simpson et al. *Simple Analytic Expressions for the Magnetic Field of a Circular Current Loop.* Tech. rep. `http://ntrs.nasa.gov/archive/nasa/casi.ntrs.nasa.gov/20010038494_2001057024.pdf`: NASA, 2001.

[65]  J. Wang, S. She, and S. Zhang. "An improved Helmholtz coil and analysis of its magnetic field homogeneity". In: 73.5 (2002), pp. 2175–2179. ISSN: 00346748. DOI: `10.1063/1.1471352`.

[66]  G. Peeren. "Stream function approach for determining optimal surface currents". In: *Journal of Computational Physics* 191.1 (2003), pp. 305–321. ISSN: 0021-9991. DOI: `10.1016/S0021-9991(03)00320-6`.

[67]  N. Nouri and B. Plaster. "Comparison of magnetic field uniformities for discretized and finite-sized standard $\cos\theta$, solenoidal, and spherical coils". In: *Nuclear Instruments and Methods in Physics Research Section A: Accelerators, Spectrometers, Detectors and Associated Equipment* 723 (2013), pp. 30–35. ISSN: 0168-9002. DOI: `10.1016/j.nima.2013.05.013`.

[68]  J. E. Everett and J. E. Osemeikhian. "Spherical coils for uniform magnetic fields". In: *Journal of Scientific Instruments* 43.7 (1966), p. 470.

[69] W. E. Lorensen and H. E. Cline. "Marching Cubes: A High Resolution 3D Surface Construction Algorithm". In: *SIGGRAPH Comput. Graph.* 21.4 (Aug. 1987), pp. 163–169. ISSN: 0097-8930. DOI: `10.1145/37402.37422`.

[70] E. A. Donley et al. "Demonstration of high-performance compact magnetic shields for chip-scale atomic devices". In: *Review of Scientific Instruments* 78.8 (2007), p. 083102. DOI: `10.1063/1.2767533`.

[71] Stefan Mayer Instruments. *Magnetic Field Sensor FLC3-70 Data sheet*. Accessed 12.03.2015. `http://www.stefan-mayer.com/images/datasheets/Data-sheet_FLC3-70.pdf`.

[72] B. Efron. "Bootstrap Methods: Another Look at the Jackknife". In: *Ann. Statist.* 7.1 (Jan. 1979), pp. 1–26. DOI: `10.1214/aos/1176344552`.

[73] B. Efron. "Missing Data, Imputation, and the Bootstrap". English. In: *Journal of the American Statistical Association* 89.426 (1994), pp.463–475. ISSN: 01621459.

[74] G. Quemener. "$B_0 \downarrow$ correcting coils currents optimisation summary (using maps from Summer 2010)". 2010.

[75] G. Quemener. "$B_0 \uparrow$ correcting coils currents optimisation summary (using maps from Summer 2010)". 2010.

[76] H. W. Kroto et al. "C60: Buckminsterfullerene". In: *Nature* 318.6042 (Nov. 1985), pp. 162–163. DOI: `10.1038/318162a0`.

[77] J. L. Horowitz. "Handbook of Econometrics". In: ed. by J. Heckman and E. Leamer. Vol. 5. Elsevier Science B. V., 2001. Chap. 52: The Bootstrap, pp. 3160–3223.

[78] I. Jolliffe. *Principal Component Analysis*. Springer, 2002.

# Acknowledgements

Firstly, I would like to thank my supervisor, professor Kazimierz Bodek, who was a big inspiration for me and has motivated me to do more than I thought I could. The rest of our working group in Krakow, Dagmara Rozpędzik, Adam Kozela, Jacek Zejma, Michał Rawlik and Maciej Perkowski were also giving me a helping hand whenever I was at a dead end.

I would also like to thank my supervisor during my 2-year stay in Switzerland, Klaus Kirch. His knowledge and experience were very helpful during this period. The rest of Low Energy Physics group in the Institute for Particle Physics at ETH Zürich, Aldo Antognini, Florian Piegsa, Kim Siang Khaw, Katherina Kwuida and Jochen Krempel gave me a warm welcome and helped me survive 2 years away from my family and friends. They have also shared their expertise, making it easier for me to achieve my goal. It was a great opportunity to work with nEDM experiment group. Their dedication to details in pursuit for better measurement sensitivity is still an example for me to follow. Discussions with Gilles Quemener were an inspiration for me in the search for the optimal magnetic field compensation system, while talks with Beatrice Franke helped me in works on prototype.

In the end, I would like to thank my wife, Iwona, who was very patient during my whole work on this dissertation. She has listened to all my sorrows and gave me additional strength when I had a bad day. I would also like to express my gratitude to my parents, Alina and Krzysztof, who made it possible for me to study Physics and continue doing my PhD and my sister, Aleksandra, who was always there to cheer me up.